DISSERTATION

MODELING OF FLUOROCARBON FILMS DEPOSITION BY HFCVD

Submitted by

Chutima Jarusiripot

Department of Chemical Engineering

In partial fulfillment of the requirements

For the Degree of Doctor of Philosophy

Colorado State University

Fort Collins, Colorado

Spring 2006

COLORADO STATE UNIVERSITY

February 8, 2006

WE HEREBY RECOMMEND THAT THE **DISSERTATION** PREPARED UNDER OUR SUPERVISION BY CHUTIMA JARUSIRIPOT ENTITLED MODELING OF FLUOROCARBON FILMS DEPOSITIONS BY HFCVD BE ACCEPTED AS FULFILLING IN PART REQUIREMENTS FOR THE DEGREE OF DOCTOR OF PHILOSOPHY.

Committee on Graduate Work

Laurence A. Belfiore

Ellen R. Fisher

Bruce A. Parkinson

Walajabad S. Sampath

Adviser: David S. Dandy

Department Head/Director: David S. Dandy

ABSTRACT OF DISSERTATION

MODELING OF FLUOROCARBON FILM DEPOSITION BY HFCVD

The present studies are directed toward the design of a new, one-dimensional, continuous flow HFCVD reactor using a rigorous computational fluid dynamics (CFD) approach. The uniform concentration boundary layer thickness over the substrate is required to achieve good quality films. First the inlet showerhead is simulated to determine the appropriate velocity profile for the reactor design simulations. The effects of the spacing between holes in the inlet showerhead, space near the walls, and the diameter of the showerhead holes have been investigated. The results from these studies indicate that there is little effect on the entrance length and the shape of the velocity profiles due to the shower hole spacing, shower hole diameter, and spacing near the chamber walls. The velocity profiles derived from Navier Stokes equation for a rectangular chamber showed very good agreement with the simulation profiles. This analytical expression was applied as the inlet velocity boundary condition gas flow. Next, the effects of the filament diameter and the spacing between filaments on the temperature distribution in the gas above the substrate region were investigated. Only the momentum and energy conservation equations were used in the calculations. The results show that the filament diameter and the spacing between each filament are also crucial to the temperature profiles. Increasing the filament spacing and filament diameter increases temperature fluctuations. Next, the effects of gas flow rate, hot gas volume thickness, the space above the filaments, and the space between the substrate and hot gas on the

temperature and mass fraction profiles were investigated using the reactor with the surrogate filament array. By changing the reactor flow rate in the range of 0.001 to 0.1 m^3/s (which is equivalent to the Reynolds number of 2.75 to 275) significantly changed both the temperature and mass fraction profiles. Uniform temperature achieved when the flow rate was at least 0.01 m^3/s. The CF_2 mass fraction gradient near the substrate surface is highest and more uniform in the flow direction when the flow rate is approximately 0.01 m^3/s. Increasing the hot gas region thickness does not change the temperature profile below the filaments, but increases the extent of the reaction in the reactor, resulting in a higher CF_2 gradient near the substrate. When the space above the filament array was reduced from 1.65 cm to 0.5 cm, the temperature profiles below the filament arrays was not changed, however the CF_2 mass fraction gradient near the substrate was increased. Decreasing the space below the filament from 6.5 to 5 mm does not significantly change either the temperature or CF_2 mass fraction profiles near the substrate. The optimal range is somewhere between 5 to 7 mm.

Chutima Jarusiripot
Chemical Engineering Department
Colorado State University
Fort Collins, CO 80523
Spring 2006

ACKNOWLEDGMENT

This dissertation could not be finished without helps and supports from many people.

First of all, I would like to thank Dr. David S. Dandy, for serving as my advisor, and providing guidance and supports over these years. I also thank to Dr. Laurence A. Belfiore, Dr. Ellen R. Fisher, Dr. Bruce A. Parkinson, and Dr. Walajabad S. Sampath for serving on my committee.

Thank to Dr. Robert N. Meroney in civil engineering for his brief introduction on how to use Fluent and Gambit program, and his permission for using these program in the Engineering Studio Lab.

I also would like to thank Thai government for giving me the financial support during the first three years of my study here.

Finally, I would like to thank my family for being so supportive in every step of the way with love and enthusiasm. Special thank to my father, without his love and encouragement, I would never come to this point.

TABLE OF CONTENTS

LIST OF TABLES

LIST OF FIGURES

Chapter 1

INTRODUCTION

Fluorocarbon films have been used in a wide range of commercial applications because of their unique chemical, mechanical, and electrical properties. These applications include their use as dielectric layers, biopassive coatings, antifouling linings, permeable membranes, and chemically resistant barriers. Of particular importance is the low dielectric constant (low-k) behavior of these materials, and their potential role in multilayer devices. As the size of electronic devices gets smaller, the increased RC delay (the product of the resistance and capacitance of a circuit), power dissipation, and crosstalk (a measure of the coupling of a signal from one portion of a circuit to another) become serious problems due to the increasingly tight spacing of interconnects. Both RC delay and crosstalk can be effectively reduced by lowering the dielectric constant of the insulator, and this drives the need to identify a new, low dielectric material to replace the existing oxide material.

Fluorocarbons have been examined as one of the possible materials for this low-k application because of its very low dielectric constant (k ~ 2 to 2.7) [1, 2], compared to other low-k materials such as fluorinated SiO_2 (k ~ 3.3 to 3.7) [3], spin-on glass films (k ~ 2.5 to 4.0) [4], and spin-on organic films (k ~ 2.6 to 3.4) [5 – 7]. The International Technology Roadmap for semiconductors (2001 and 2002 update) [8] identifies fluorinated organic polymer films as ultra low-k (k <2.5) and extreme low-k (k ≤1.9) dielectric material candidates. However, many challenges exist that have prevented the integration of fluorocarbon films into microelectronic fabrication

processes. A key issue is that, to date, fluorocarbon films synthesized via chemical vapor deposition (CVD) are not sufficiently stable at elevated temperatures, including temperatures consistent with normal device operation. Significant effort has been made to produce polymer films with highly cross-linked structure to increase thermal stability, but these have been largely empirical investigations using plasma enhanced chemical vapor deposition (PECVD) techniques [2, 9-17]. Films deposited from PECVD usually require treatment at high temperature to eliminate excess free radicals, i.e., dangling bonds, and some weak bonds that are created in the polymer network during deposition. Without intervention, these dangling bonds usually react with oxygen or water in the atmosphere, causing undesirable variations in film properties overtime.

In recent studies, pulsed plasma enhanced chemical vapor deposition (pulsed PECVD) has been used to deposit fluorocarbon films [1, 18-21]. Pulsed PECVD is a combination of PECVD and thermal CVD, where the plasma excitation is applied over a short period (on-time ~ 10 ms) followed by an off-time or no excitation period (50 to 400 ms). Various film structures, which range from cross-linked networks to linear polymer chains of polytetrafluoroethylene (PTFE), can be achieved by changing the duration of the off-time period [22]. Films deposited using short off-time periods had significant amounts of CF_3, CF_2, CF and quaternary carbon in their composition, while films deposited using longer off-time periods mainly consisted of CF_2 linear chains. The dangling bond concentration also decreases with increasing off-time period, since ion bombardment at the film surface is diminished at short applied plasma periods [18].

The dependence of film chemistry and properties on off-time in pulsed PECVD system led investigators to explore thermal CVD techniques such as hot filament chemical vapor deposition (HFCVD). The films deposited via HFCVD have F:C ratios near 2, and 90% of CF_2 fraction together with 10% of CF_3 and CF moieties. An increase in crystalinity of films was also found in HFCVD films [23]. The refractive index of the films was around 1.33 to 1.38, which is very close to that of bulk PTFE (1.38). The dangling bond concentration also appeared low compared to those films deposited from continuous PECVD. These films have much closer properties to those of bulk PTFE [23], and may be applicable as interlayer dielectric (ILD) materials since bulk PTFE has a low dielectric constant ($k \sim 2$), a very low dielectric loss, a degradation temperature above 673 K, and is an excellent moisture barrier [22]. However, films with more linear CF_2 chain character showed loss of molecular weight or chain unzipping during thermal annealing at 200 °C in ambient nitrogen [24].

An important distinction between HFCVD and more traditional CVD techniques is independent control over gas phase temperature and substrate temperature. For fluorocarbon film deposition, the substrate temperature is maintained at 21 °C while the gas temperature is as high as 500 °C. The ability to independently control gas phase and substrate temperature makes HFCVD a powerful tool for separately investigating the gas phase and surface reaction mechanisms. Experiments carried out by Lau et al. [25] showed that differences in grain structure were observed when the filaments, made of resistive heating wire (80% Ni/20% Cr), were preheated before the deposition of film from a hexafluoropropylene oxide (HFPO) precursor. This observation suggests that the filaments play an active role in the decomposition of

HFPO, since chromium and its oxidized states are known to act as catalysts for epoxide ring opening. Although the experiments have revealed some insights into the chemistry associated with fluorocarbon film deposition, there are still a number of important, unanswered questions about the chemistry occurring in these systems. For example, while substantial polymerization of fluorocarbene occurs in these systems, it is still unclear whether this happens in the gas phase or at the substrate surface, or to what degree it may be a combination of the two. It is possible that one of these two polymerization processes controls the overall film growth rate, and perhaps more important, controls the properties of the resulting film.

Like most other CVD systems, the reactor geometry in HFCVD strongly affects flow, energy, and mass transport behavior during the deposition processes, which in turn affects the properties of the deposited films. This dissertation focuses on the development of a rational approach for the design of a HFCVD system to be used for the deposition of ultra and extreme low-*k* fluorocarbon films. Computational fluid dynamics (CFD) will be used to investigate different reactor geometries and operating conditions. The achievement of a uniform concentration boundary layer thickness over a constant temperature deposition surface, which is required to achieve films with uniform thickness and properties, will be used as the criterion for determining the optimum reactor configuration.

1.1 The Deposition Process of Fluorocarbon Films

Many different techniques have been applied to produce fluorocarbon films, and these can be categorized into two groups: physical vapor deposition and chemical vapor deposition. Physical vapor deposition methods include simple vacuum evaporation [26] and rf sputtering [27]. The vacuum evaporation technique can be

only used in special cases where polymers with a low molecular weight evaporate as monomers and condense on the substrate without reactions occurring. Polymer films formed by vacuum evaporation have lower dissociation temperature than the source materials [26]. In rf sputtering, the volatile polymer fragments are emitted into the plasma volume and serve as precursors in the plasma polymerization process. The rf deposited films are highly cross-linked and have amorphous structure that are similar to films deposited from the fluorocarbon gaseous feeds [27-28] when sputtered under fluorocarbon mixtures. Chemical vapor deposition usually requires at least two step chemical reaction mechanisms: the dissociation of the feed gas to form reactive species, and the subsequent gas-phase or surface reactions of these active species to form films on the substrate. Two main variations of the dissociation methods have been applied: plasma and thermal pyrolysis. Plasma enhanced CVD, pulsed plasma CVD, and high density plasma CVD use plasma to create reactive species, such as radicals and ions from the feed monomers, while hot filament CVD uses energy generated from the hot wire to create reactive species from the feed monomers. Chemical vapor deposition (CVD) appears to be an attractive method because of its ability of completely fill high aspect ratio features, and their compatibility with the existing integrating process. Most of the fluorocarbon films to date have been deposited by the CVD techniques. Various CVD deposition techniques will be discussed here.

1.1.1 Plasma-Enhanced Chemical Vapor Deposition (PECVD)

The observation that glow discharges in various organic vapors resulted in the formation of polymer films on surface exposed to the discharge was made more than 50 years ago [29]. The acceleration of electrons and ions in an electric field

causes collisional excitation of the organic molecule to an elevated electronic level as well as direct ionization, and the recombination of these ions, radicals, and excited molecules are responsible for the film formation on the surface. This technique was first applied to produce useful insulating films by Goodman in 1960 [29]. He used a pair of parallel electrodes immersed in organic vapor, and by applying a sufficiently large potential difference across the electrodes he obtained a glow discharge that resulted in polymer film deposition on the electrodes. By placing a substrate on one of the electrodes, Goodman was able to coat it with polymer film to the desired thickness. This original dc glow technique requires relatively high gas pressures, and a considerable amount of substrate heating. The deposited films were cross-linked high molecular weight polymers. Up to 8 μm/min deposition rates were reported in this type of reactor. To improve the efficiency of the discharge and reduce the substrate heating, Connell and Gregor used an rf electrodeless coil to create a glow discharge inside a tube through which monomer gas was flowed [30]. This rf discharge needed less power input to sustain the glow than Goodman's.

More recently, plasma-enhanced chemical vapor deposition (PECVD) has been widely used to deposit films from a variety of fluorocarbon precursors [2, 9, 11-12, 30-31]. Most PECVD of fluorocarbon thin films use a continuous radio frequency (rf) of 13.56 MHz within the glow region to create fluorocarbon plasmas. These plasmas have been used extensively in the microelectronics industry to anisotropically etch silicon and silicon dioxide [9]. Film formation results from a competition between substrate etching and film deposition reactions in fluorocarbon plasmas. By modifying the plasma conditions, plasma equilibrium can be shifted to deposition rather than etching, and these films can be preferentially deposited [10]. A simple rf

parallel plate reactor is shown schematically in Figure 1.1 [11]. Capacitively coupled glow discharges typically operate in the range of 100 mtorr to 20 torr, with plasma densities between 10^9 and 10^{11} cm^{-3}, and T_e between 3 and 10 eV [31]. Different film conformations can be obtained by changing deposition conditions such as plasma power, applied substrate bias, and the precursor sources. Increasing the rf absorbed power usually increases the cross-linking density and the dielectric constant [11-12]. Typical precursors used in PECVD include CF_4, C_2F_4, C_2F_6, C_3F_6, CHF_3, C_4F_8, C_6H_5F, HFPO, SF_6, NF_3, mixtures of these fluorocarbon compounds, and mixtures of these fluorocarbon compounds with any of the following compounds, including H_2, N_2, He, Ar, CH_4, C_2H_2, and C_6H_6 [11-16, 20].

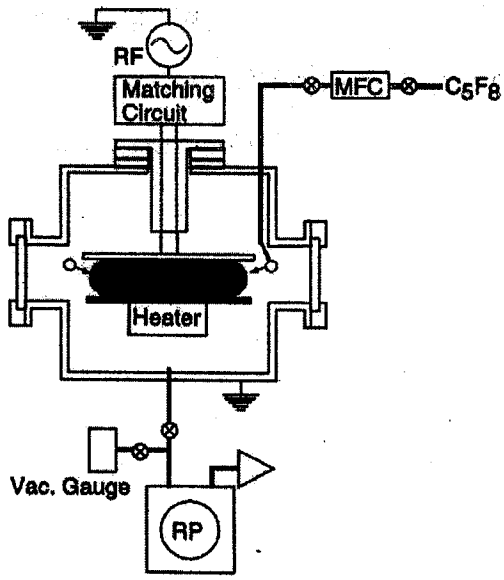

Figure 1.1 Schematic diagram of rf parallel plate PECVD reactor.

Films deposited by PECVD have highly cross-linked amorphous structure and high dangling bond concentrations, i.e., unpaired electron, and trapped free radicals, that are theorized to give rise to dielectric loss and aging effects [31]. These dangling bonds are the results of the imbalances in the production and consumption rates of free radicals during the plasma polymerization process [17]. Typical dangling bond concentrations for PECVD polymers are 10^{18} to 10^{20} spins/cm^3 [32], which can sometimes be reduced by low temperature annealing [33]. Films deposited at lower pressure are highly amorphous due to the increase in surface bombardment from energetic particle [34]. The F:C ratios of continuous PECVD films are low compared to those of films from pulsed and pyrolytic CVD. Typical PECVD films deposited from HFPO have a F:C ratio of only ~ 1.6 and CF_2 fraction of 32% [20]. In addition to CF_2 groups, comparable concentrations of CF_3, CF and quaternary carbon moieties are also found in continuous PECVD. In addition, unlike bulk PTFE, continuous PECVD films may contain carbon-carbon double bonds.

1.1.2 Pulsed Plasma-Enhanced Chemical Vapor Deposition (pulsed PECVD)

The purpose of the power pulsing is to enable plasma processes to approximate a thermal process but at lower process temperatures. This approach has been used to produce films that have an order of magnitude lower dangling bond density than films formed from continuous plasma deposition processes. This impact is to produce low-*k* films that are less lossy. The major drawback of power pulsing is that it could create plasma-induced damage in CMOS transistors. This is a problem that would not be easily minimized by process modification, as it would be difficult to remove spatial and temporal voltage gradients from the plasma within processing equipment [31].

In a pulsed PECVD process, rf power is applied for a specific "on" time, followed by an "off" time period during which no excitation is used. During the "on" time, both ions and reactive neutrals are produced. However, ions often have shorter lifetimes than neutrals. During the "off" time the ratio of neutrals to ions will increase, and thus, the process equilibrium will be shifted to favor film deposition from reactive neutrals. The pulsed PECVD process is believed to follow a deposition mechanism similar to that for remote or afterglow PECVD, where the substrates are placed outside the glow region. Both pulsed and downstream PECVD allow long-lived neutral intermediates to participate in the deposition process. The deposition rates of downstream PECVD are typically low (~ 1.6 Å/min) compared with pulsed PECVD (17 to 52 Å/min) [34-35]. Films deposited from downstream HFPO plasmas contain oriented CF_2 chains terminated with CF_3 groups, and these chains are perpendicular to the substrate [36].

Pulsed plasma has been reported to dramatically change the nature of the deposited fluorocarbon film [21, 37-38]. Films deposited by pulsed excitation have lower dangling bond concentrations than those of continuous PECVD films [18]. The composition of films deposited from hexafluoropropylene oxide (HFPO) depends strongly on the pulse "off" time. At very short pulse off times (10 ms on, 20 to 60 ms off time) films contain significant fractions of CF_3, CF_2, CF, and quaternary carbon C–CF. As the pulse off time is increased, the film composition is dominated by CF_2 fraction (~ 64%) [39]. A few atomic percent of oxygen have been detected in pulsed plasma films [20-21,37-38]. The gas phase concentration of CF_2 relative to other film-forming species is believed to be the controlling factor for film composition [21]. Although slight changes in film compositions are observed when the substrate

temperature changes, the deposition rate increases significantly as substrate temperature decreases. As substrate temperature is decreased from 126 to -26 °C, the deposition rate increases from 0.4 to 2.6 Å /cycle [21].

The choice of precursors is also important in pulsed PECVD systems. Addition of hydrogen to a pure fluorocarbon system will shift the boundary between etching and deposition regimes [19]. Films deposited from different precursors show different distributions of CF_x species. Films from $C_2H_2F_4$ and CH_2F_2 have higher content of quaternary carbon or C–CF species, whereas films from $CHClF_2$ and HFPO are dominated by CF_2 species [19]. All these precursors have similar F:C ratios, but their F:H ratios can vary significantly. The CF_x species distributions in the films are largely controlled by the competition between CF_2-producing and HF elimination reactions in the pulsed plasmas. Dominance by HF elimination produces films with higher C–CF and CF concentrations, whereas dominance by CF_2-producing reactions leads to films with higher CF_2 concentrations. Pulsed plasma films from all three precursors gave dielectric constants of 2.4, with loss tangents or the dissipation factor (tan δ) on the order of 10^{-2}. Dielectric measurements of pulsed plasma films from hexafluoropropylene oxide gave a dielectric constant of 2.0 ± 0.1 with a loss tangent of 0.009 [19]. Films from HFPO and $CHClF_2$ had F:C ratios of 1.9 and 1.22, respectively, whereas films from CH_2F_2 and $C_2H_2F_4$ had F:C ratios of 0.6 and 0.91, respectively [19].

1.1.3 Hot Filament Chemical Vapor Deposition (HFCVD) for PTFE

A schematic diagram of a hot filament chemical vapor deposition reactor is shown in Figure 1.2 [24]. Undiluted hexafluoropropylene oxide was used as feed gas to produce fluorocarbene monomer. Conditions used in the deposition process are summarized in Table 1.1 [25]. Preconditioning time in Table 1.1 refers to the duration

of filament heating at the desired process conditions prior to actual film deposition. Films were grown on 100-mm diameter p-type silicon wafers. The gas in the reactor was heated by resistive heating filaments made of 28 AWG Nichrome wire (80% Ni / 20% Cr). The filament was placed 15 mm above the substrate. The substrate temperature was maintained at the desired temperature by backside water cooling.

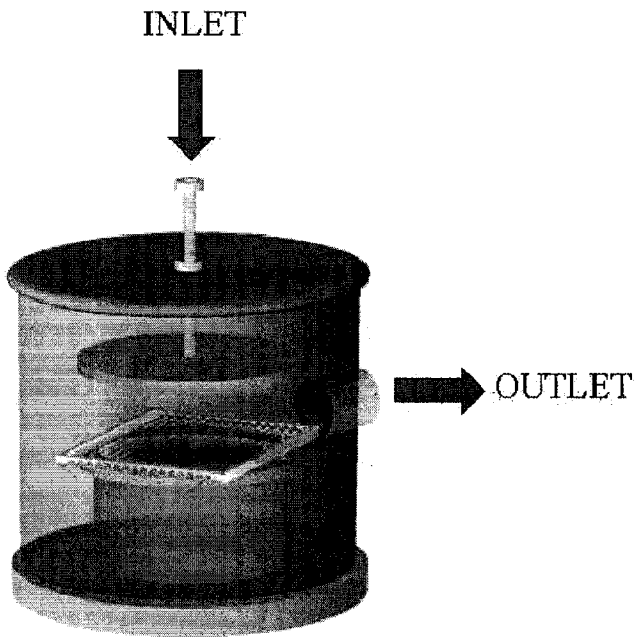

Figure 1.2 Schematic diagram of HFCVD reactor.

Table 1.1 Deposition conditions for HFPO HFCVD film [23, 25]

Parameters	*Value from Ref. [25]*	*Value from Ref [23]*
Flow rate (sccm)	15, 30	12.5
Preconditioning time (min)	0, 15	0
Substrate Temperature (°C)	21 ± 5	20 ± 3
Filament Temperature (°C)	500 ± 50	325 – 535
Pressure (Torr)	1	1

Films deposited by HFCVD have a high content of CF_2 (~ 90% for films deposited at 1 torr, 673 K filament temperature), and low dangling bond concentration [23]. The deposition rates of HFCVD increase with filament temperature, but decrease with increasing flow rate (from 15 sccm to 30 sccm) [25]. The reported deposition rate is about 35 μm/h for deposition at a filament temperature of 808 K, and 1.8 μm/h at 691 K filament temperature. Both rates were measured at 1 torr pressure, and 12.5 sccm HFPO flow rate [23].

The morphology of deposited films without preconditioning and with 15 min preconditioning before actual films deposition are different. Films deposited with no filament preconditioning display spherical nodules, while films deposited with filament preconditioning have anisotropic rod-like grains. The highest degree in grain anisotropy was observed in films deposited with a 30 sccm HFPO flow rate and 15 min filament preconditioning. The content of OH and CO/COO groups in the film was also found to be minimum at this same set of conditions. These OH and CO/COO moieties are possibly formed from the reaction of unterminated radicals at the chain ends with oxygen and water in the atmosphere after the reactor is opened. If this supposition is correct, films with a higher OH/CF_2 ratio would contain a greater number of shorter CF_2 chain structures, while films with lower OH/CF_2 would contain

a fewer number, but longer, CF_2 chain structures. The possible reaction pathways for the oxygen and hydrogen incorporation are expressed as follows [25]:

$$-CF_2CF_2CF_2\cdot + O_2 \rightarrow -CF_2CF_2CF_2OO\cdot$$

$$-CF_2CF_2CF_2OO\cdot \rightarrow -CF_2CF_2CF_2O\cdot + O$$

$$-CF_2CF_2CF_2O\cdot \rightarrow -CF_2CF_2COF\cdot + F$$

$$-CF_2CF_2COF\cdot + H_2O \rightarrow -CF_2CF_2COOH\cdot + HF$$

1.2 Overview of Research

The objective of this work is to design a new, one-dimensional flow HFCVD reactor using the computational fluid dynamics (CFD) approach. The reactor geometry strongly affects the flow characteristics, which in turn affects the properties of films. A uniform concentration boundary layer thickness over the substrate is required to achieve good quality films. The studies in this research are directed toward the design of the one-dimensional flow HFCVD reactor. The mathematical models including fluid flow, energy transport, mass transfer equation, and the boundary conditions that are normally used in CVD modeling are presented in section 2.1. Then, the physical properties of all the species involved in the reactions and the methods used to calculate those properties that are not available in the literature are presented in 2.2. Sections 2.3 and 2.4 are devoted to the gas phase reactions and an example of the simulation of original radial flow HFCVD reactor using the Fluent Program version 6.1 (Fluent Inc., USA).

Chapter 3 will present the effects of the showerhead inlet configuration, including the hole diameter, hole spacing, and the gap near the wall. The analytical

expression of the inlet velocity profiles derived from the Navier-Stokes equations and the comparison of the analytical profiles with the profiles from the scaled-up showerhead inlet will be presented in the following sections in this chapter.

Chapter 4 will present the design of the filament arrays considering the effects of the filament diameter, and filament spacing. Then, the preferred filament array configuration will be used to simulate the fluid flow, energy transfer, and mass species equations. The simulation results from this reactor will be compared with the results from the reactors that the filament array is replaced by the hot gas region at the location of the filament arrays in the reactor.

Chapter 5 will look into the effects of the gas flow rates first, then the reactor sizing which includes the thickness of the hot gas region, the overhead space above the filaments array, and the space between the substrate and the filaments. Finally, the conclusion and the recommendations for future work will be presented in Chapter 6.

Chapter 2

ANALYSIS OF A CYLINDRICAL HOT FILAMENT CVD REACTOR

In most thermal CVD system, film qualities are highly determined by transport phenomena in the gas mixture and by chemical reaction in the gas mixtures near the substrate surface. On the other hand, the transport process and chemical kinetic reaction strongly depend on the operating condition, i.e., species concentration and flow rate, etc., and on the reactor geometry. To achieve high quality films, a well designed reactor is needed. The objective of this study is to design a one-dimensional horizontal flow HFCVD system to be used for the deposition of ultra and extreme low-k fluorocarbon films. The realization of a uniform concentration boundary layer thickness over a constant temperature deposition surface, which is required to achieve films with uniform thickness and properties, will be used as the criterion for determining the optimum reactor configuration.

2.1 Mathematical Modeling

The mathematical equations generally used in modeling CVD reactor consist of fluid flow (momentum), energy, and species transport equations and chemical reactions in both gas phase and on the surface of substrate. These equations incorporate the thermodynamics and physical properties of the gas species in the reactor, as functions of composition, temperature and pressure. Unfortunately, some of these properties required for modeling of the tetrafluoroethylene films deposition

are not available in the literatures. The essential species and prediction method are explained in this section.

2.1.1 Assumption in Model Development

The following assumptions have been used in CVD reactor modeling.

1. The gas mixture in the reactor can be treated as a continuum. This assumption is valid when the mean free path of the gas molecules in the reactor is much smaller than the characteristic length of the reactor geometry, this relationship may be specified from the Knudsen number. Generally the continuum approach is valid when the Knudsen number K_n is << 1, which practically speaking, means for $K_n < 0.01$. The Knudsen number is defined as $K_n = \ell / \mathcal{L}$, where ℓ is mean free path of gas molecules in the reactor, and $\mathcal{L}$ is an appropriate characteristic length in the reactor. The mean free path for the species in this system at 600 K is in the range of 4.989×10^{-5} m to 8.866×10^{-5} m, which corresponds to K_n of 0.003 to 0.005.

2. For the range of pressures and temperatures used in CVD, the gases in reactor may be treated as ideal gases.

3. For low pressure CVD reactors, the gas flow can be assumed to be laminar. The Reynolds number for typical CVD is in the range of 10^{-2} to 10^{2}, depending on the flow rate, pressure, temperature, and reactor dimensions. The Reynolds number is

defined as the ratio of the product of characteristic length and velocity to kinematic viscosity. In general, the flow is laminar when the Reynolds number is less than 2000.

4. The gases in the reactor do not absorb radiative energy from the susceptor.

5. Viscous dissipation and pressure work contribute negligibly to energy changes in the gas phase.

6. The effects of pressure variations on the temperature of the gas mixture may be neglected for the low Mach number flow in CVD reactor. The Mach number is defined as the ratio of the gas velocity to sound velocity in the same gas medium.

2.1.2 Fluid Flow and Energy Transport

The gas flow in CVD reactors can be described by the mass conservation, or continuity equation

$$\frac{\partial \rho}{\partial t} = -\nabla \cdot \rho \boldsymbol{v}, \tag{2.1}$$

where ρ is the mixture density and $\boldsymbol{v}$ is the velocity. The conservation equations for momentum, which reduce to the Navier-Stokes equations for Newtonian fluids, are

$$\frac{\partial \rho \boldsymbol{v}}{\partial t} = -\nabla \cdot (\rho \boldsymbol{v}\boldsymbol{v}) - \nabla \cdot \boldsymbol{\tau} - \nabla P + \rho \boldsymbol{g}, \tag{2.2}$$

where P is pressure, and the $\boldsymbol{\tau}$ is the viscous stress tensor,

$$\boldsymbol{\tau} = -\mu(\nabla \boldsymbol{v} + (\nabla \boldsymbol{v})^T) - (\kappa - \frac{2}{3}\mu)(\nabla \cdot \boldsymbol{v})\boldsymbol{I}\,, \tag{2.3}$$

where μ is the dynamic viscosity, κ is the bulk viscosity, and the superscript ^{T} indicates the transposed tensor.

For steady state conditions, the continuity, and Navier-Stokes equations reduce to

$$\nabla \cdot \rho \boldsymbol{v} = 0 \tag{2.4}$$

and

$$\nabla \cdot (\rho \boldsymbol{v}\boldsymbol{v}) + \nabla \cdot \boldsymbol{\tau} + \nabla P - \rho \boldsymbol{g} = 0\,. \tag{2.5}$$

Since all the physical properties (ρ, μ) are functions of temperature, the momentum equation is coupled to the energy equation. The expression for the energy transport is given by

$$\begin{aligned} \rho c_p \frac{\partial T}{\partial t} = -\rho c_p (\boldsymbol{v} \cdot \nabla T) + \nabla \cdot (\lambda \nabla T) + \sum_{i=1}^{N} \frac{\overline{H}_i}{M_i} (\nabla \cdot \boldsymbol{j}_i) \\ - \sum_{i=1}^{N} \sum_{k=1}^{K} \overline{H}_i \nu_{ik} (\mathcal{R}_k^g - \mathcal{R}_{-k}^g), \end{aligned} \tag{2.6}$$

where c_p is the specific heat capacity of the gas, T is temperature, λ is the thermal conductivity, and R is the universal gas constant. The quantities M_i in the above equation represent species molar mass. $\mathcal{D}_i^T$ is the thermal diffusion coefficient, $\overline{H}_i$ is

the partial molar enthalpy, and $\boldsymbol{j}_i$ is the diffusive mass flux of species i. ν_{ik} is the stoichiometric coefficient of the i^{th} species in the k^{th} gas phase reaction, and $\mathcal{R}_k^g$ and $\mathcal{R}_{-k}^g$ are the forward and reverse reaction rates. The third term on the right hand side of Eq. (2.6) represents the energy transfer caused by the interdiffusion of the chemical species. The energy equation for the steady state condition becomes

$$\rho c_p(\boldsymbol{v}\cdot\nabla T)=\nabla\cdot(\lambda\nabla T)+\sum_{i=1}^{N}\frac{\overline{H}_i}{M_i}(\nabla\cdot\boldsymbol{j}_i)-\sum_{i=1}^{N}\sum_{k=1}^{K}\overline{H}_i\nu_{ik}(\mathcal{R}_k^g-\mathcal{R}_{-k}^g), \qquad (2.7)$$

The fluid properties such as λ, μ, ρ, and c_p are functions not only of temperature and pressure, but also of the gas composition in the reactor. Thus the momentum and energy equations are also coupled with the species transport equation.

2.1.3 Mass Transfer Equation

The diffusion of gas in a CVD reactor usually results from the concentration gradients (ordinary diffusion) and temperature gradients (Soret effect). The mass balance for the i^{th} species in k^{th} gas phase reaction can be written as

$$\rho\frac{\partial w_i}{\partial t}=-\rho\mathbf{v}\cdot\nabla w_i-\nabla\cdot\mathbf{j}_i+M_i\sum_{k=1}^{K}\nu_{ik}(\mathcal{R}_k^g-\mathcal{R}_{-k}^g), \qquad (2.8)$$

where w_i is the mass fraction of the species i, $\boldsymbol{v}$ is the mass average velocity (appearing in the Navier-Stokes equations), $\mathcal{R}_k^g$ is the rate of reaction in gas phase, ν_{ik} is the stoichiometric coefficient of species i in reaction k.

The diffusive mass flux of species i, $\boldsymbol{j}_i$, is composed of diffusion flux due to concentration gradients and diffusion flux due to the temperature gradients, i.e.,

$$\boldsymbol{j}_i = \boldsymbol{j}_i^C + \boldsymbol{j}_i^T, \tag{2.9}$$

or

$$\boldsymbol{j}_i = \frac{C^2}{\rho} \sum_{j=1, j\neq i}^{n} M_i M_j \mathcal{D}_{ij} \boldsymbol{d}_j - \mathcal{D}_i^T \nabla \ln T, \tag{2.10}$$

where $\mathcal{D}_{ij}$ is the multicomponent diffusion coefficient matrix for the species pair i j, C is molar concentration of the mixture, and $\mathcal{D}_i^T$ is the multicomponent thermal diffusion coefficient for species i; $\mathcal{D}_i^T$ is greater than 0 for large, heavy molecules, and less than 0 for small, light molecules. M_i, M_j are the molecular weight of species i and species j, respectively. $\boldsymbol{d}_i$ is mechanical diffusion vector for species i and defined as

$$\boldsymbol{d}_i = \frac{y_i}{a_i} (\nabla a_i)_{P,T}, \tag{2.11}$$

where y_i is the mole fraction of species i in the mixture, and a_i is the activity coefficient of species i in the mixture. For an ideal gas mixture, the activity is equal to the mole fraction, and Eq. (2.11) becomes

$$\boldsymbol{d}_i = \nabla y_i, \tag{2.12}$$

and equation (2.10) is simplified to

$$\boldsymbol{j}_i = \frac{C^2}{\rho} \sum_{j=1, j\neq i}^{N} M_i M_j \mathcal{D}_{ij} \nabla y_i - \mathcal{D}_i^T \frac{\nabla T}{T}. \tag{2.13}$$

The following equations are used to convert the mole fraction to mass fraction:

$$y_i = \frac{M}{M_i} w_i , \tag{2.14}$$

$$y_i = \frac{w_i}{M_i}\left[\sum_{j=1}^{N} \frac{w_j}{M_j}\right]^{-1} , \tag{2.15}$$

where M is the mean molecular weight of gas mixture, and can be expressed as

$$M = \frac{\rho}{C} = \left[\sum_{i=1}^{N} \frac{w_i}{M_i}\right]^{-1} . \tag{2.16}$$

Substituting Eq. (2.14), and Eq. (2.16) into Eq. (2.13) yields

$$\boldsymbol{j}_i = \rho \frac{M_i}{M} \sum_{j \neq i}^{N} \mathcal{D}_{ij} \left(\nabla w_j + w_j \frac{\nabla M}{M} \right) - \mathcal{D}_i^T \nabla (\ln T) . \tag{2.17}$$

In an N component gas mixture, there are N-1 independent species concentrations since the mass fractions must sum up to 1, the summation of diffusive mass flux must be zero. Thus,

$$\sum_{i=1}^{N} w_i = 1 , \tag{2.18}$$

and

$$\sum_{i=1}^{n} \boldsymbol{j}_i = 0 . \tag{2.19}$$

2.1.4 Boundary Conditions

To solve the transport equations described above, a set of self-consistent boundary conditions must be specified for each equation. Boundary conditions for the velocity, temperature, and species concentrations for non-reacting walls, substrate, inlet, and outlet are described in this section. The pressure at one point—either at the inlet or outlet—is specified as the background pressure, taken to be the reactor pressure reported from the experiments.

Nonreacting Walls:

For a non-reacting wall, which is any surface other than the substrate, the no slip condition is applied for the velocity. Thus, the velocities for these walls are specified to be zero since the wall is stationary. And an isothermal boundary condition is applied for temperature. The total mass flux normal to these non-reacting walls must be zero for each of the gas species:

$$\boldsymbol{v} = \boldsymbol{0}$$
$$T = T_{wall}$$
$$\boldsymbol{n} \cdot \boldsymbol{j}_i = \boldsymbol{0},$$

where $\boldsymbol{n}$ is a unit vector normal to a non-reacting surface of the wall.

Reacting Surface:

For a reacting surface, specifically the substrate, the temperature is treated as isothermal. In a preliminary study, substrate temperature is set at 300 K. The velocity at the substrate is zero. The mass flux normal to the substrate is set to zero for all species except for the difluoromethylene, CF_2. That specie's mass fraction is set to zero at the reacting surface to simulate the mass transfer limited condition. The

velocity normal to the substrate surface is also set to zero due to the no-slip condition. Thus,

$$
\begin{aligned}
T &= T_{substrate}, \\
\boldsymbol{v} &= 0, \\
w_{CF_2} &= 0, \\
\frac{\partial w_i}{\partial n} &= 0, i \neq \mathrm{CF_2}.
\end{aligned}
$$

Inflow:

The velocity normal to the inlet boundary, which is in the direction of inlet flow, will be equal to the average inlet velocity calculated from feed gas flow rate. The mass fraction of the feed gas equals to 1.

$$
\begin{aligned}
T &= T_{in}, \\
\boldsymbol{n} \cdot \boldsymbol{v} &= v_{in}, \\
w_{HFPO} &= 1.
\end{aligned}
$$

Outflow:

At the outlet, zero gradient for all properties in the direction of flow are assumed:

$$
\begin{aligned}
\boldsymbol{n} \cdot (\nabla \boldsymbol{v}) &= 0, \\
\boldsymbol{n} \cdot (\nabla T) &= 0, \\
\boldsymbol{n} \cdot \boldsymbol{j} &= 0.
\end{aligned}
$$

2.2 Properties of Gas Species

Physical properties of each gas species in the reactor are summarized in Table 2.1. The boiling temperatures in the table were collected from the NIST chemistry webbook [40]. The critical properties are from CRC Handbook [41], and those of hexafluoropropylene oxide (HFPO) were measured by Zytkus [42].

Table 2.1 Physical properties and Lennard-Jones parameters of the gas species

Materials	*M*	T_b *(K)*	T_c *(K)*	P_c *(MPa)*	V_c *(cm^3/mole)*	ε/k *(K)*	σ *(Å)*
HFPO	166.02	246	359	2.895	281.39	285.079	5.3013
TFAcF	116.01	214.10	-	-	-	246.215	4.941
CF_2	50.01	–	–	–	–	108.0	3.977
TFE	100.02	196.8	306.5	3.94	172	243.389	4.677

Table 2.1 also shows the Lennard-Jones parameter for each gas species. The Lennard-Jones parameters of HFPO, and TFE are estimated from their critical properties using method of Chung et al. [43]. Since the critical properties of trifluoro-acetyl fluoride (TFAcF) are not available, the values of ε/k and σ are estimated from normal boiling point properties. The molar volume of the trifluoroacetyl fluoride (TFAcF) is estimated from the density of the liquid at normal boiling point, reported by Pace and Hodge [44]

$$\frac{\varepsilon}{k} = \frac{T_c}{1.2593} \text{ or } \frac{\varepsilon}{k} = 1.15T_b, \tag{2.19}$$

$$\sigma = 0.809V_c^{1/3} \text{ or } \sigma = 1.166V_{b,l}^{1/3}, \tag{2.20}$$

where ε is the maximum energy of attraction.

σ is the collision diameter

T_b is the normal boiling point temperature

T_c is the critical temperature

V_c is the critical volume

$V_{b,l}$ is the molar volume of liquid at the normal boiling point.

2.2.1 Calculation of Thermophysical Properties

The density of pure gas is calculated from the ideal gas law,

$$\rho = \frac{PM}{RT}, \tag{2.21}$$

where M is molecular weight of the pure gas, R is the universal gas constant, P and T are the local pressure and temperature, respectively.

The viscosity and thermal conductivity of the fluid are also estimated from kinetic theory [43],

$$\mu_i = 2.6693\times10^{-6}\frac{\sqrt{M_i T}}{\sigma_i^2 \Omega_\mu}, \tag{2.22}$$

where μ is in kg/m·s, T is in Kelvin, $T^* = kT/\varepsilon$, $\Omega_\mu(T^*)$ is the collision integral, σ_i is collision diameter, and ε is characteristic energy in the 12-6 Lennard-Jones potential function. Values of σ and ε/k are listed in Table 2.1. Neufeld et al. [45] proposed an empirical equation for calculating collision integral as:

$$\Omega_\mu = \left[A/(T^*)^B\right] + \left[C/\exp(DT^*)\right] + \left[E/\exp(FT^*)\right], \tag{2.23}$$

where the coefficients for the Ω_μ in the above equation are A = 1.16145, B = 0.14874, C = 0.52487, D = 0.77320, E = 2.16178, and F = 2.43787. All other coefficients can be found in Neufeld et al. [45]. Eq. (2.23) is applicable in the range of $0.3 \leq T^* \leq 100$ with an average deviation of only 0.064 percent.

The thermal conductivity of pure gas is calculated by the Eucken correlation [43]:

$$\lambda_i = \frac{15}{4}\frac{R\mu_i}{M_i}\left[\frac{4}{15}\frac{c_{pi}M_i}{R} + \frac{1}{3}\right]. \tag{2.24}$$

Specific heat capacities of tetrafluoroethylene (TFE) and difluoro-methylene (CF_2) are calculated using the following polynomial form, with c_p in J/mol K [46] and T in Kelvin.

$$c_p = A + BT + CT^2 + DT^3 + \frac{E}{T^2}. \tag{2.25}$$

The coefficients A, B, C, D are listed in Table 2.2. The original data of the specific heat of tetrafluoroethylene and difluoromethylene are shown in Appendix A. The specific heat of HFPO and TFAcF is estimated using CACHE, which is molecular mechanics program, since the experimental values are not available in the literature. The specific heat obtained from the calculations were fitted using least square method into the following polynomial form with c_P in J/kg·K,

$$c_p = A + BT + CT^2 + DT^3 + ET^4 + FT^5 + GT^6. \tag{2.26}$$

The curve fitting are shown in Appendix A. The coefficients *A, B, C, D, E, F,* and *G* in Eq.(2.26) are listed in Table 2.3.

Table 2.2 Polynomial coefficients for calculating specific heat capacity of trifluoroethylene and difluoromethylene [46], Eq. (2.25)

	TFE		CF_2	
	298-1100 (K)	1100-6000 (K)	298-600 (K)	600-2000 (K)
A	43.55126	129.9776	8.825772	59.34753
B	175.9079	1.690919	125.3652	-2.317176
C	-138.7331	-0.340087	-129.4940	0.890518
D	40.35619	0.023448	50.33101	-0.055879
E	-0.381260	-10.83204	0.259749	-3.467545

Table 2.3 Polynomial coefficients for calculating specific heat capacity of HFPO and trifluoroacetyl fluoride, Eq. (2.26)

	HFPO	*TFAcF*
A	27.173466	84.877581
B	4.3986935	4.1695413
C	-1.0330651×10^{-2}	-1.0123372×10^{-2}
D	1.8675535×10^{-5}	1.8178686×10^{-5}
E	-2.1460597×10^{-8}	-2.0297402×10^{-8}
F	1.3318069×10^{-11}	1.2207946×10^{-11}
G	-3.3790579×10^{-15}	-3.0124388×10^{-15}

2.3 Chemistry of the Gas Species

The chemistry of the gaseous species in a HFCVD system is assumed to follow a three step process. First, the feed HFPO decomposes into difluorocarbene radical (CF_2) and trifluoroacetyl fluoride (CF_3COF), which can be considered as the initiation step in the polymerization. Secondly, the difluorocarbene radicals combine

with one another to form tetrafluoroethylene (TFE). Finally, either TFE itself or TFE and difluorocarbene recombine to form a longer chain of polytetrafluoroethylene, which is called the polymerization step. The kinetic studies of these reactions that found in the literatures are presented in this section.

2.3.1 Pyrolysis of Hexafluoropropylene Oxide

The pyrolysis of hexafluoropropylene oxide (HFPO) has been used widely to generate difluorocarbene. HFPO is known to thermally decompose above 150 °C, and forms trifluoroacetyl fluoride and difluorocarbene as the primary products [47-48]. This pyrolysis process is reversible, and HFPO can be formed by adding difluorocarbene to trifluoroacetyl fluoride [48]. In the absence of other reacting species, CF_2 will react with itself to produce tetrafluoroethylene [47-48]. The reactions describing gas phase decomposition of HFPO and CF_2 recombination in a HFCVD reactor are

$$CF_3CFOCF_2 \xrightarrow{\Delta} CF_3CFOF + CF_2 \qquad (2.25)$$

$$2CF_2 \rightleftharpoons CF_2{=}CF_2 \,. \qquad (2.26)$$

FTIR analysis of the effluent from the HFCVD reactor identify the presence of only unreacted HFPO, trifluoroacetyl fluoride (TFAcF), and trifluoroethylene (TFE) during HFPO HFCVD deposition [25]. This indicates that the above decomposition mechanism occurred during deposition, and that the deposition rate may be controlled by decomposition of HFPO in the gas phase.

The first order rate constant (k) of hexafluopropylene oxide pyrolysis at temperatures between 141 °C and 257 °C was measured by Kennedy and Levy [47]. The following rate constant expression was obtained from Kennedy's least squares fit:

$$k = 10^{13.2 \pm 0.2}\, e^{(-36{,}300 \pm 500)/RT},$$

with k in s^{-1}, and activation energy, E_a, in cal/mole. The activation energy reported by Knickelbein et al. [49] using pulsed pyrolysis is 31 kcal/mole, which is about 15% lower than the activation energy shown in the above expression, and is remarkably close to the activation energy measured for the thermal decomposition of tetrafluoroethylene oxide (~31.6 kcal/mole) [50], which undergoes decomposition at lower temperature (120 °C to 140 °C). The activation energy obtained from the Arrhenius plot of deposition rate as a function of inverse hot filament temperature of HFPO pyrolytic CVD (about 29 ± 4 kcal/mol) is surprisingly close to Knickelbein's value considering the experimental errors [23]. However, these methods used by Knickelbein and Gleason, are not the direct measurement of HFPO decomposition. Their activation energy is quite low compared with the activation energy of Kenedy and Levy. In addition, many researchers have been measured the kinetics of HFPO decomposition by different methods, and found rates which agree with the value reported by Kenedy and Levy. The rate constant and the activation energy from various publications are summarized in Table 2.4.

Table 2.4 Rate constant for unimolecular decomposition of hexafluoro-propylene oxide (HFPO)

logA (s^{-1})	*Ea (kcal/mol)*	*Tempereature Range*	*Measuring Method*
13.2±0.2	36.9±0.5	414-530 K	Static pyrolysis [47]
13.41±0.15	37.2±0.3	423-523 K	Static pyrolysis [51]
14.5 ±0.2	39.7±1.2	$T \leq 735$ K	Adiabatic compression [52]
13.8±0.2	36.5±1	400-750 K	Pulsed laser pyrolysis in C_3F_6O-SF_6 mixture [53]
14.2±0.5	37.9±1	463-503 K	Thermal pyrolysis [54]

2.3.2 Recombination of the Difluorocarbene

Hexafluoropropylene oxide undergoes unimolecular decomposition to trifluoroacetyl fluoride and difluorocarbene (CF_2) between 160 to 250 °C. The primary stable products of this process are trifluoroacetyl fluoride, tetrafluoroethylene (C_2F_4) and perfluorocyclopropane (cyclo-C_3F_6) [47-48]. However, tetrafluoroethylene and perfluorocyclopropane are formed by the dimerization of CF_2 radical, and the combination of CF_2 to C_2F_4, respectively. The formation of perfluorocyclopropane proceeds through the insertion of CF_2 into the π-component of tetrafluoroethylene double bond [55]. The rate constant for dimerization of CF_2 has been determined by Dalby using flash photolysis of tetrafluoroethylene and perfluorocyclopropylene [56]. The disappearance of CF_2 follows a second order rate equation in the temperature range 298 to 572 K. The dimerization of CF_2 to tetrafluoroethylene

$$CF_2 + CF_2 \xrightarrow{k_1} C_2F_4, \qquad (2.27)$$

is the dominant process for removal of CF_2 in the gas phase, where k_1 is the second-order rate constant in liter/mol·sec, which is defined as

$$\frac{d[CF_2]}{dt} = -k_1[CF_2]^2 . \tag{2.28}$$

The constant has been determined to be $k_1 = 1.3\times10^8 (T/300^\circ K)^{1/2} e^{(-1200\pm200)/RT}$ liter/mol·sec, where R is the gas constant in cal/mol·K, T is the absolute temperature, and the activation energy of the reaction is in cal/mol. The reaction constant varies by less than a factor of 2 when tetrafluoroethylene pressures vary from 0.2 to 50 cm Hg [56]. Tyerman [57] has reinvestigated the dimerization of CF_2 in flash photolyzed C_2F_4, and CF_2CFCl, and reported the rate constant as

$$k_1^{'} = (2.5\pm0.5)10^6 T^{1/2} \exp(-200\pm50)/T \text{ liters/mol}\cdot\text{s},$$

where $k_1^{'}$ is defined as

$$\frac{d[CF_2]}{dt} = -2k_1^{'}[CF_2]^2 . \tag{2.29}$$

Except for the association reaction, CF_2 is a rather unreactive molecule, and shows such a low reactivity with tetrafluoroethylene molecules. The CF_2 addition to tetrafluoroethylene is negligible compared to CF_2 dimerization. Atkinson and McKeagan [58] measured the reaction rate of

$$CF_2 + C_2F_4 \xrightarrow{k_2} (CF_2)_3, \tag{2.30}$$

and reported a rate constant of

$$k_2 = 10^{6.09} T^{1/2} \exp(-8500/RT) \text{ liters/mol.s}.$$

The rate constant of perfluorocyclopropane decomposition, $k_2^{'}$, which is the reverse reaction of Equation (2.30), is determined at 253 to 276 °C to be

$$k_2^{'} = 10^{13.25} \exp(-38600/RT) \text{ s}^{-1},$$

no variation with pressure over the range 2 to16 cm Hg. Cohen and Heickien [59] measured the rate of the addition of CF_2 to C_2F_4 using mercury-sensitized photolysis of C_2F_4, and reported the rate constant ratio, $k_2/k_1^{1/2}$, to be 395 exp(-6700/RT) (liter/mole·s)$^{1/2}$. Recently, Mel'nikovich and Moin [55] have investigated the reaction of CF_2 with C_2F_4, by a competing reaction technique in the 160 to 240 °C interval, at atmospheric pressure. In their experiments, the CF_2 was obtained by thermal decomposition of hexafluoropropylene oxide. Their reported rate constant for the addition of CF_2 to C_2F_4 is $k_2 = 10^{9.96\pm0.44} \exp(-7100 \pm 1100/RT)$ cm^3/mole·s, which is close to the value reported by Cohen and Heickien and a little bit lower than the value reported by Atkinson and McKeagan.

2.3.3 Fluorocarbene Polymerization

From the decomposition mechanism of HFPO, Eqs. (2.25) and (2.26), there are two possible pathways for polymerization of the fluorocarbene, CF_2. One is through addition of a singlet CF_2 to an existing CF_2 chain. The other is the addition of a singlet CF_2 to an existing perfluoroalkene molecule which involves the breaking of a double bond in perfluoroalkene molecule [25],

$$CF_2 + (CF_2)_n \rightarrow (CF_2)_{n+1}, \quad (2.31)$$

$$CF_2 + CF_2CF(CF_2)_n \rightarrow (CF_2)_{n+1}. \quad (2.32)$$

The first pathway, Eq. (2.31), appears to be more favorable than the latter, Eq. (2.32), because of the high stability of the CF_2= CF_2 double bond (ΔH_f ~ -161.1 kcal/mole). The addition of singlet CF_2 to the unterminated CF_2 chain is independent of the chain length (for $n \geq 2$). The heat of reaction for adding a singlet CF_2 into CF_2 chain is only about -49 kcal/mole [25]. It is still unclear whether the polymerization of CF_2 radicals occurs in the gas phase or at the substrate. It is also possible that the polymerization occurs in both locations since some white powder was observed on the substrate in some experiments [49]. This white powder is possibly PTFE formed from polymerization reactions occurring in the gas phase during the HFCVD deposition.

2.4 Simulation of a Hot Filament Cylindrical Reactor

The following section will demonstrate the applicability of the model by simulating the deposition of fluorocarbon films in a cylindrical HFCVD reactor. The results obtained from this simulation will be compared with those from the experiments.

2.4.1 Grid Generation

Calculations were done for two different reactor configurations, one used by Lau et al. to deposit HFCVD films [25], the other a modified version of Lau et al.'s reactor having a different inflow manifold configuration. The first reactor configuration is shown in Figure 2.1. The diameter of the inlet tube is about 3 mm, the substrate diameter is 11.43 cm, and the space above the substrate is 10.16 cm. All other dimensions are shown in Figure 2.1. The second reactor used a showerhead as the inlet feed, with the overhead above substrate reduced to 4 cm. All other dimensions

are the same as the first reactor. The hot filaments were placed 1.5 cm above the substrate for the reactor without the showerhead, and 1 cm for the reactor with the showerhead. Figures 2.2, and 2.3 show computational grids for the reactor without showerhead, and grids for the reactor with the showerhead, respectively. Both grids were generated by the Gambit Program Version 1.2 (Fluent Inc.). The smallest grid size is about 1 mm, corresponding to the grid near the inlet and hot filament, and the biggest grid size is about 0.5 cm, near the outer wall of the reactor. The grids at the outer circumference of the reactor are tetrahedral grids, whereas the grids at the center of the reactor are structured grids.

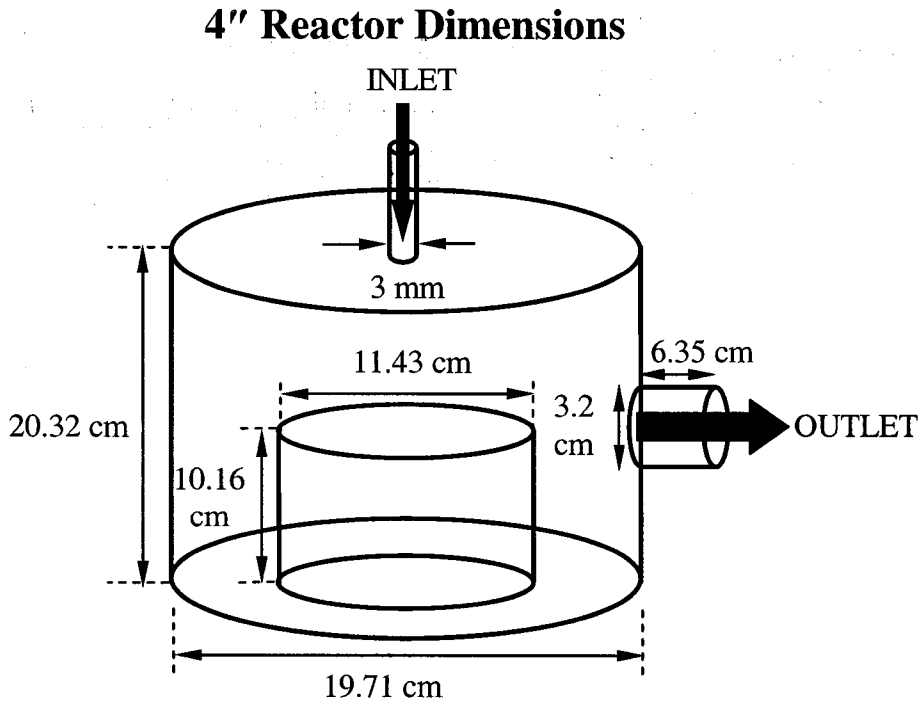

Figure 2.1 Reactor configuration.

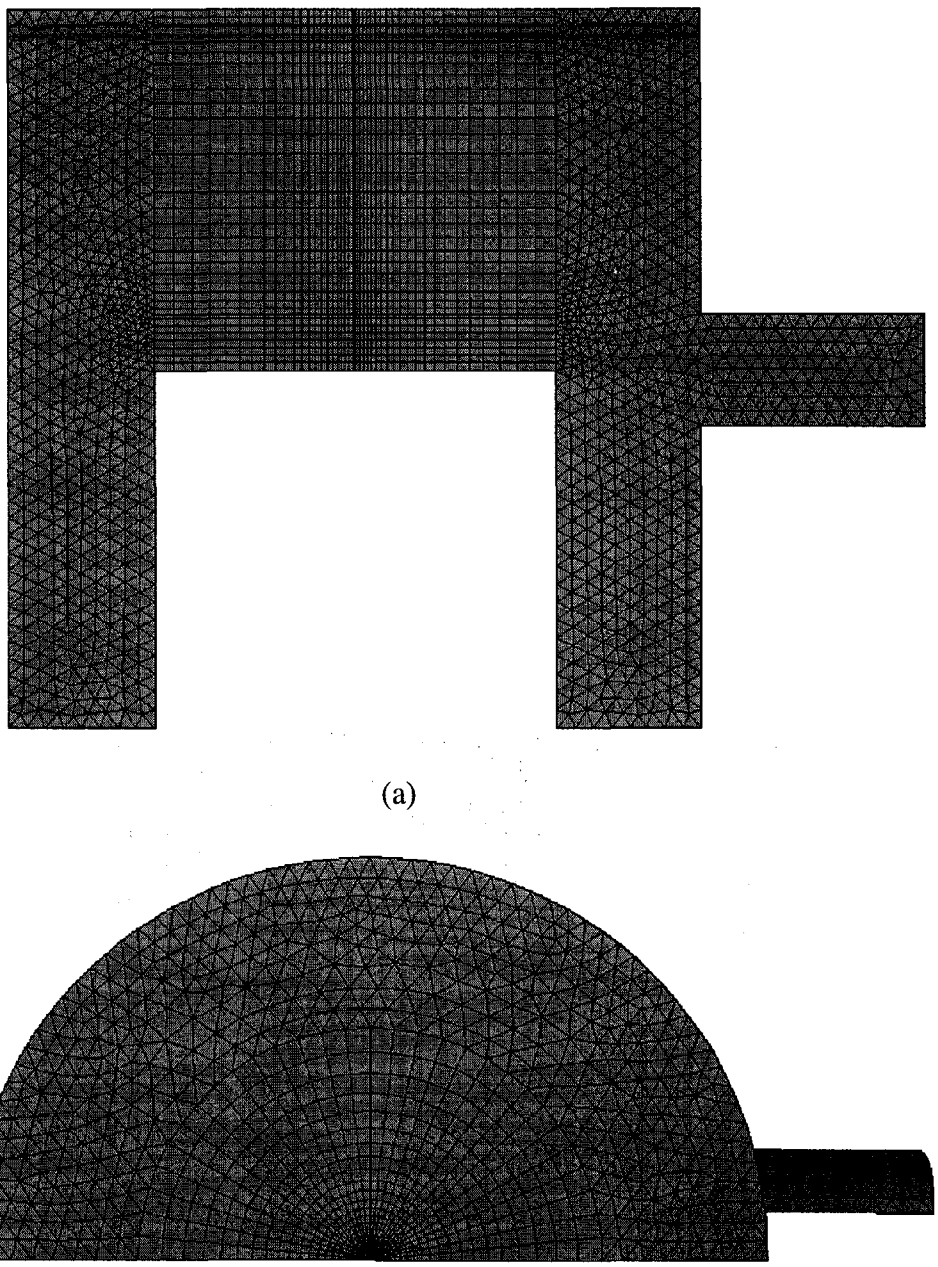

(a)

(b)

Figure 2.2 The grids for reactor without showerhead. The top figure, (a), shows cross-sectional view of the reactor, and the bottom figure, (b), shows the top view of the reactor.

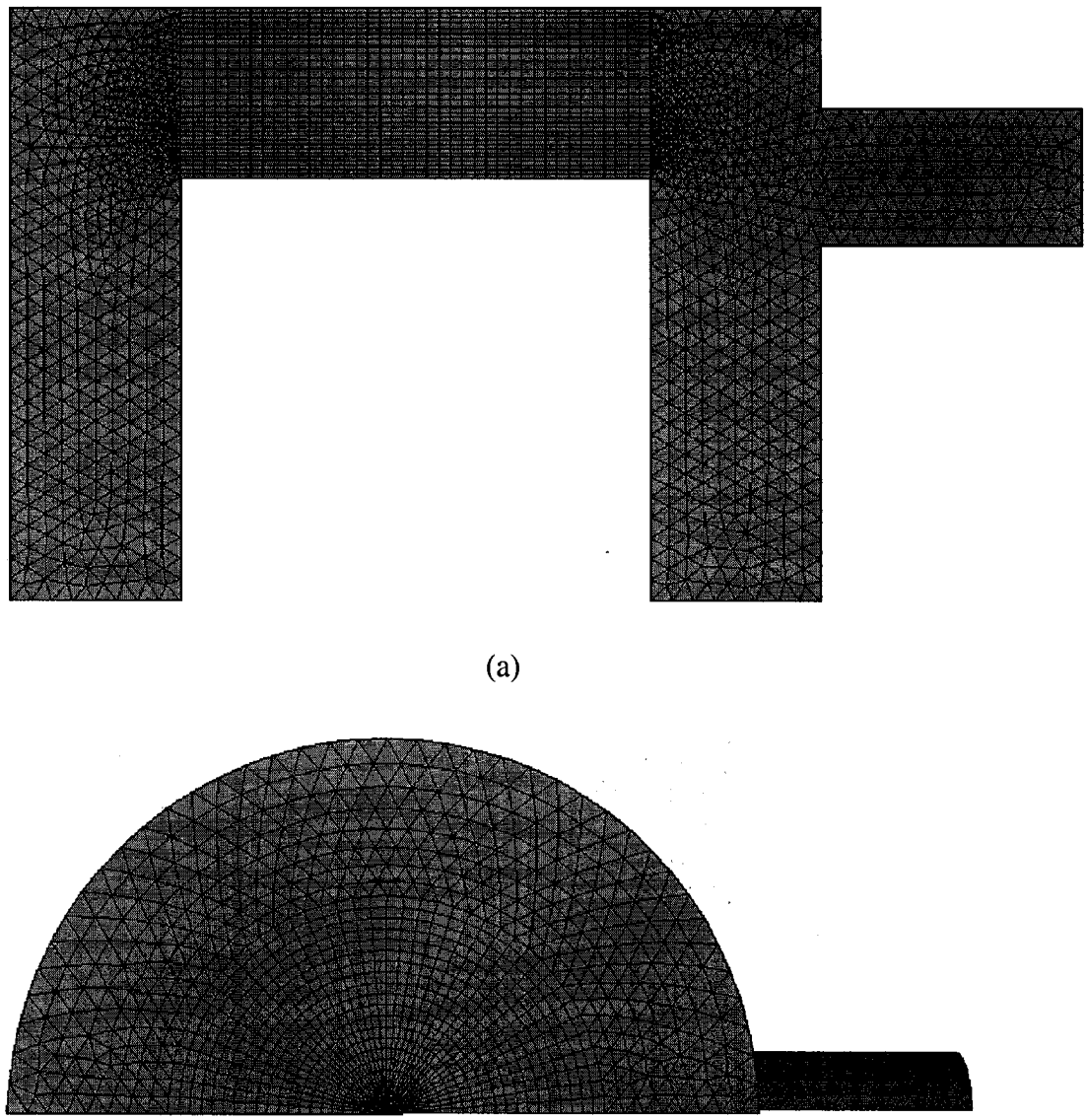

Figure 2.3 **The grid for a reactor with showerhead. The top figure, (a), shows cross-sectional view of the reactor, and the bottom figure, (b), shows top view of the reactor.**

2.4.2 Method of Calculation

The Fluent program (Fluent Inc.) is used to solve the appropriate transport equations presented in the previous section. The momentum, energy, and species transport equations were solved using a segregated method, meaning that these equations were not solved simultaneously, but rather sequentially, in an iterative manner. Fluent uses the finite volume method to discretize the governing equations for a set of algebraic equations that can then be solved numerically. A second order upwind scheme is used to interpolate the quantities at cell faces. The gradient terms or diffusion terms, are calculated using the central difference method, which is second order accurate. The pressure-velocity coupling is solved by Simplec method [60]. The linear algebraic equations obtained from the discretization method are solved by point-implicit Gauss-Seidal method.

2.4.3 Results of the Calculations

The calculations were done for the two different reactor configurations, with and without the showerhead, as described in the previous section. Figure 2.4 shows a representative velocity vector plot of the flow in the plane of symmetry for the reactor with no showerhead. Conditions used in calculations were 48 m/s inlet velocity (corresponding to 30 sccm flow rate), 1 torr pressure at the inlet, and 0.3 W/cm^3 heat generation rate in the hot filament zone. The minimum velocity was 3×10^{-5} m/s, and occurred at the bottom of the reactor, while the maximum velocity was the value of 48 m/s at the inlet. Gas recirculation in the reactor occurred around the centerline in a toroidal pattern. The higher velocity inlet jet prevented this recirculation from occurring at the axis of the reactor, and also acted to cool down the

gas near the hot filament array, as can be seen from Figure 2.5. The non-uniform flow and temperature profiles correlated directly to non-uniform thickness of films deposited in this reactor. A typical film deposited in this reactor is shown in Figure 2.6. The different colors on the film surface results from different film thickness. Films near the wafer edge are thinner than at the wafer center. The calculated results also demonstrate the non-uniform flow over substrate as can be seen in the path line plot (Figure 2.7). The gas was in closer contact with the substrate at the center than at the edge. The results demonstrate the effects of the reactor geometry on the film uniformity.

Calculations were performed to observe the effects of the flow for the same reactor by increasing the flow rate. The results showed increasingly non-uniform temperature contours, with recirculation still occurring over the substrate in more complicated patterns. When the geometry of the reactor was changed by decreasing the overhead space above the substrate through the use of a showerhead inlet, both the velocity vector plots and temperature contours (Figure 2.8, and 2.9), calculated from this new geometry showed significant improvements. Recirculation zones disappeared and the temperature was significantly more uniform above the substrate area.

Although there are no direct experimental data to validate the improvement in the film properties, the geometry of the reactor such as the overhead space above the substrate, inlet size and characteristics, outlet size and position are known from other studies to have significant effects on the quality of the deposited films [61-62].

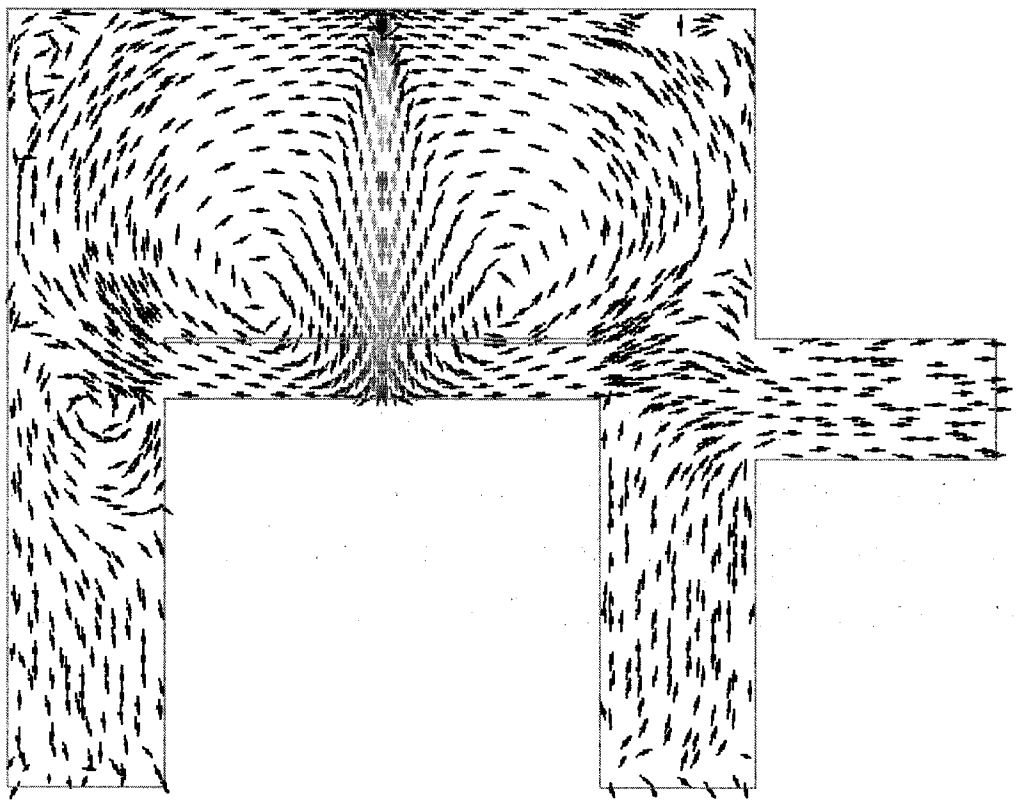

Figure 2.4 **Velocity vector plot of original reactor calculated at 48 m/s inlet velocity (30 sccm inlet flowrate), 1 torr pressure, 300 K substrate temperature.**

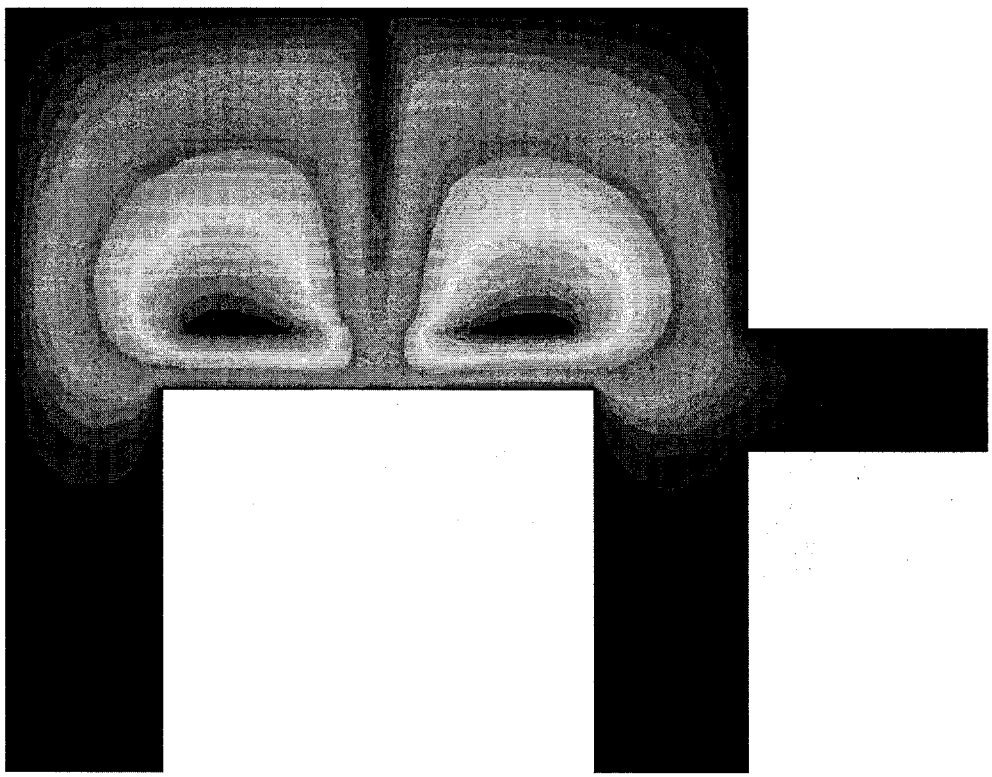

Figure 2.5 **Temperature contour of original reactor calculated at 48 m/s inlet velocity (30 sccm inlet flow rate), 1 torr pressure, and 300 K substrate temperature**

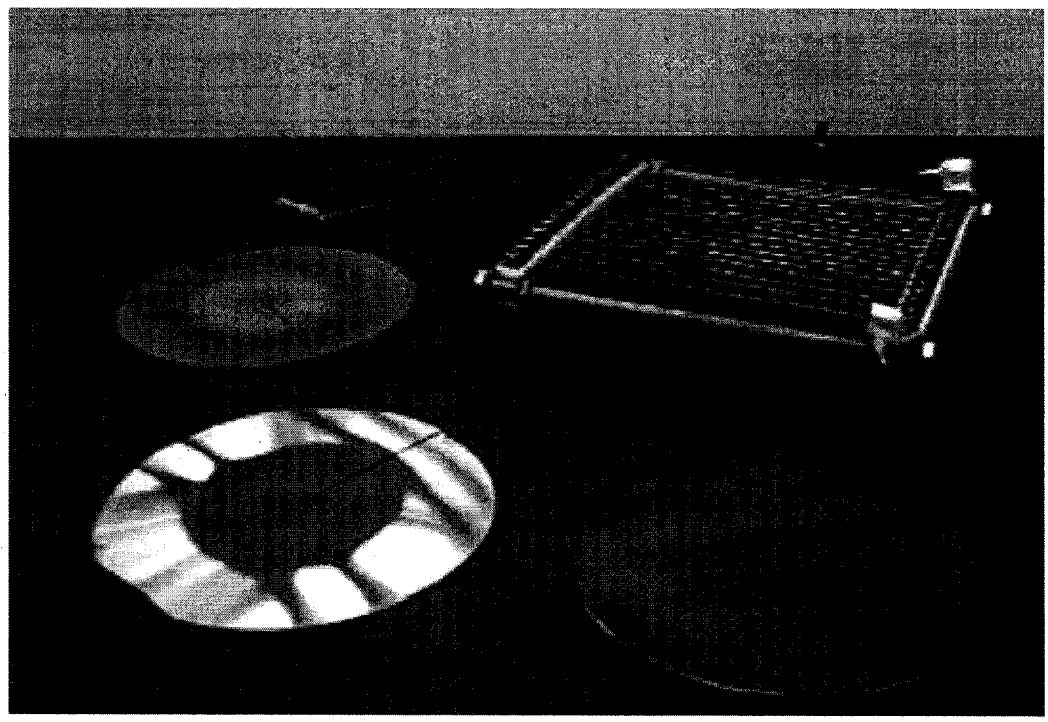

Figure 2.6 Example of films deposited by HFPO HFCVD [63].

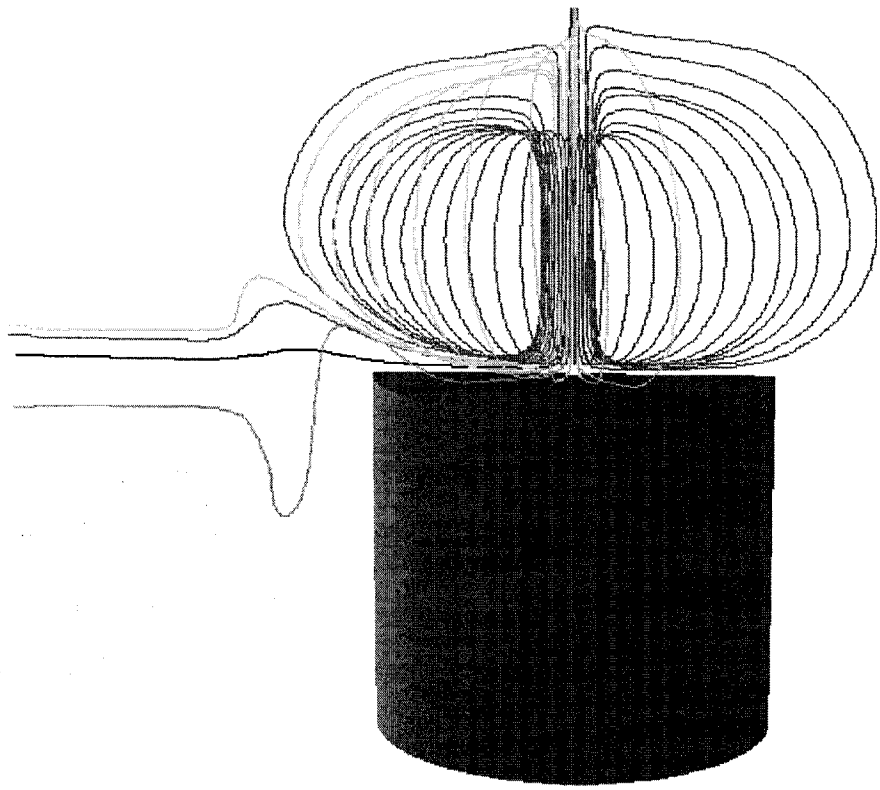

Figure 2.7 **Pathline plot of original reactor calculated at 48 m/s inlet velocity (30 sccm inlet flow rate), 1 torr pressure, 300 K substrate temperature.**

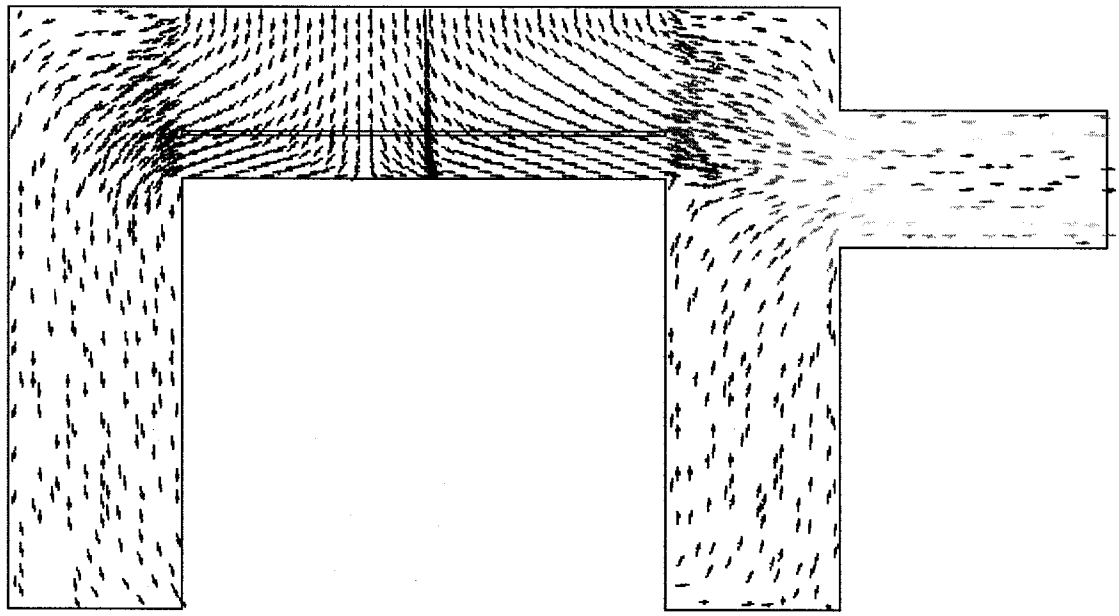

Figure 2.8 **Velocity vector plot of the showerhead reactor, calculated at 0.4 m/s inlet velocity (300 sccm inlet flow rate), and 1 torr pressure, 300 K substrate temperature.**

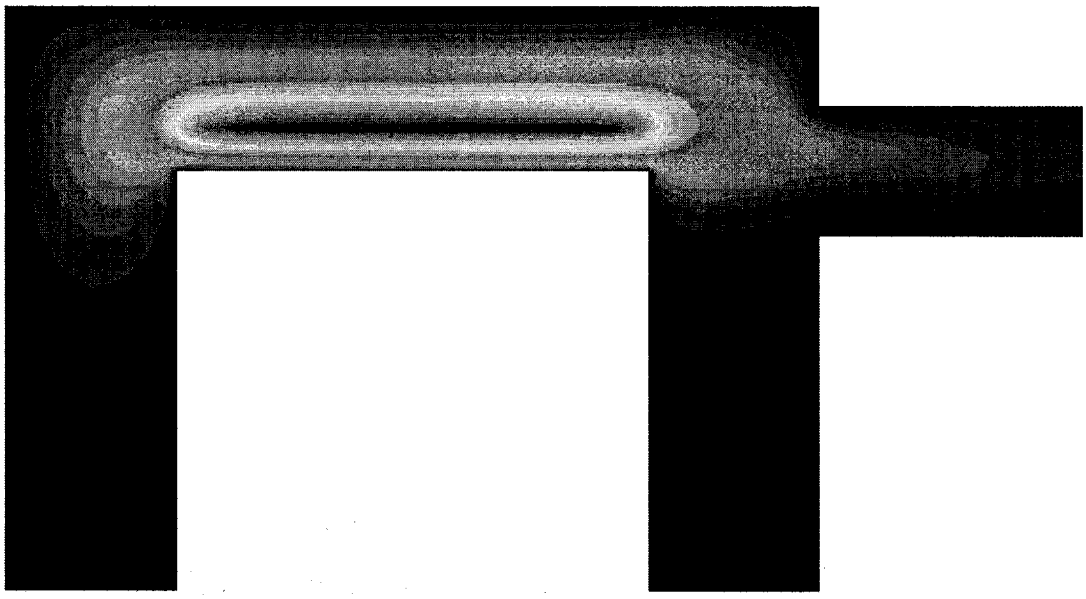

Figure 2.9 **Temperature contour at the symmetric plane for the showerhead reactor, calculated at 0.4 m/s inlet velocity (300 sccm inlet flow rate), and 1 torr pressure, 300 K substrate temperature.**

2.5 Summary

Limited information on the physical and thermodynamic properties of the species involved in the fluorocarbon films deposition has been found in literatures. Some of these properties are calculated from the method and tool available at present time. Although the actual error can not be estimated, the simulation shows the interesting results. In contrast, the kinetics of hexafluoropropylene oxide decomposition has been widely investigated and published. The decomposition of this materials results in the CF_2 which will recombine to tetrafluorethylene and some perfluorocyclopropane. The kinetics of the CF_2 recombination and the combination of CF_2 to C_2F_4 are also well known. The remaining process that has limited kinetic data is the addition of CF_2 into polytetrafluoroethylene chains.

By applying the momentum, and energy equations presented in this chapter to a cylindrical hot filament reactor, the model can capture the recirculation of the flow. This recirculation is related to the non-uniformity of films deposited by this reactor. When the reactor geometry was changed, the recirculation disappeared. This result indicates the effect of flow and the reactor geometry on the reactor performance, and the capability of model for designing the new type of reactor.

Chapter 3

SIMULATION OF AN INLET MANIFOLD SHOWERHEAD CONFIGURATION

The overall objectives of the hot filament chemical vapor deposition reactor (HFCVD) modeling studies are: (1) to design a horizontal flow reactor where the flow, temperature, and concentration profiles over the substrate are uniform, and (2) to develop a gas phase reaction and surface reaction mechanism for application to process optimization. The following studies are directed toward the first objective, namely the design of a new one-dimensional flow HFCVD reactor, shown schematically in Figure 3.1, using computational fluid dynamics (CFD) approach. In the process of designing a CVD reactor, the first step is to determine appropriate configuration for the inlet showerhead that will result in a uniform inlet flow across the area where the substrate would be located and to investigate the sensitivity of the inlet flow characteristics on the showerhead configuration. Generally, uniform inlet flow is assumed as the gas passes through the showerhead. This assumption is not always appropriate due to inefficient mixing of the individual jet streams leaving the shower-head, edge effects, etc [64]. There are several steps in the overall reactor modeling process, and the first step is determining the appropriate inlet velocity profiles. Once an optimal inlet profile is determined, it will be used to design the reactor characteristics, including the overall dimensions, the space between the substrate and the reactor wall, and the location of the substrate in the reactor. The objectives of the following studies are to determine what type of the velocity profiles

will be obtained when the inlet showerhead configuration is changed and what would be realistic profiles to be used in the simulation for the future studies and how far downstream from the inlet is required for the flow to become fully developed.

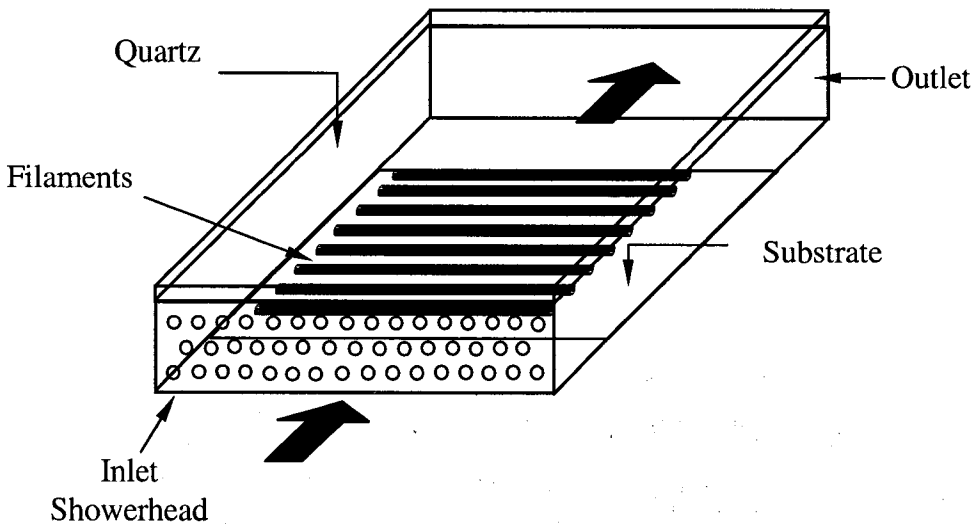

Figure 3.1 Schematic Diagram of a Horizontal Flow HFCVD Reactor.

Simulating a complete showerhead is not possible because of the large number of holes and the disparate scales involved. Instead, small sections of the rectangular chamber with a few holes, which represent a "unit cell" of the inlet showerhead, were used in these studies to investigate the effects of hole diameter, spacing between holes, and space near the reactor walls in the showerhead, on the entrance length, and the velocity profiles in the reactor chamber. After this a larger

rectangular chamber with higher number of shower head holes is simulated to check the effect of the chamber size on the velocity profiles.

The objectives of the following studies are to investigate the effects of the spacing between holes in the showerhead, space near the walls, and the diameter of the showerhead holes. The inlet showerhead configuration certainly affects the velocity profiles as well as the entrance length, i.e., the distance required to realize a uniform flow field that is independent of the specific inlet geometry. The intent of the showerhead is to evenly distribute the flow across its surface area, and generally consists of a large number of holes, each with very small diameter. The ideal configuration is an array of very small, closely spaced holes. However, the smaller the diameter, the higher the cost of the showerhead due to manufacturing challenges, and the larger pressure drop required to obtain a desired flow rate. The following studies will determine how small the showerhead holes need to be to achieve uniform flow, how sensitive the details of the flow are to changes in hole spacing, hole diameter, and space near the walls. This chapter is divided into six sections: (1) the effects of the spacing between holes, (2) the showerhead hole diameter, and (3) the space near the walls on the velocity profiles and entrance length are presented in the first three sections. The fourth section presents the scale-up effects on the velocity profiles. Last, an analytical expression obtained from solving for the Poiseuille flow field in a rectangular chamber, and the summary are presented in sections five and six, respectively.

3.1 Effect of the Showerhead Hole Spacing

In this study, four configurations of the showerhead with different hole spacings are considered. Figure 3.2 shows the general configuration of the rectangular chamber used in the calculations. The showerhead hole diameter is 1 mm, and the distance from the chamber wall to the holes is 2 mm. The chamber is 3 mm high and 30 mm long. The width of the chamber ranges from 9 mm to 17 mm based on the space between holes. The space between holes, L, is varied from $1d$ to $5d$, where d is the hole diameter. All these parameters are listed in Table 3.1. The calculations were performed at a temperature of 300 K and 1 torr pressure. The inlet velocity was set at 31 m/s, which corresponds to an inlet Reynolds number of 20 (based on each hole diameter). The Reynolds numbers in the chambers were 4.7, 5.9, 6.8, and 7.9 for the chambers with $5d$, $3d$, $2d$, and $1d$ hole spacing respectively. The corresponding inlet flow rates calculated with these same chamber Reynolds numbers for a reactor with 30 cm × 5 cm cross-sectional area are 335, 286, 252, and 201 sccm for $1d$, $2d$, $3d$, and $5d$ hole spacings, respectively. The Reynolds number is defined as

$$N_{\mathrm{Re}} = \frac{\rho D_h v_{avg}}{\mu}, \tag{3.1}$$

where ρ is gas density, D_h is the hydraulic diameter, defined as four times cross-sectional area divided by wetted perimeter, and v_{avg} is the average velocity, take as the volumetric flow rate divided by the cross-sectional area.

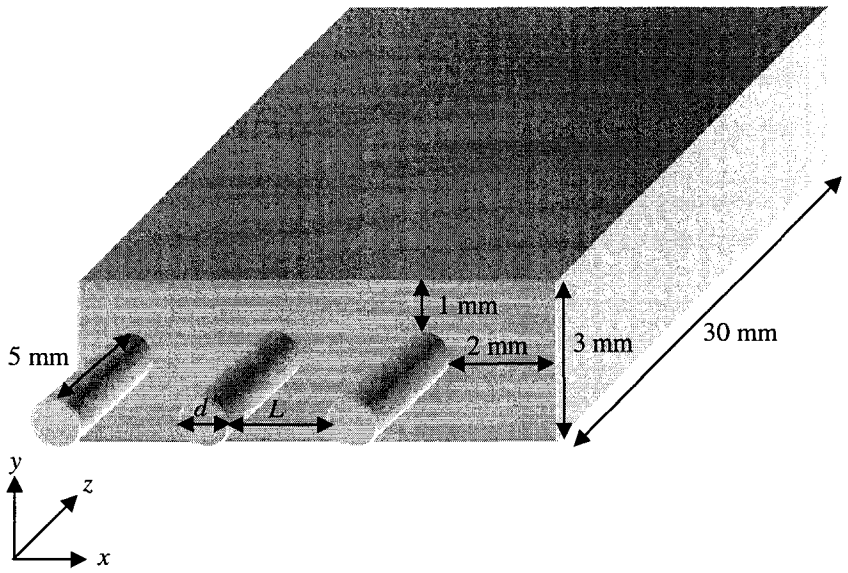

Figure 3.2 **Configuration used in the calculations for studying the effects of hole spacing.**

Table 3.1 **Dimensions of the showerhead used in the calculations for studying the effects of the hole spacing.**

Parameters	
Hole diameter (mm)	1
Hole Spacing (mm)	1, 2, 3, 5
Space between shower holes and chamber side-walls (mm)	2
Space between shower holes and chamber top-walls (mm)	1
Thickness of showerhead (mm)	5
Chamber height (mm)	3
Chamber length (mm)	30
Chamber width (mm)	9, 11, 13, 17

The plots of the dimensionless axial velocity (v_z/v_{avg}) versus the dimensionless axial position (z/D_h) at the centerline of the chamber are shown in Figure 3.3 for the different hole spacings. From these curves, good estimates of the chamber entrance length can be determined. The entrance length is the distance from the inlet to the position where the flow becomes fully developed or the position where the velocity component in the primary direction of flow does not change with position. In this study, the entrance length is determined from the distance from the inlet to the position where the centerline velocity reached 99% of the fully developed velocity. From Figure 3.3, the dimensionless entrance lengths (z/D_h) are 1.4, 1.1, 1.1, and 1.3 for 1*d*, 2*d*, 3*d*, and 5*d* hole spacing, respectively. As shown in Figure 3.3, the increase in hole spacing did not result in any significant change in the entrance lengths.

A plot of the axial velocity profiles as a function of transverse horizontal position, x, (the axes are shown in Figure 3.2) is shown in Figure 3.4. The curves are velocity profiles at 3 mm away from the outlet and at the center of the chamber height. In this figure, the dimensionless transverse horizontal position, x/a, is defined in terms of the chamber width, a, and the axial velocity is once again normalized by the average velocity, v_{avg}. The curve for 1*d* hole spacing is a smooth parabola, whereas the curves for the others are more perturbed from this shape due to discrete influences of the inlet holes. The percentage difference of the velocity in the middle part of the curves for 2*d*, 3*d*, and 5*d* hole spacing is approximately 2.5 to 3%. These fluctuations in the velocity magnitude are still in the acceptable range and can be considered to be uniform profiles. Figure 3.5 shows a path line plot for 1*d*, 2*d*, 3*d*, and 5*d* hole spacing. There is recirculation occurring near the inlet in every cases. The least recirculation occurred for the case of 1*d* hole spacing. For that case, recirculation occurred only on

the sides, not around the middle hole, since the space between showerhead holes and chamber side walls are larger than the hole diameter. The recirculation tends to occur when the space is greater than the hole diameter. This recirculation results in a longer entrance length, as seen from the velocity profiles in Figure 3.3.

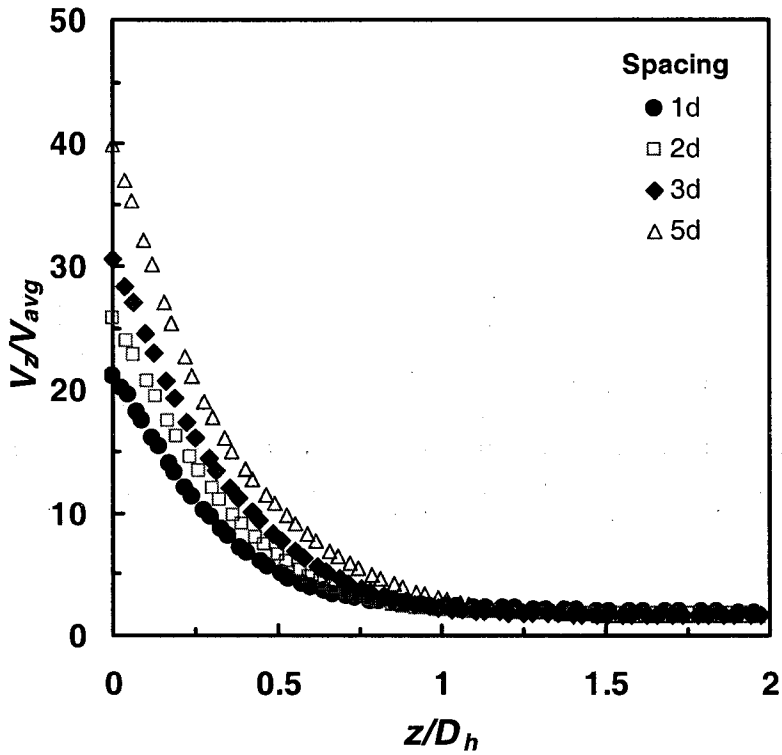

Figure 3.3 **The dimensionless axial velocity (v_z/v_{avg}) at the centerline of the chamber as a function of dimensionless axial position for the inlet showerhead with different hole spacing. The calculations were performed at 300 K, 1 torr, and 31 m/s inlet velocity (N_{Re} ~ 20).**

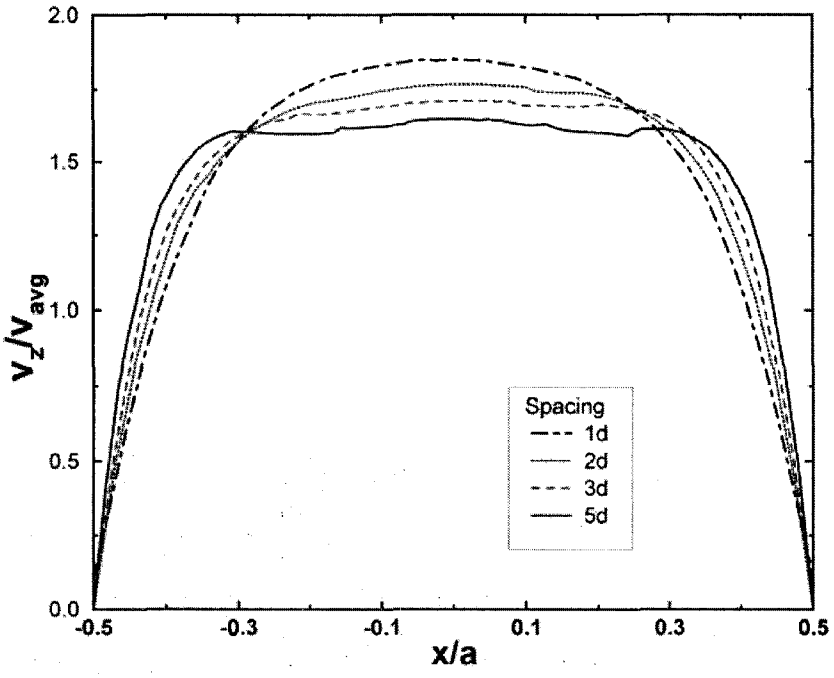

Figure 3.4 **The axial velocity profiles along horizontal axis for the showerhead with different hole spacing. The conditions used in the calculations were 300 K, 1 torr, and 31 m/s inlet velocity (Re ~ 20). The curves were plotted at ~ 3 mm away from the chamber outlet, and at the midpoint of the chamber height.**

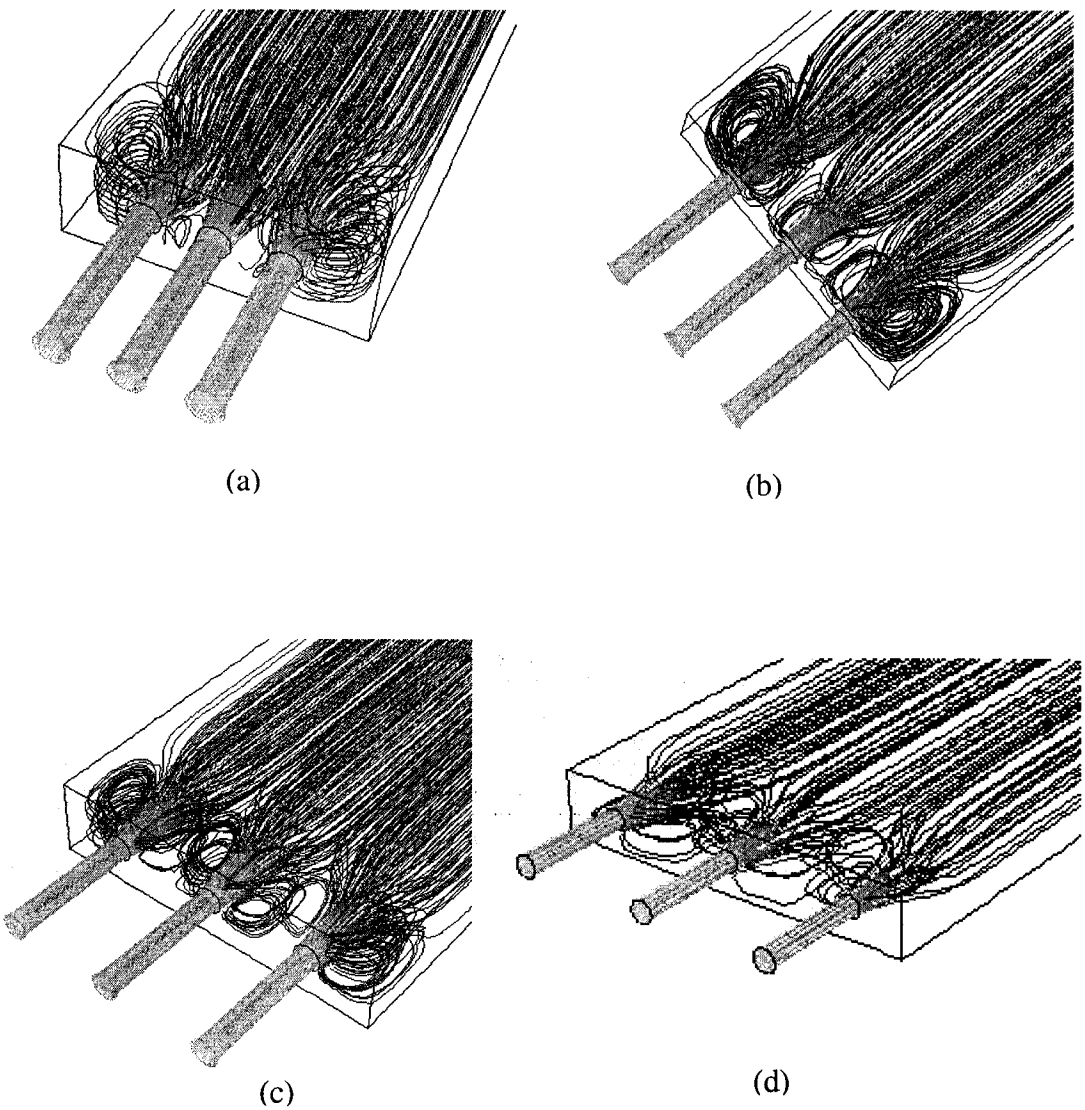

Figure 3.5 The pathlines plot for different hole spacing, (a) 1d, (b) 2d, (c) 3d, and (d) 5d.

The results of this study demonstrate that increasing the hole spacing in the studied range (1 to 5 times the hole diameter) does not change the entrance length significantly, but flattens out the velocity profiles. Rather flat velocity profiles are achieved when spacing is roughly 3 to 5 times the diameter of the holes, but the profiles become distorted in the middle. Strictly speaking, a uniform velocity profile over the substrate surface is required in a CVD reactor to achieve uniform deposition. However, it is impossible in reality to get an ideal uniformity because of no-slip boundary conditions that exist at the walls. The profiles with the extended flat part in the middle, such as those obtained from the case of $3d$ and $5d$ spacing, are considered to be an acceptable uniformity. The velocity profile will be increasingly distorted as the spacing increases, and the assumption of uniform velocity profile will no longer be reasonable.

3.2 Effect of Showerhead Hole Diameter

In this series of calculations, the diameter of the holes in the inlet shower is varied from 1 to 5 mm, while the hole spacing, and the space between holes and chamber wall are fixed at 2 mm. The chambers are 50 mm long (see Table 3.2). The chamber width and height are changed accordingly for each hole diameter. Figure 3.6 shows a schematic drawing of the chamber used in the calculations. The conditions in the chamber are set at 300 K and 1 torr. The inlet velocities are set at 31, 15.5, 10.3, and 6.2 m/s for the 1, 2, 3, and 5 mm hole diameters, respectively, to fix the inlet Reynolds number at 20. The chamber Reynolds numbers are 5.9, 9.5, 11.9, and 14.8, for 1, 2, 3, and 5 mm, respectively. The corresponding inlet flow rates for these chamber Reynolds numbers, calculated for a reactor with 30 cm × 5 cm cross-sectional

area are 251, 402, 502, and 627 sccm for 1, 2, 3, and 5 mm hole diameters, respectively.

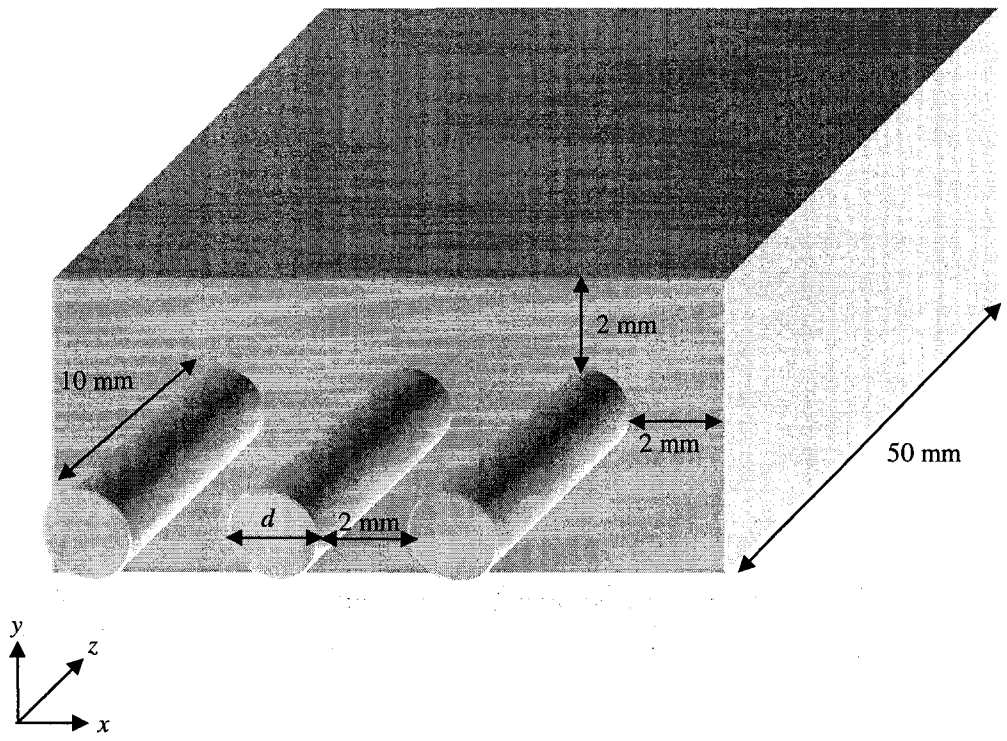

Figure 3.6 Dimensions of the showerhead used in the calculations for studying the effects of the hole diameter.

Table 3.2 Dimensions of the showerhead used in the calculations for studying the effects of the hole diameter. The hole spacing and the space between showerhead hole the chamber wall are fixed at 2mm. The showerhead is 10 mm thick.

Parameters	*Hole Diameter (mm)*			
	1	2	3	5
Chamber height (mm)	5	6	7	9
Chamber length (mm)	50	50	50	50
Chamber width (mm)	11	14	17	23
Inlet velocity (m/s)	31	15.5	10.3	6.2
Inlet Reynolds number	20	20	20	20
Inlet Flow rate (sccm)	251	402	502	627
Chamber Reynolds number	5.9	9.5	11.9	14.8

Figure 3.7 shows the dimensionless z-component of velocity (v_z/v_{avg}) as a function of the dimensionless axial position (z/D_h), for different hole diameters. The plot shows the dimensionless axial velocity along the centerline of the chamber. The dimensionless entrance length (z/D_h) obtained from these plots are 0.9, 0.9, 0.9, and 0.8 for the hole diameters of 1, 2, 3, and 5 mm, respectively. The axial velocity profiles along the x direction, near the chamber outlet plane at the midpoint of the chamber height, are shown in Figure 3.8. The velocity profiles are parabolic for all cases, but are flatter in the middle when the hole diameter increases. The velocity profiles for the 3 and 5 mm holes are much closer quantitatively to each other than those of 1 and 2 mm hole diameter cases. Figure 3.9 shows a pathline plot for the showerhead with1, 2, 3, and 5 mm hole diameters. The pathlines in Figure 3.9 (d) show uniformly expanding streamlines with no recirculation near the chamber entrance. However, recirculation is significant for the 1 mm hole diameter. This effect decreases as the hole diameter increases, and completely disappears when the hole diameter was 5 mm, or 2.5 times bigger than the hole spacing.

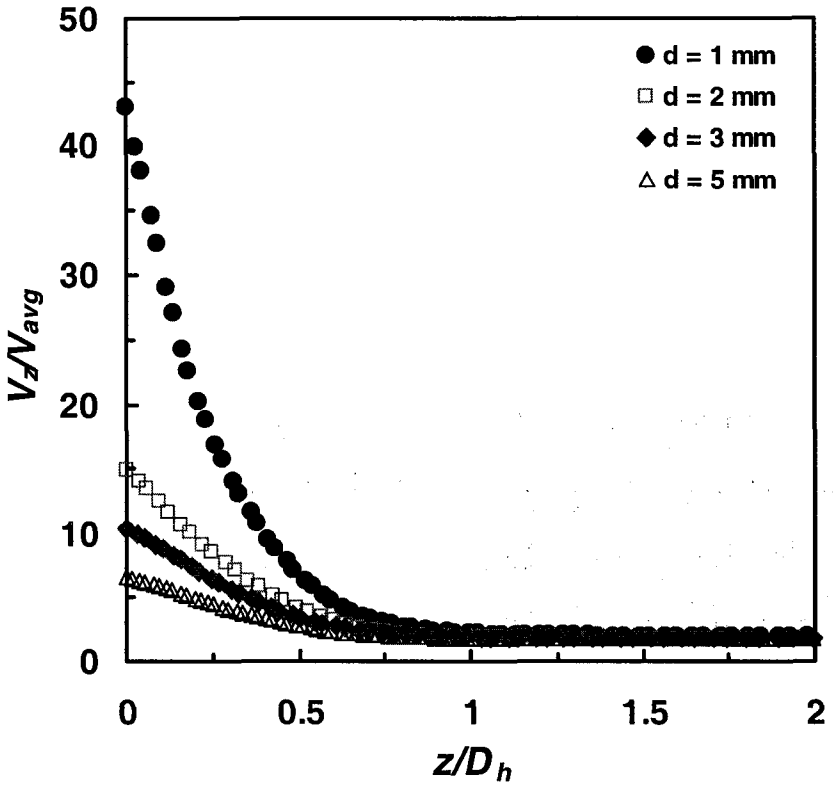

Figure 3.7 **The dimensionless axial velocity (v_z/v_{avg}) as a function of dimensionless axial position along the centerline of the chamber, for the inlet showerhead with different hole diameters. The conditions used in the calculations are 300 K and 1 torr.**

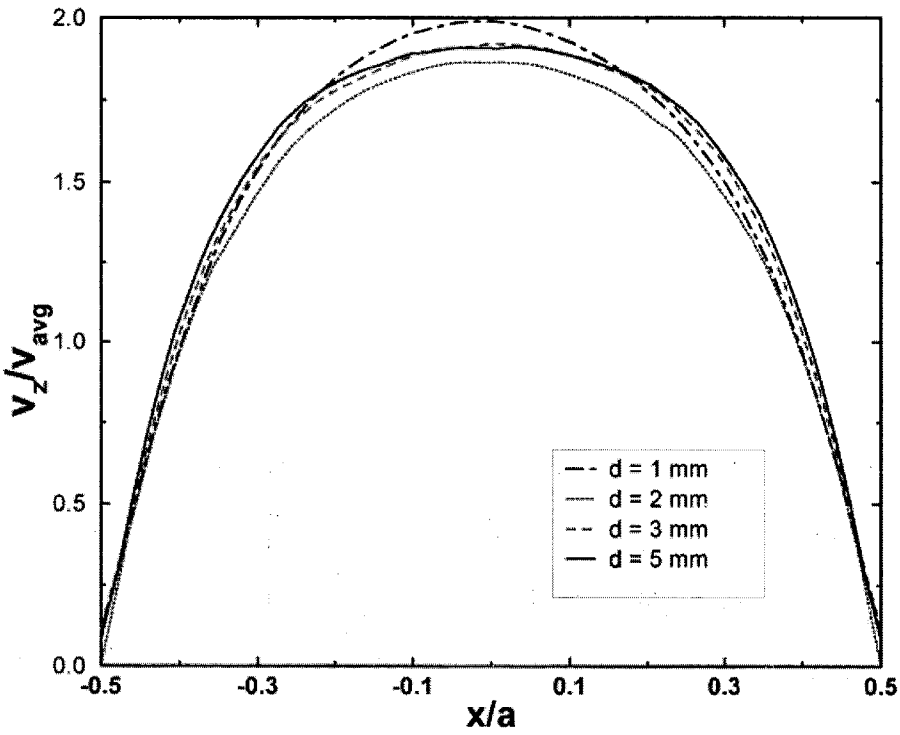

Figure 3.8 **The axial velocity profiles along the transverse horizontal axis for the showerhead with different hole diameters. The conditions used in the calculations are 300 K and 1 torr. The curves are plotted near the chamber outlet plane, at the midpoint of the chamber height.**

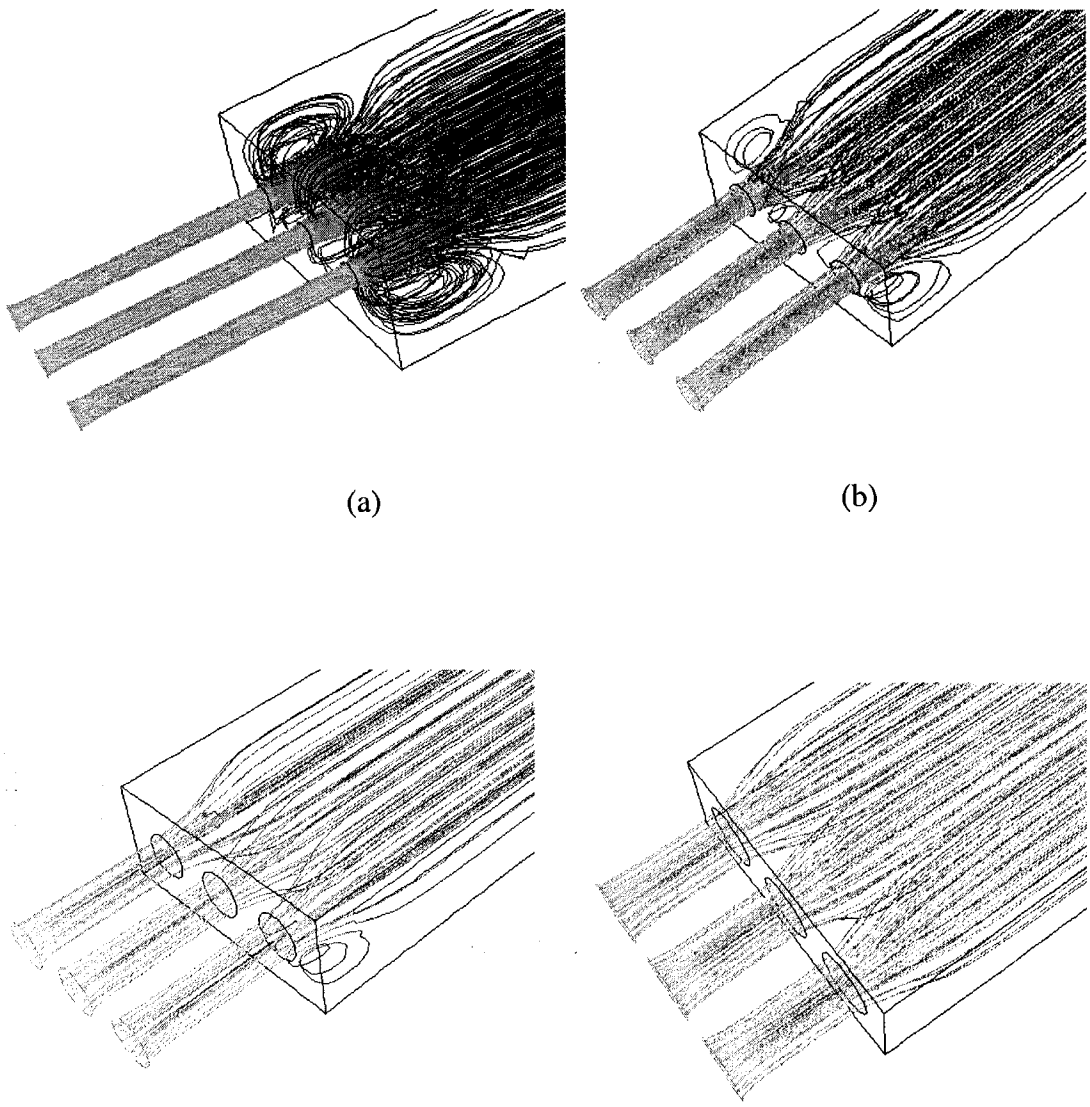

Figure 3.9 Pathline plot for different hole diameters, (a) 1 mm, (b) 2 mm, (c) 3 mm , and (d) 5 mm.

The results from this study are similar to those of the previous section. The entrance lengths did not change significantly as the hole diameter increased. But, the velocity profiles became flatter as the hole diameter increased from 1 mm to 5 mm. The bigger hole diameter is preferred since the flow is more uniform, the showerhead may be easier to manufacture, and the required pressure drops are lower.

3.3 Effect of the Gap near the Chamber Walls

In this study, the spacing between holes and chamber wall, h, was varied from 1 mm to 4 mm, while the hole spacing and the hole diameter were fixed at 2 mm. The chambers were 50 mm long. The chamber width and height were changed in accord with the space between holes and chamber wall, as listed in Table 3.3. The configuration of the chamber used in these calculations is shown in Figure 3.10. The conditions in the chamber were again set at 300 K and 1 torr. The inlet velocity was set at 15.5 m/s, which corresponds to an inlet Reynolds number of 20.

Table 3.3 Dimensions of the chamber and other parameters used in the calculations for studying the effects of space near the chamber wall. The hole diameter and hole spacing are fixed at 2 mm. The showerhead is 10 mm thick.

Parameters	*Gap near the chamber*			
	1 mm	*2 mm*	*3 mm*	*4 mm*
Chamber height (mm)	4	6	8	10
Chamber width (mm)	12	14	16	18
Chamber length (mm)	50	50	50	50
Inlet velocity (m/s)	15.5	15.5	15.5	15.5
Inlet Reynolds number	20	20	20	20
Inlet flow rate (sccm)	503	402	336	287
Chamber Reynolds number	11.9	9.5	7.9	6.8

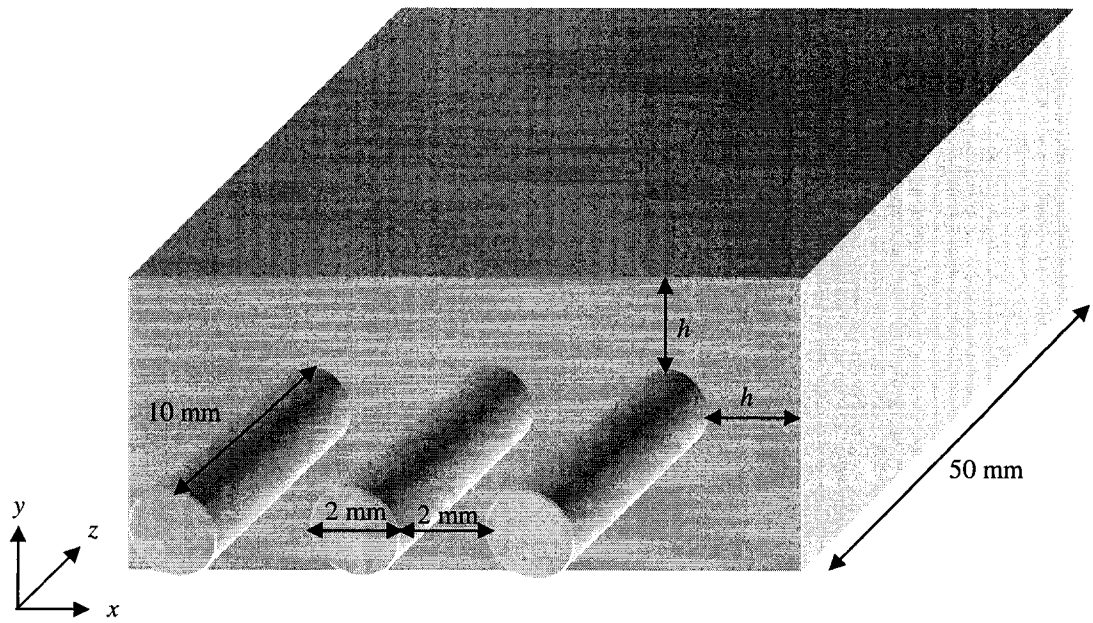

Figure 3.10 Configuration used in the calculations for studying the effects of space between chamber wall and holes, *h*.

Figure 3.11 shows the dimensionless axial velocity component as a function of the dimensionless axial position. The curves represent the velocities along the centerline of the chamber. The entrance lengths were seen to increase with increasing space between the holes and chamber walls. The extracted dimensionless entrance lengths were approximately 0.9, 0.9, 1.2, and 1.3 for 1, 2, 3, and 4 mm spacing near the walls, respectively. The axial velocity profiles along the horizontal axis are shown in Figure 3.12, where the curves represent the velocity profiles near the chamber outlet, at center of the chamber. The velocity profiles along the x direction were parabolic for all cases. The profiles were flatter when the space between the holes and chamber wall was decreased.

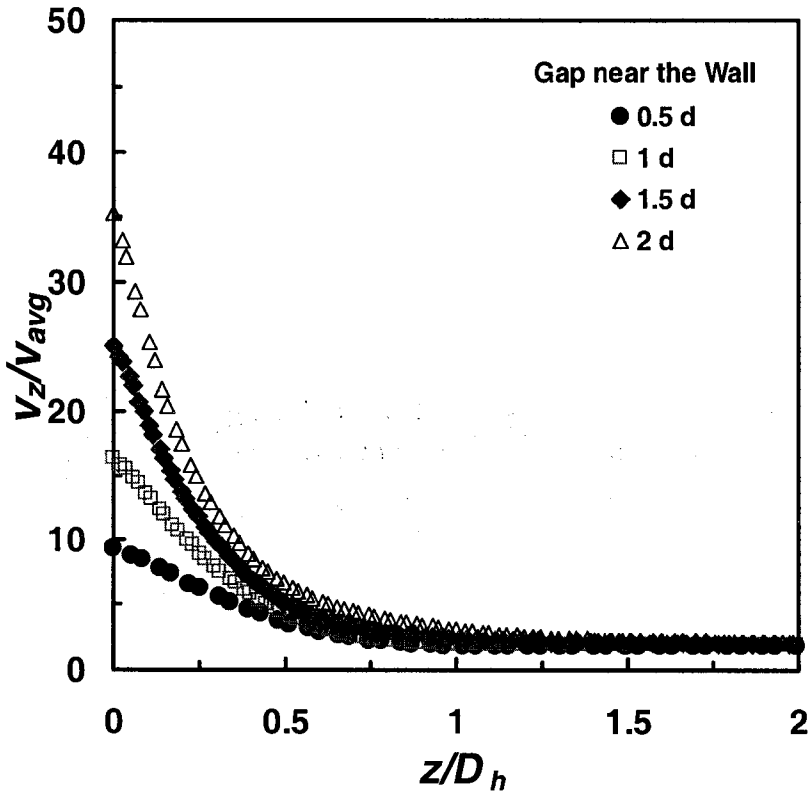

Figure 3.11 The dimensionless axial velocity (v_z/v_{avg}) along the centerline of the chamber as a function of dimensionless axial position (z/D_h) for the inlet showerhead with different spacing between holes and chamber wall. The conditions used in the calculations were at 300 K, 1 torr, and 15.5 m/s inlet velocity (N_{Re} ~ 20).

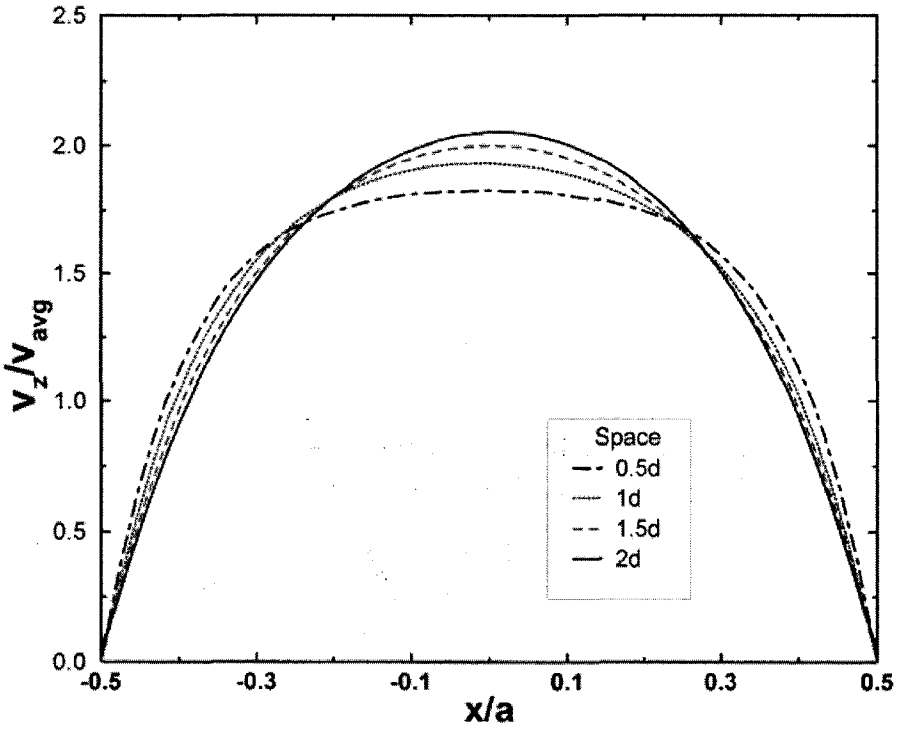

Figure 3.12 The velocity profiles along the transverse horizontal axis for the showerhead with different spacings between holes and wall. The conditions used in the calculations were 300 K, 1 torr, and 15.5 m/s inlet velocity (N_{Re} ~ 20). The curves were plotted near the chamber outlet plane, at the midpoint of the chamber height.

An increase in space between holes and chamber wall increases the entrance length. If the space between showerhead holes and chamber wall is too large, flow separation occurs, that is, the flow moves in the opposite direction near the chamber walls. The recirculation occurs at the corners of the chamber near the inlet as shown in Figure 3.13 when the space near the chamber walls is greater than the diameter of the showerhead holes (3 and 4 mm in this study). Figure 3.13 shows a pathline plot of the flow in the chamber for the case of 4 mm space between showerhead holes and chamber wall. The recirculation also occurs when the space between showerhead holes and chamber wall becomes greater than the hole spacing, as was discussed in the previous section. There the recirculation occurred at the corners of the chamber entrance for the case of 1 mm hole spacing, which has a hole spacing (1 mm) smaller than the space between showerhead holes and chamber walls (2 mm).

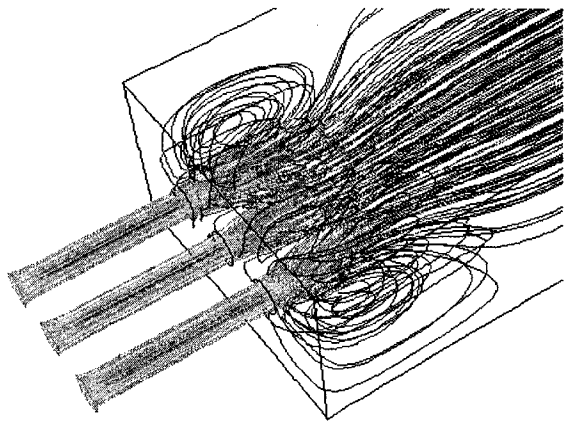

Figure 3.13 Pathlines showing the recirculation at the corners near the chamber inlet for the case of 4 mm spacing near the walls.

The dimensionless entrance lengths based on the hydraulic diameter of the chamber for the showerhead used in the above simulations are in the range 0.9 to 1.5, and do not change significantly as the hole spacing, hole diameter, and spacing near the chamber wall are increased. It is known that the entrance length of flow in the channel depends on the Reynolds number. The correlation of the hydrodynamic entrance length in unidirectional laminar flow for two infinite parallel plates proposed by Atkinson et al. [65] is

$$X_e = 0.625 + 0.022 N_{\mathrm{Re}}, \tag{3.2}$$

where X_e is dimensionless entrance length based on the gap between the parallel plates, N_{Re} is the Reynolds number between parallel plates based on the hydraulic diameter. The dimensionless entrance lengths based on the hydraulic diameter of the chamber (L_e/D_h) extracted from this study are plotted as a function of the Reynolds number in Figure 3.14. The filled circles represent the data from the hole spacing study (section 3.1), the filled squares represent the data from the hole diameter study (section 3.2), and the filled diamonds represent the data from the space between showerhead holes and chamber wall (section 3.3). These data are not well correlated since the inlet configurations are changed in each case. This apparent lack of correlation arises because the entrance lengths at low Reynolds numbers depend strongly on the axial diffusion of the upstream vorticity from the chamber entrance [65], which in turn depends on the inlet configuration. Additional simulations are carried out using a larger chamber with the inlet showerhead consisting of 21 holes of 2 mm hole diameter, 2 mm hole spacing, and 4 mm space between holes and chamber wall. The chamber is 32.4 mm wide, 18 mm high, and 100 mm long. The calculations are

carried out for different inlet velocities from 0.5 to 20 m/s, which correspond to chamber Reynolds numbers that range from 0.9 to 34. The dimensionless entrance lengths extracted from these simulations are plotted in Figure 3.13 (filled triangle). The correlations obtained from the linear least squares fit are shown below:

$$L_e / D_h = 0.0793 + 0.0172 N_{\mathrm{Re}}, \tag{3.3}$$

where L_e is the entrance length, D_h is the hydraulic diameter, and N_{Re} is the Reynolds number based on the hydraulic diameter. The slope of linear fit obtained in this study (0.0172) is reasonably close to Atkinson's equation for laminar flow in parallel plates, but the intercept is about one eighth of Atkinson's. However, Atkinson's equation is a two-dimensional expression for unidirectional flow, and can only be rigorously applied to a very large width to height ratio in a rectangular channel. Since the chamber used in this study has width to height ratio of 1.8, the assumption of two dimensional flow is not valid. The other reason for the difference in the correlations is that Atkinson et al. used a flat velocity profile as the initial condition in their calculations, whereas the inlet velocity profiles in these studies are the small parabolic profiles emerging from the showerhead holes. Since the coefficients of the entrance length correlation obtained from the least squares fit are lower than the value of Atkinson's equation, it is safe to calculate the entrance length for the actual reactor using Atkinson's correlation.

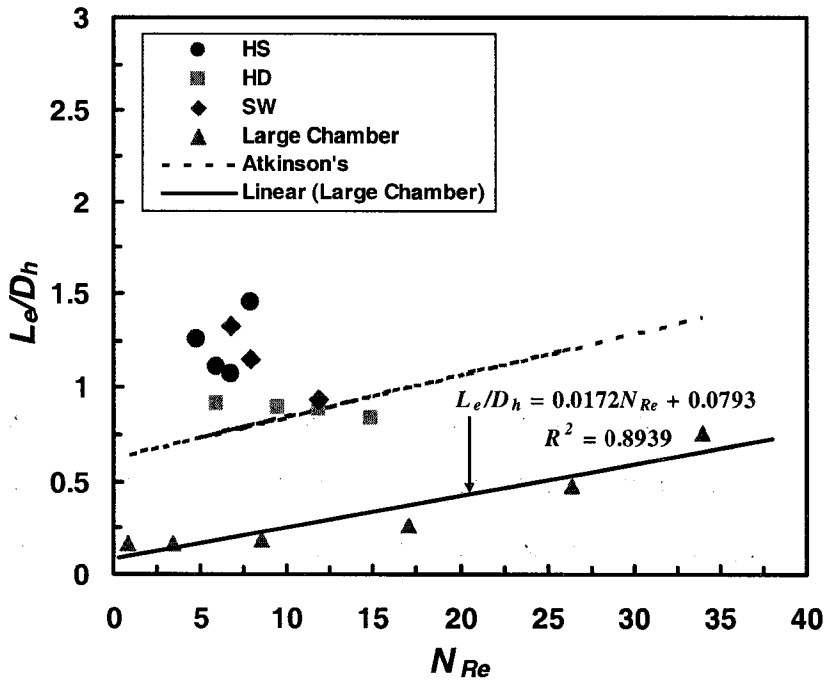

Figure 3.14 **Dimensionless entrance lengths (L_e/D_h) as a function of Reynolds number (N_{Re}). The circles represents data from hole spacing study (HS), the diamonds represent data from hole diameter study (HD), and the squares represent data from the spacing between holes and wall study (SW), the triangles represent data from large chamber simulations.**

3.4 Scale-Up

Since the studies have been performed in small chambers, with corresponding small numbers of inlet showerhead holes, there is an important question regarding the validity of the results. To ensure that the results are applicable to larger chambers, several calculations were done using a chamber larger than these chambers used in these studies. The simulations are carried out in two chambers with the same width to height ratio (~ 1.8), and showerhead configuration. The cross-sectional area of the large chamber is 3.24 times the cross-sectional area of the small chamber. The diameter of the holes is 2 mm, the hole spacing is 2 mm and the space between holes and chamber wall is 4 mm. While the number of holes in the small chamber is 3, 21 holes are used in the larger chamber. The velocity profiles at the plane near the chamber exit from these two cases are plotted in Figure 3.15. In this figure, the axial velocity is normalized by average velocity, v_{avg}, and the dimensionless transverse horizontal position is defined in terms of the chamber width, a. The profiles from these two chambers are exactly the same. This indicates that the increase in the size of the chamber does not change the velocity profile and the profiles determined in the above studies are applicable to use in the situations where the size of the chamber is larger than the chamber in these studies.

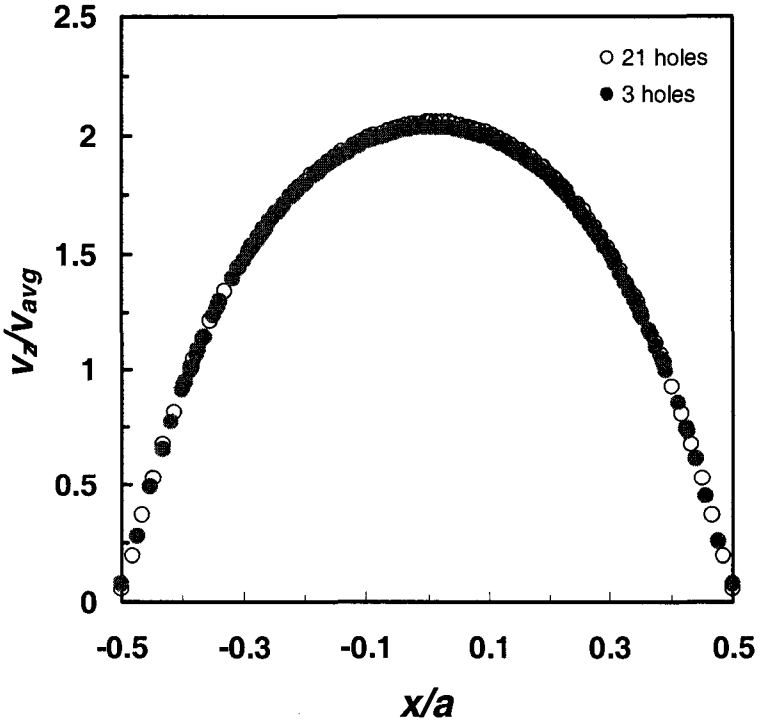

Figure 3.15 Comparison of the velocity profiles generated from flow in a large chamber and small chamber with the same inlet configuration. These profiles show the normalized velocity as a function of normalized transverse horizontal position near the exit of the chamber.

3.5 Analytical Expression for the Velocity Distribution

The results from these studies have shown that the velocity profiles obtained from the different showerhead configurations are mainly parabolic, once the flow becomes fully developed. The next step in the overall reactor modeling is to examine the flow and heat transfer in an "actual"' reactor, and it's not feasible to run calculations with inlets containing hundreds or thousands of holes. It is highly desirable to be able to neglect the entrance region in full reactor modeling studies. To

accomplish this it is necessary to be able to specify the fully developed velocity profile as the inlet boundary condition. The objective of this section is to derive an analytical expression for this fully developed flow, obtained from solving the governing equations and associated boundary conditions.

To find a velocity distribution in a rectangular cross-section channel whose sides are at $y = \pm a$, and $x = \pm b$, where b is much greater than a, the axes are placed at the middle of the channel. The effect of gravity is neglected since the channel is in a horizontal position. At a certain point in the axial direction or z-direction where the flow is considered to be a fully developed flow, the axial velocity does not depend on the axial position. For a unidirectional flow in a rectangular channel, x and y velocity component are zero. Hence, the continuity equation, the y-component and the z- component of equation of motion [66] reduce to

$$\frac{\partial u}{\partial z} = 0, \frac{\partial p}{\partial y} = 0, \frac{\partial p}{\partial z} = 0, \tag{3.4}$$

where u is the velocity in z-direction, and p is dynamic pressure in the channel. The x-component of the equation of motion for the steady state case is simplified to

$$\frac{\partial^2 u}{\partial x^2} + \frac{\partial^2 u}{\partial y^2} = -\frac{G}{\mu}, \tag{3.5}$$

where G is a positive constant pressure gradient, and μ is viscosity.

The general solution is obtained by assuming $u(x,y)$ may be represented as the sum of a homogeneous (u_h) and a particular (u_p) solution. The homogeneous equation is

$$\frac{\partial^2 u_h}{\partial x^2} + \frac{\partial^2 u_h}{\partial y^2} = 0. \tag{3.6}$$

Applying the separation of variables method yields the solution of equation (3.6) as

$$u_h(x, y) = X(x)Y(y), \tag{3.7}$$

which are the product of two functions, each depending only on one of the variable x and y. Differentiating equation (3.7) and substituting into equation (3.6) gives

$$\frac{X''}{X} = -\frac{Y''}{Y} = -\lambda^2, \tag{3.8}$$

which can be separated into two ordinary linear differential equations:

$$X'' + \lambda^2 X = 0, \tag{3.9}$$

and

$$Y'' - \lambda^2 Y = 0. \tag{3.10}$$

By solving equation (3.9), the general solution of equation (3.9) is

$$X = A\cos(\lambda x) + B\sin(\lambda x). \tag{3.11}$$

The velocity reaches a maximum at the center of the channel. This gives $\frac{\partial u_h}{\partial x} = 0$ at $x = 0$ or $X'(0) = 0$. After differentiating equation (3.11), the first term becomes zero when x is zero, while the second term will not be zero. In order to satisfy this boundary condition, B must be zero. The solution of X is in the form

$$X = A\cos(\lambda x). \tag{3.12}$$

Solving the equation (3.10) yields the general solution as

$$Y = C\cosh(\lambda y) + D\sinh(\lambda y). \tag{3.13}$$

Again, the velocity is maximum at the center, which give $Y'(0) = 0$. Applying this boundary condition into equation (3.13) gives $D = 0$, and equation (3.13) becomes

$$Y = C\cosh(\lambda y). \tag{3.14}$$

Substituting equation (3.12) and (3.14) into equation (3.7) yields

$$u(x, y) = A\cos(\lambda x)\cosh(\lambda y). \tag{3.15}$$

Due to the adhesion of fluid to the wall, the velocity at the wall is zero, or $u(a,y) = 0$. To satisfy this condition cos (λa) must be zero, that is,

$$\lambda a = \left(n + \frac{1}{2}\right)\pi, \qquad n = 0,1,2,\cdots \tag{3.16}$$

or

$$\lambda_n = (2n+1)\frac{\pi}{2a}. \tag{3.17}$$

Hence, the general solution obtained from the homogeneous equation is

$$u(x, y) = \sum_{n=0}^{\infty} A_n \cos(\lambda_n x)\cosh(\lambda_n y). \tag{3.18}$$

Since the function on the right hand side of equation (3.4) is independent of y, the particular solution is obtained by solving the following ordinary differential equation

$$\frac{d^2u}{dx^2} = -\frac{G}{\mu}. \tag{3.19}$$

Integrating equation (3.19) yields

$$\frac{du}{dx} = -\frac{G}{\mu}x + C_1, \tag{3.20}$$

where C_1 is integrating constant. Since the velocity is symmetric at the center, or $\left.\frac{du}{dx}\right|_{x=0} = 0$. Applying this boundary condition to equation (3.20), gives C_1 =0 and

$$\frac{du}{dx} = -\frac{G}{\mu}x. \tag{3.21}$$

Again, integrating equation (3.21) yields

$$u = -\frac{G}{2\mu}x^2 + C_2, \tag{3.22}$$

where C_2 is integrating constant. Applying boundary condition, $u(a, y) = 0$, gives $C_2 = \frac{G}{2\mu}a^2$. Therefore,

$$u(x, y) = \frac{G}{2\mu}(a^2 - x^2) + \sum_{n=0}^{\infty} A_n \cos(\lambda_n x)\cosh(\lambda_n y). \tag{3.23}$$

Since the velocity at the top wall is also zero, $u(x, b)$ is zero. Applying this boundary condition into equation (3.23) gives

$$\sum_{n=0}^{\infty} A_n \cos(\lambda_n x)\cosh(\lambda_n y) = -\frac{G}{2\mu}(a^2 - x^2). \tag{3.24}$$

Since $-\frac{G}{2\mu}(a^2 - x^2)$ is an even function, A_n can be obtained by solving the half cosine series as

$$A_n \cosh(\lambda_n b) = -\frac{G}{\mu a}\int_0^a (a^2 - x^2)\cos(\lambda_n x)dx. \tag{3.25}$$

Integrating equation (3.25) yields

$$A_n = -\frac{2G\sin(\lambda_n a)}{\mu a \lambda_n^3 \cosh(\lambda_n b)}. \tag{3.26}$$

The velocity distribution in a channel of rectangular cross-section obtained from the above equation can be expressed as a Fourier series as

$$u(x, y) = \frac{G}{2\mu}(a^2 - x^2) + \sum_{n=0}^{\infty} A_n \cos(\lambda_n x)\cosh(\lambda_n y), \tag{3.23}$$

where

$$\lambda_n = \frac{(2n+1)\pi}{2a},$$

$$A_n = -\frac{2G\sin(\lambda_n a)}{\mu a \lambda_n^3 \cosh(\lambda_n b)},$$

where a is the half width of the channel, and b is the half height of the channel. The volumetric flow rate Q passing through the channel can be calculated by integrating the velocity distribution over the cross-sectional area,

$$Q = 4\int_0^b \int_0^a u(x,y)dxdy. \tag{3.27}$$

From the volumetric flow, we can find the pressure gradient G in term of Q as

$$G = \frac{\mu Q}{4}\left[\frac{a^3 b}{3} - \frac{2}{a}\sum_{n=0}^{\infty}\frac{\sin^2(\lambda_n a)\tanh(\lambda_n b)}{\lambda_n^5}\right]^{-1}. \tag{3.28}$$

The velocity profiles calculated from the expression in Eq. (3.23), and the velocity profiles at the plane near the chamber exit, from the simulations of the scaled-up chamber are shown together in Figure 3.16. Figure 3.16(a) shows the plot of the velocity profiles along the transverse horizontal axis. Figure 3.16(b) shows the velocity profiles along the vertical axis. The chamber used in the calculation is 100 mm long, 18 mm high, and 32.4 mm wide. The shower inlet in the CFD simulation consisted of 21 inlet holes with 2 mm diameter, 2 mm hole spacing, and 4 mm spacing near the walls. The velocity profiles along both directions are in very good agreement with the analytical velocity profiles. As mentioned at the beginning of this section, the next step of the overall reactor modeling is to examine flow and heat transfer in an "actual"' reactor. The analytical expression obtained in this section will be used as the inlet velocity profiles in the calculations for future studies.

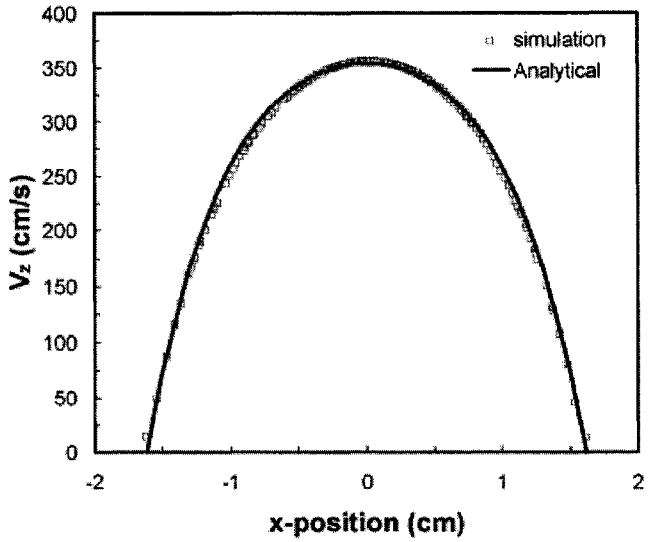

(a)

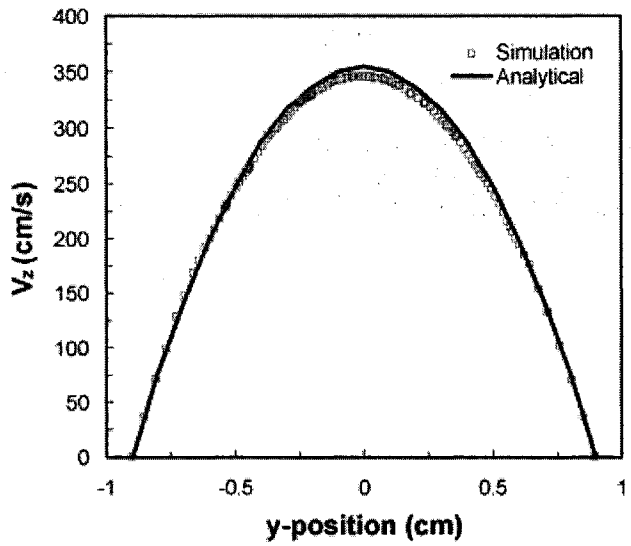

(b)

Figure 3.16 Comparison of velocity profiles near the chamber exit obtained from the simulation with the velocity profiles from analytical expression (equation 3.23). The top figure, (a), shows velocity profiles along the transverse horizontal axis, and the bottom figure, (b) shows the velocity profiles along vertical axis.

3.6 Summary

The following conclusions can be drawn from the above results.

- The results from these studies indicate that there is little effect on the entrance length and the shape of the velocity profiles due to the shower hole spacing, shower hole diameter, and spacing near the chamber walls.

- The entrance lengths obtained from the simulations were fitted by the least square method with R^2 value of 0.89. The slope of the correlation obtained from this study is reasonably close to Atkinson's equation, but the intercept is about one eighth of Atkinson's value.

- The velocity profiles from the analytical expression showed very good agreement with the simulation profiles. The analytical expression will be used as the inlet velocity profile for the calculations in the future, which will examine the flow and heat transfer in an "actual" reactor to identify the most important reactor geometric parameters, such as the location of the substrate, space between substrate and hot filaments, and space between the reactor top wall and hot filaments.

Chapter 4

DESIGN AND OPTIMIZATION OF THE HOT FILAMNET ARRAY

In this chapter an investigation of the effects of the filament arrangement and filament size is presented. The primary goal of these hot filament chemical vapor deposition reactor (HFCVD) modeling studies is to design a one-dimensional flow HFCVD reactor for the deposition of fluorocarbon films using an approach based on rigorous application of computational fluid dynamics (CFD) to investigate different reactor geometries and operating conditions. It is known from experience with many CVD systems that reactor geometry strongly affects flow, mass, and energy transport behavior, which in turn directly affects the properties of the deposited films [64]. The following numerical experiments are an important part of the studies in the design stage. In the last chapter, the effect of different showerhead configurations has been investigated through varying the showerhead hole-diameter, showerhead hole spacing, and the space between the showerhead and the reactor walls. The results from the last chapter showed that the shower hole spacing, the hole-diameter, and the space near the chamber wall had little effect on entrance length and the shape of the velocity profiles. The velocity profiles obtained from the simulations were parabolic, and were in good agreement with the profiles obtained from the analytical expression, derived from the equation of motion, as follows:

$$u(x,y)=\frac{G}{2\mu}(a^2-x^2)+\sum_{n=0}^{\infty}A_n\cos(\lambda_n x)\cosh(\lambda_n y), \qquad (4.1)$$

where

$$\lambda_n = \frac{(2n+1)\pi}{2a},$$

$$A_n = -\frac{2G\sin(\lambda_n a)}{\mu a \lambda_n^3 \cosh(\lambda_n b)},$$

a is half width of the channel, b is half height of the channel, $u(x,y)$ is the velocity as a function of the horizontal position, x, and vertical position, y, in the reactor chamber, G is the pressure gradient, and μ is the viscosity of the gas. To simplify the model, the entrance region will not be considering. Instead, the domain begins at the point where the flow is fully developed, and is well described by the equation (4.1). Figure 4.1 (a) shows the configuration of the reactor and the direction of the system coordinate used in the calculation.

In this chapter, two possible filament arrangements will be examined to determine the appropriate filament arrangement that will lead to the uniform temperature profile above the substrate that is essential for producing a uniform fluorocarbon films. In the first arrangement, the filaments are arranged perpendicular to the flow at a uniform height above the substrate, as shown in Figure 4.1, and are called the horizontal filament arrangement. In the second configuration, the filaments were stacked vertically near the reactor inlet, again orient perpendicular to the flow, referred to as the vertical filament arrangement. The effects of the filament diameter and the spacing between filaments on the temperature distribution in the gas above the substrate region will be investigated. Only the momentum and energy conservation equations will be used in the calculations. Since the pyrolytic conversion of hexafluopropylene oxide (HFPO) is so small, the heat of reaction and the species composition has negligible effects on the energy and momentum equations. All the calculations

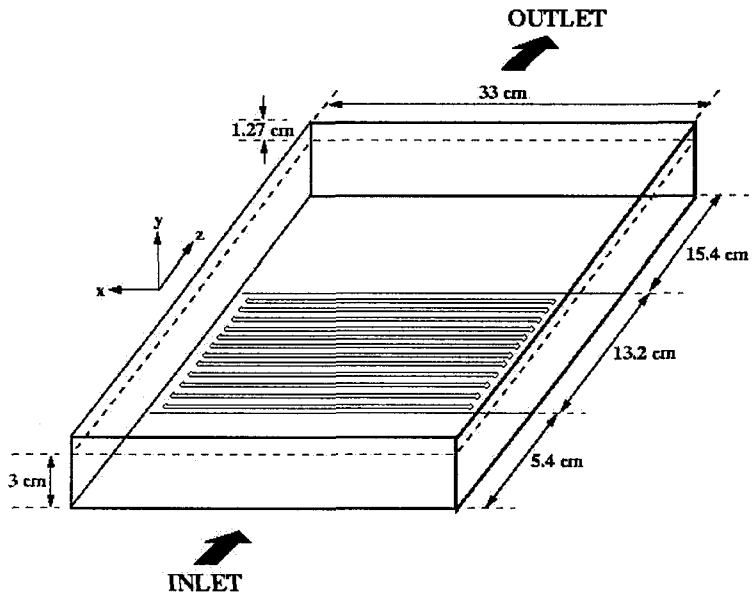

(a)

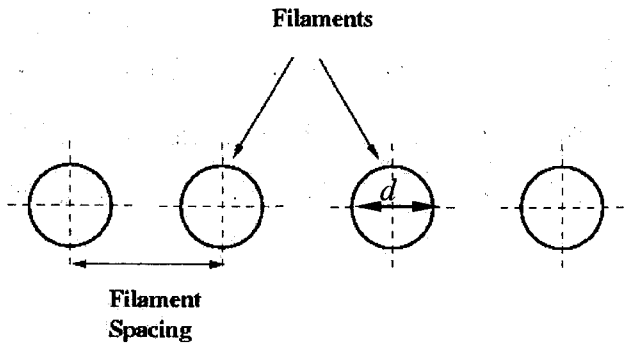

(b)

Figure 4.1 **The reactor configuration used in the calculations for the horizontal filament arrangement. (a) The dimension of the reactor and the position of the filament array in the reactor. (b) the cross-sectional of the filament array showing that the spacing was measured from the center of one filament to the center of the next filament.**

were done at 1 torr pressure, with a HFPO inlet flow rate of 790 sccm. These parameters are equivalent to a Reynolds number of 20. The boundary conditions used in this study are listed on the Table 4.1. As discussed, in the following study, equation (4.1) is applied as the inlet velocity boundary condition gas flow. The user defined function of the inlet velocity profile is shown in Appendix C.1. The entrance length of the reactor is known from the previous chapter. The assumption of fully developed flows will be applied in this study. Thus, the domain of the calculations will exclude the showerhead and reactor entrance sections.

Table 4.1 Boundary conditions used in the calculations

Boundary	Flow Type	Energy Type
Gas inlet	velocity profiles Eq.(4.1)	constant temperature (300K)
Gas outlet	zero velocity gradient	zero temperature gradient
Substrate	no-slip wall	constant temperature (300 K)
Filaments	no-slip wall	constant temperature (700 K)
Reactor top wall	no slip wall	natural convection
Reactor sidewall	no-slip wall	natural convection
Reactor bottom wall	no-slip wall	constant temperature (300 K)

4.1 Horizontal Filament Arrangement

In this section, the filament array was placed 1 cm above the substrate and about 5.4 cm from the inlet for 2*d*, 3*d*, and 6*d* cases, about 5.5 cm for 5*d*, and 5.6 cm for the 4*d* case. The reactor chamber used in the calculations was 33 cm wide, 34 cm long, and 3 cm high. The filaments are 32 cm long with 2 mm diameter (*d*) for this study. The filament spacing is measured as the center-to-center distances between adjacent filaments, and is varied from 2*d*, or 4 mm to 6*d*, or 12 mm, in a 1*d*, or 2 mm increment. The configuration of the reactor chamber and filaments arrangement is

shown in Figure 4.1 (a). The total width of filament array varies from 12.8 to 13.3 cm. The dimensions of the reactor and the parameters used in the calculations are summarized in Table 4.2.

Table 4.2 Dimensions of the reactor and parameters used in the calculations for studying the effects of the filament arrangement

Parameters	Value
Filament spacing (mm)	4, 6, 8, 10, 12
Filament diameter (mm)	2
Filament length (cm)	32
Reactor chamber height (cm)	3
Reactor chamber length (cm)	34
Reactor chamber width (cm)	33
Substrate area (cm × cm)	33 × 14

4.1.1 Effects of the Filament Spacing

Figure 4.2 shows the temperature distributions of the gas in the area under the filament array for different filament spacings; $2d$ and $3d$. The temperature is shown along the axial direction of the reactor, at the center, and at different vertical distances below the filament array; 2, 3, 4, 5, 7, and 9 mm below the center of the filament array. As shown in Figure 4.2, the gas temperature at 2 mm below the filaments fluctuates more as the space between the filaments is increased. The spikes in fluctuations correspond directly to the position of the filaments. The fluctuations in temperature decrease noticeably at 3 to 4 mm below the filaments. The temperature profile experienced fluctuation 5 and 7 mm below the filaments in all cases. The fluctuations at these locations appear to be random and do not show any predictable patterns or dependence on the filament spacing. However, in each case the fluctuation pattern at the 5 mm away from filaments was similar to the fluctuation pattern at 7

mm. It appears that the patterns travel from left to right, with the flow and increased away from the filaments. This implies that these fluctuations may be the result of the conduction of the energy toward the substrate, and convection of energy from the entrance of the reactor to the exit. The temperature distributions are more uniform closer to the substrate since the substrate temperature is fixed at 300 K. In terms of the temperature magnitude, the average temperature in the gas phase increases as the space between filaments decreases. The average temperature and standard deviation calculated from the temperature values between 8 cm and 18 cm from the inlet, at 2 mm below the filaments, are plotted against the filament spacing and shown in Figure 4.3. The average temperature decreased linearly with the filament spacing, and the standard deviation, or the temperature fluctuation, increased linearly with the filament spacing. Since the temperature fluctuation increased with the filament spacing, the optimum filament spacing for the horizontal filament arrangement should be as small as possible. The filament diameter was 2 mm in this study, so the optimum filament spacing would be 4 mm or 2 times of the filament diameter.

Figure 4.4 shows the temperature distributions along the vertical direction at different axial position from the inlet. Note that all temperatures correspond to horizontal positions midway between filament pairs. The temperature distributions below the filaments array are fully developed at 6.8, 6.9, 9.2, and 10 cm from the inlet for $2d$, $3d$, $4d$, and $5d$ cases, respectively. The maximum temperature between the filaments also increased with the decreased filament spacing. Since the profiles became fully developed 1.4 to 4.5 cm from the filament array, the substrate should be placed no closer than 5 cm to the start of the filament array to have a uniform temperature profile over the deposition area.

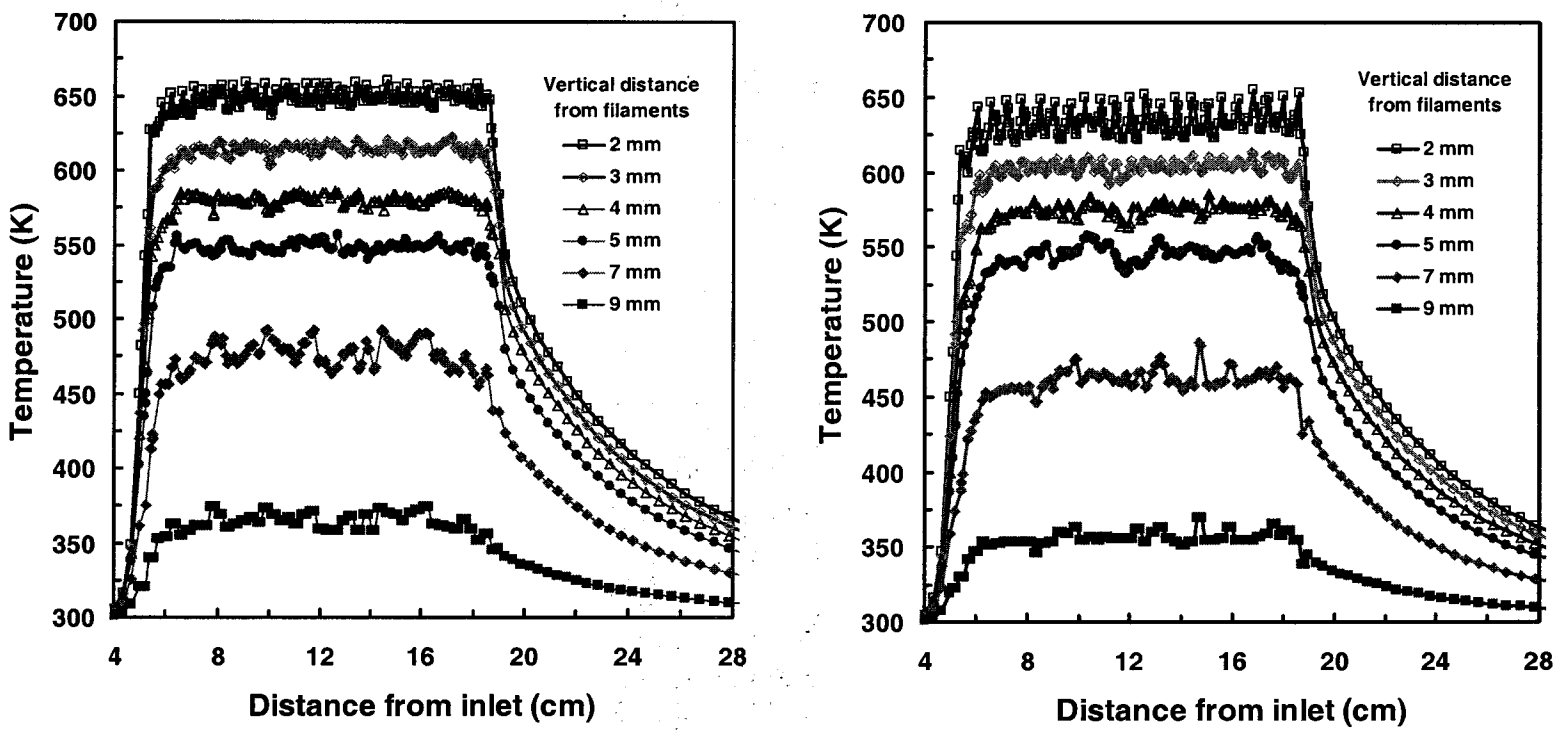

Figure 4.2 **The temperature profiles along the axial direction at different vertical distance measured from the filaments towards the substrate. (a) 2*d* filament spacing. (b) 3*d* filament spacing.**

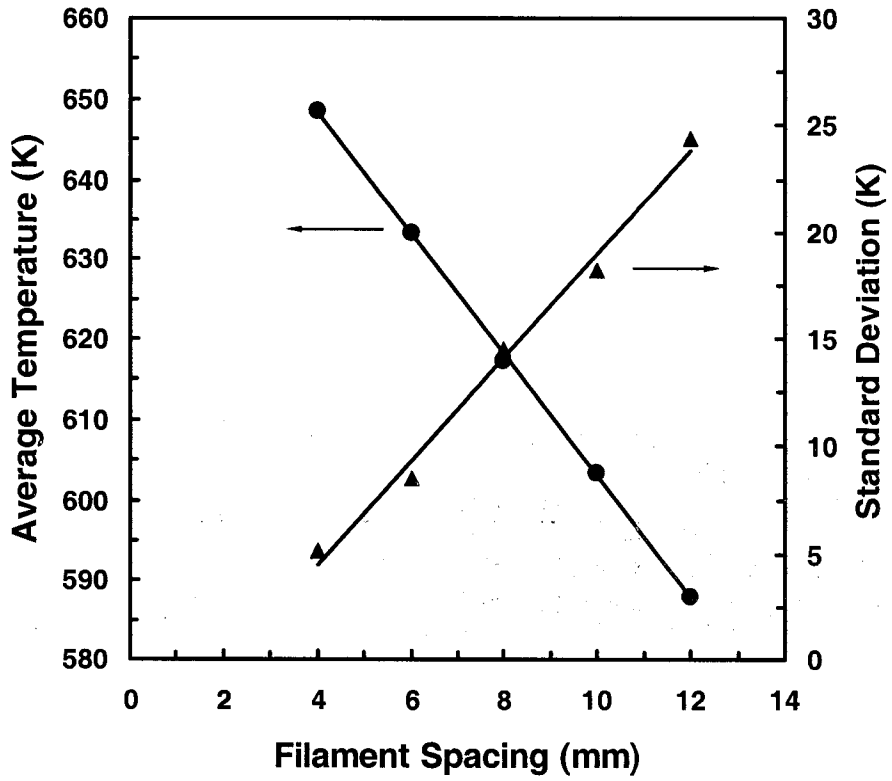

Figure 4.3 **The plot of the average temperature in gas phase at 2 mm away from the filament array versus the space between filaments with the filament diameter of 2 mm.**

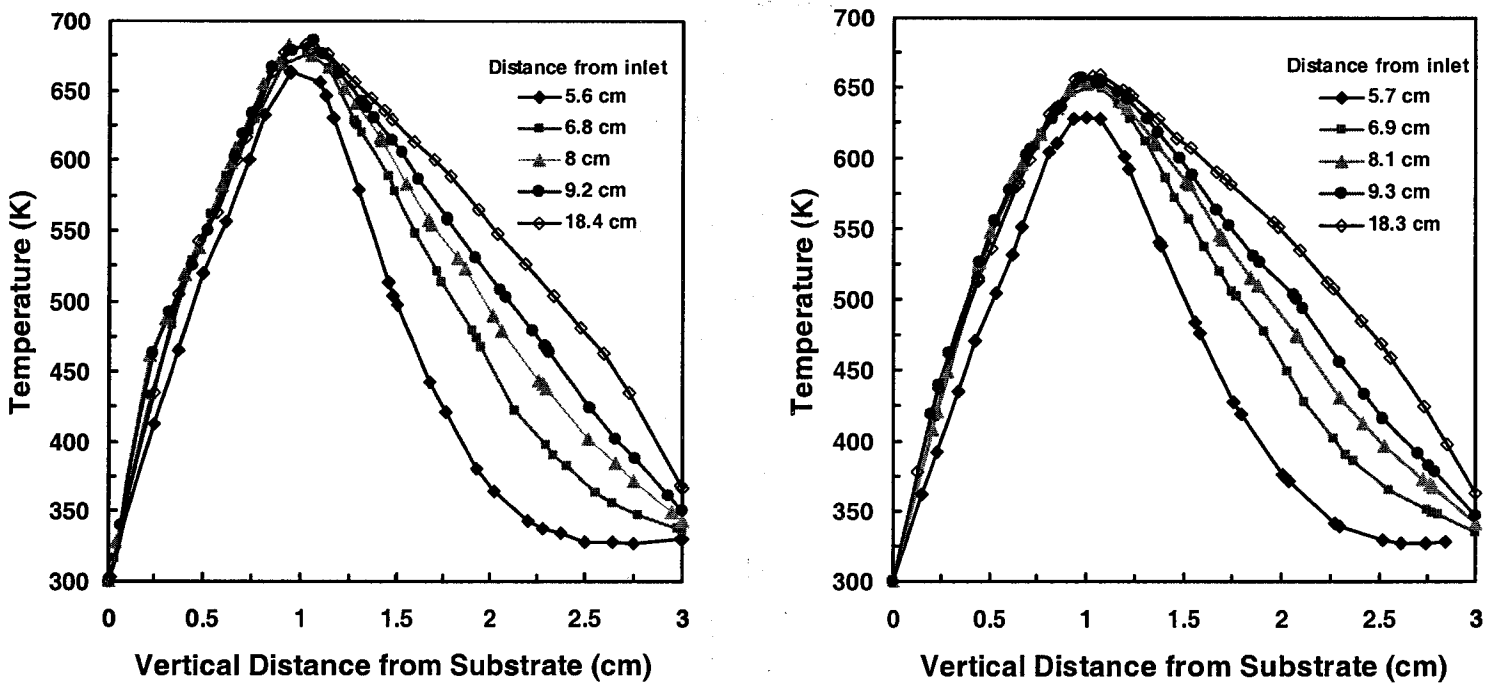

Figure 4.4 **The temperature profiles in a vertical direction at different axial distance from the reactor inlet with different filament spacing, (a) 2*d* filament spacing (b) 3*d* filament spacing.**

4.1.2 Effects of Filament Diameter

In this section, filament diameter was varied from 0.8 to 2 mm with a filament spacing of 5*d*. The distances of the filament array from the inlet were about 5.35 cm for 1.4 mm, 5.4 cm for 1.2 mm, and 5.5 cm for 1, and 2 mm filament diameters. Other reactor parameters and boundary conditions used in this study are the same as those of in section 4.1.1. Figure 4.5 shows the temperature distributions in the gas phase at different positions in the region below the filament array. The temperature profiles are similar to the profiles in the previous section. As shown in the Figure 4.5, as the filament diameter increases magnitude of the gas temperature fluctuation below the filament array were also increases. Comparing the case of 1 mm filament diameter to the 2 mm case for 2*d* filament spacing, the degree of the fluctuation is about the same, but the maximum temperature is higher for the latter case. The uniform temperature region was also larger for the case of 2 mm filament diameter with 2*d* spacing. The effects of the spacing on the temperature uniformity for small diameter filaments were not as critical as those of the big filaments. For larger diameter filaments, the spacing had to be as small as possible or less than 5 mm for all filament sizes. Figure 4.6 shows the vertical temperature profiles at different axial positions for various filament diameters. The temperature profiles below the filament become fully developed at 6.75, 6.9, 7.1, and 10 cm from the inlet for 1, 1.2, 1.4, and 2 mm filament diameter, respectively. For the horizontal filament arrangement, the optimum filament diameter was about 1 mm with the filament spacing of 5 mm. From the temperature profiles shown in this study, the temperature started fluctuating again at 7 mm below the filament array. The space between the substrate and the filament array should be less than 1 cm.

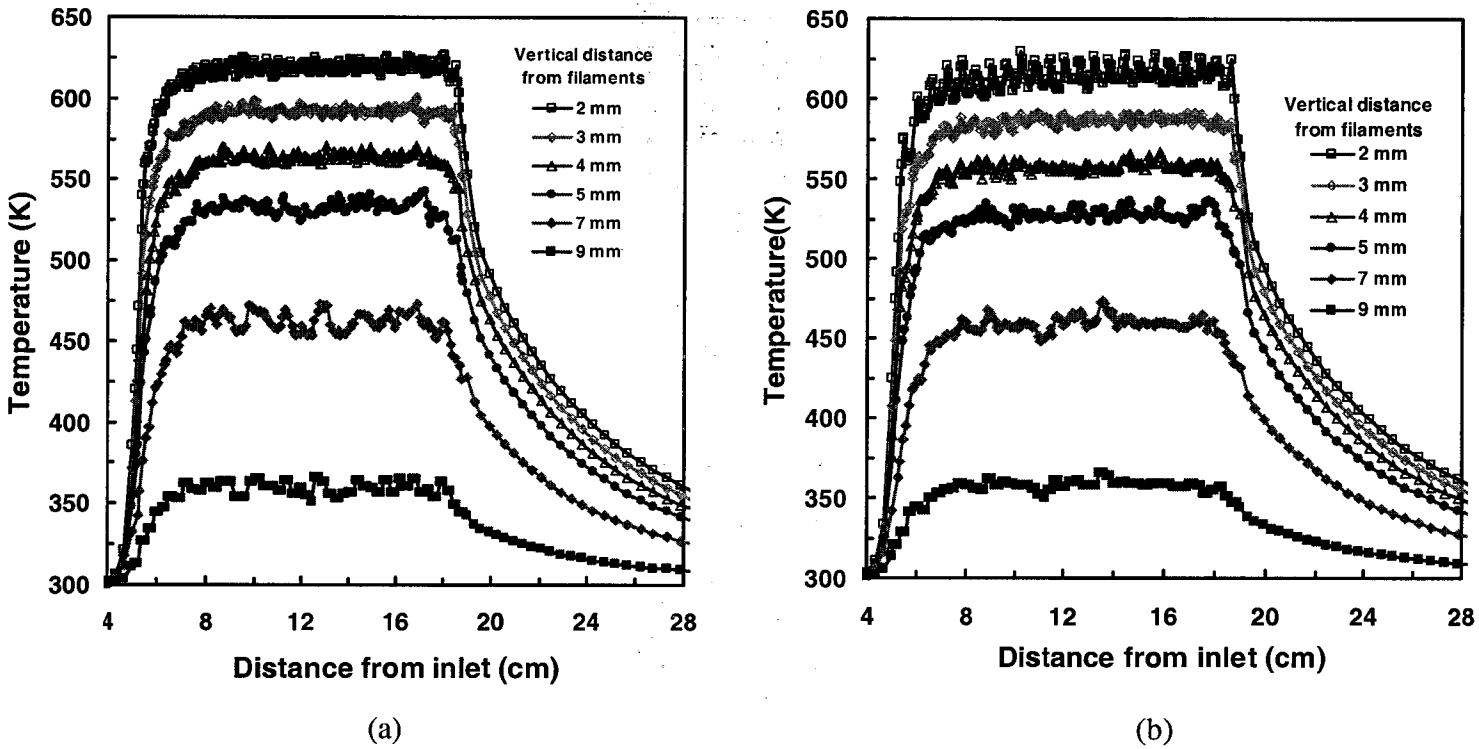

Figure 4.5 **The temperature profiles in axial direction at different position from the filament array with different filament diameter, (a) 1 mm filament diameter (b) 1.2 mm filament diameter.**

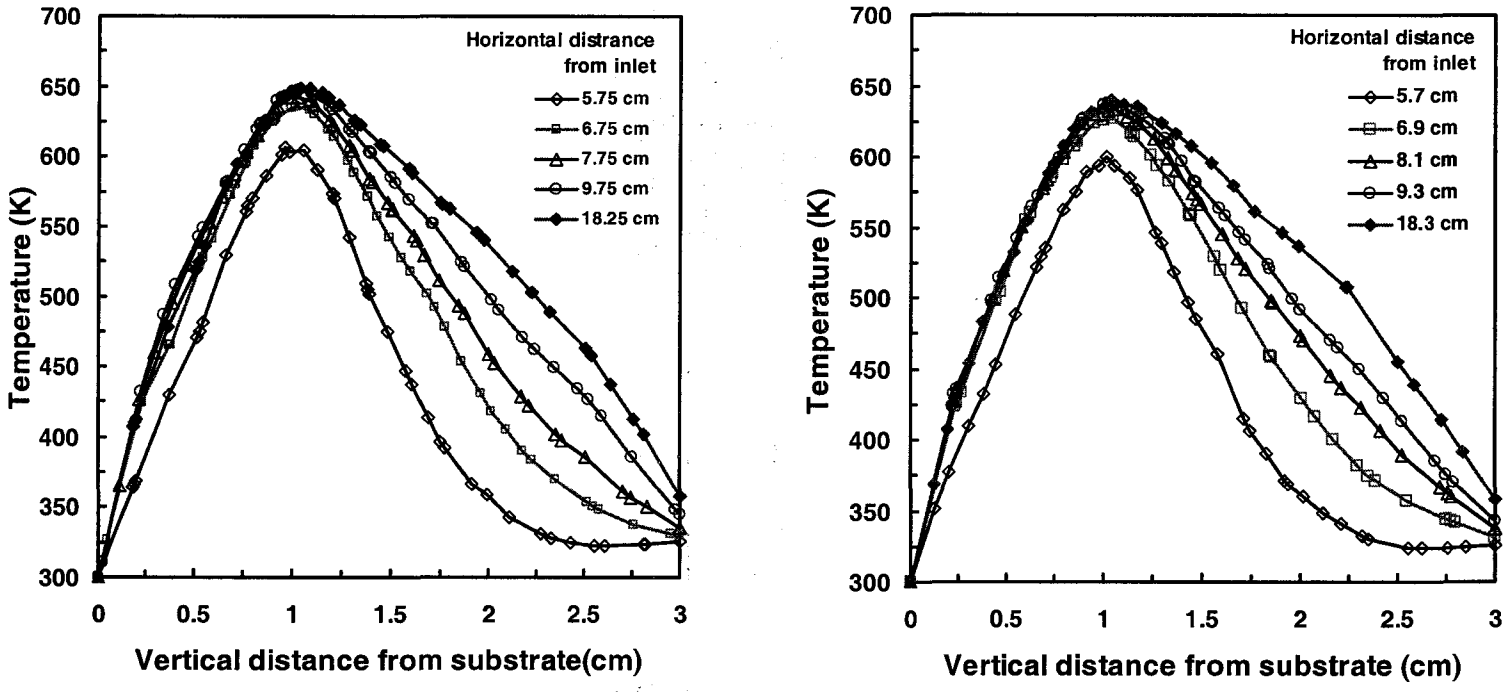

Figure 4.6 The temperature profiles in a vertical direction at different axial distance from the reactor inlet with different filament diameter, (a) 1 mm filament diameter (b) 1.2 mm filament diameter.

4.2 Vertical Filament Arrangement

The reactor used in the calculations is shown in Figure 4.7. The filaments were placed 0.5 cm from the inlet and the substrate was 28 cm long, beginning 5 cm from the inlet. The filaments were 32 cm long with 1 mm diameter and 5 mm filament spacing. The calculation was done at 1 torr pressure and a Reynolds number of 20. In this study, two sets of energy boundary conditions will be applied at the reactor walls (including top wall, side walls, and the bottom walls): (1) the adiabatic walls, and (2) convective heat flux walls. The convective heat flux losses from the wall the ambient air is calculated using the following equation:

$$q = h(T_a - T_w), \tag{4.2}$$

where q is the heat flux, h is the natural convection heat transfer coefficient, T_a is the ambient air temperature, and T_w is the wall temperature. For air at ordinary temperature and at atmospheric pressure, the natural convective heat transfer coefficient is calculated using the following equation. For a vertical surface, convective heat transfer is simplified to a dimensionless equation as [67]:

$$h = 0.29(\Delta t / L)^{0.25}. \tag{4.3}$$

For a horizontal surface h is calculated from [67]

$$h = 0.27(\Delta t / L)^{0.25}, \tag{4.4}$$

where, Δt is the temperature difference between the reactor wall and the ambient air, L is the length or height of the surface. The user defined functions of these heat transfer

coefficients are shown in Appendix C.2. The temperature of the substrate was set at 300 K. The filament temperature is 700K.

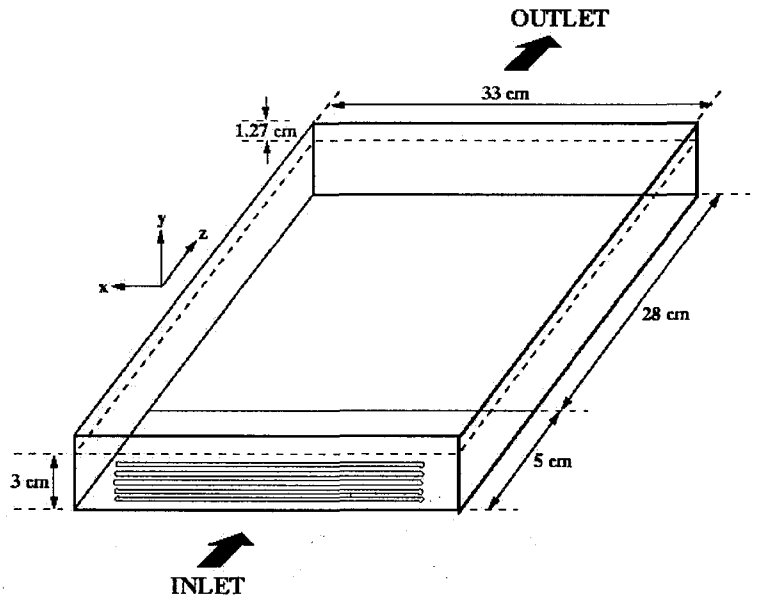

Figure 4.7 Reactor configuration used in the calculations.

The temperature profiles in the vertical direction (y-direction) were plotted at different axial positions (z-direction) as shown in the Figure 4.8. Figure 4.8(a) displays the temperature profiles when convective heat flux boundary conditions are applied at the reactor wall. The profile near the inlet was flatted at the center due to the filament array. As the gas traveled along the reactor toward the exit, the profiles became parabolic and the gas was cooled down to 300 K by the time it reached the outlet. When the reactor walls boundary conditions were changed to adiabatic, the

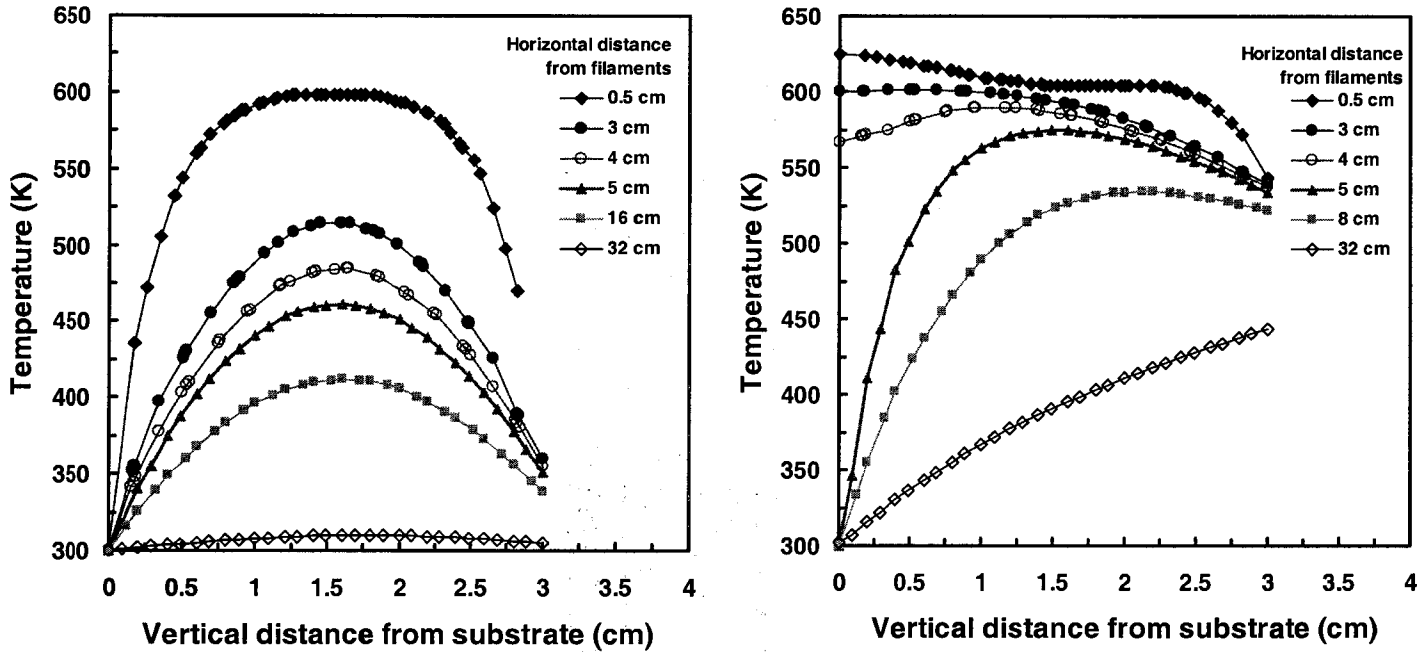

Figure 4.8 **Temperature profiles in vertical direction at different axial position. (a) The temperature profiles when the reactor wall boundary conditions were set as convective heat flux. (b) The temperature profiles when the reactor wall boundary conditions were set as adiabatic.**

profiles were more flatted near the filaments, but the temperature was also dropped, to less than 450 K at the outlet, due to the heat loss through the substrate. In both cases, the temperature over the substrate area was not uniform and it would be hard to gain uniformity in both temperature and species concentrations using this type of filament arrangement. The conversion of the HFPO (hexafluoropropylene oxide) would be very low for this arrangement as compared to the horizontal arrangement. For these reasons the vertical configuration was not investigated further. The following section will be focused solely on the horizontal filament arrangement.

4.3 Comparison of Discrete and Effective Filament Arrays

In the previous section, different filament arrangements were studied to identify the optimal combination of filament size and configuration for the reactor. The results showed that the horizontal filament arrangement produced more uniform temperature profiles over the substrate area when the filament diameter was less than 1 mm and the filament spacing was below 5*d*. However, the process of generating grids with that capture the actual shape filament geometry for diameters below 1 mm is very challenging because of the extreme differences in size between the filaments and the reactor. Moreover, the grids for the reactor with cylindrical filaments were unstructured, which tend to provide lower accuracy in calculations than structured grids. To address this technical complication and alternate filament arrays representation was examined. Instead of reproducing the actual shape of small filaments inside the reactor, the region where the filament arrays located will be replaced by a thin volume of hot gas with a temperature equals to the average temperature of the gas around the filaments, as determined in the previous sections.

The following calculations were performed to determine whether this surrogate array yields valid predictions and how much the results produced from this reactor deviated from the result of the calculations in section 4.1 and 4.2.

Figure 4.9 shows the configuration of the reactors used in this study. The reactor that contains the discrete cylindrical filaments is shown in Figure 4.9(a), and the reactor with the effective or surrogate filament array is shown in Figure 4.9(b). In both cases, the reactor dimensions are 33 cm width, 45 cm length, and 3 cm height. The reactor bottoms are divided into 3 regions: the inlet region (4 cm long), the substrate region (21 cm long), and the outlet region (20 cm long). For the reactor with cylindrical filaments, the filaments were placed at 7 mm above the substrate, measuring from filament center to the substrate surface. The first filament in the filament array was placed at 5 mm (measuring from inlet plane to the first filament center) from the inlet and the last filament was placed at 24.5 cm from the inlet. The filaments were 1 mm in diameter with 5 mm spacing between the filaments, and total number of filaments was 49. For the reactor with the effective array, the hot gas volume was 1 mm thick by 32 cm wide, by 24.1 cm long. The hot gas volume center line was placed at 7 mm above substrate and 4 mm from the inlet. The dimension of the reactor and parameters used in the calculations are summarized in Table 4.3.

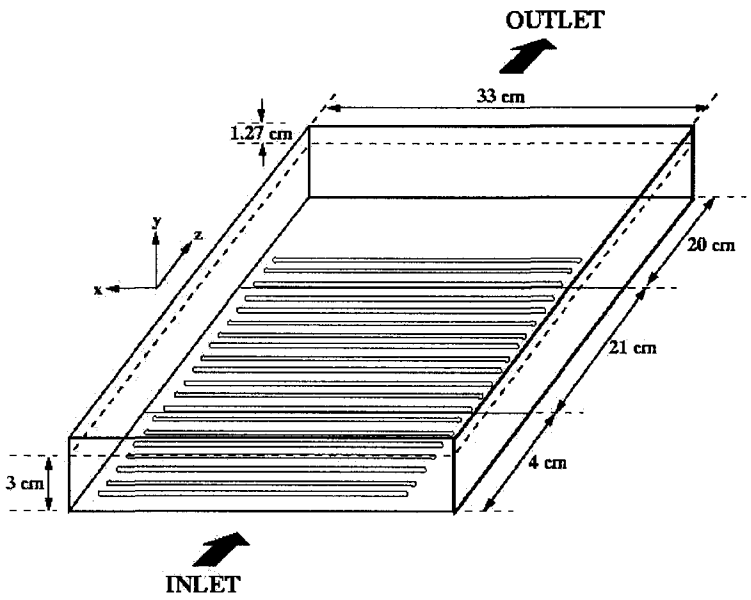

(a)

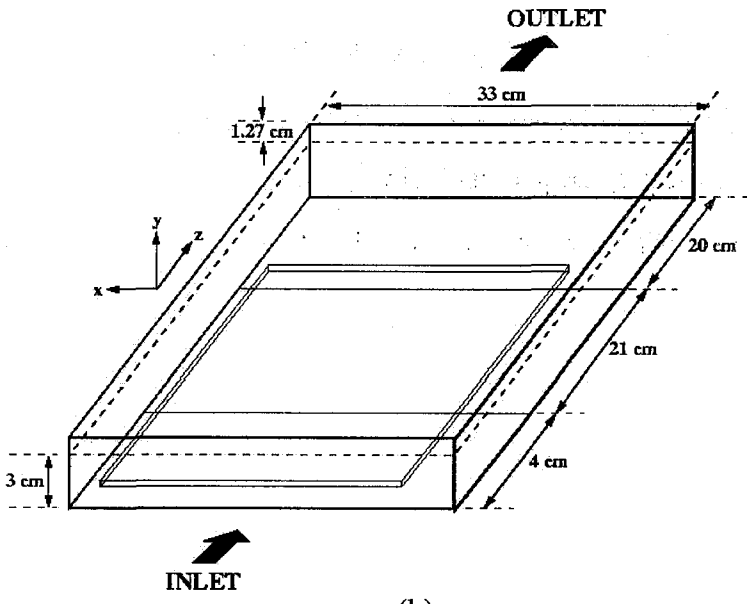

(b)

Figure 4.9 **The configuration of reactors that were compared in this study, (a) the reactor with the solid shape filaments, (b) the reactor with a rectangular hot gas volume.**

Table 4.3 Parameters used in the calculations for comparing the solid shape filaments reactor with the rectangular hot gas volume reactor

Parameters	
Volume of hot gas (cm^3)	32 × 0.1 × 24.1
Filament diameter (mm)	1
Filament length (cm)	32
Filament spacing (mm)	5
Reactor chamber height (cm)	3
Reactor chamber length (cm)	45
Reactor chamber width (cm)	33
Substrate area (cm^2)	33×21

The calculations were done at 1 torr pressure and a Reynolds number of 20. The boundary conditions used in the calculations were the same as the boundary conditions used in the horizontal arrangement study, as listed in Table 4.1, except for the hot gas temperature. The temperature of hot gas was set at 663 K since the gas around the filaments is observed to be below 700 K, the temperature of the filament surface. The actual gas array temperature was determined by using a trial and error procedure to meet the temperature profiles to those found in the reactor with cylindrical filaments. The grids generated by Gambit program (Fluent Inc., USA) for the reactor used in the calculations are shown in Figure 4.10 and Figure 4.11. The grids in the reactor with cylindrical filaments were tetrahedral cells, with the grid size of 2 mm, while the grids in the hot gas array were hexahedral with a size of 1 mm. The calculation was terminated when the convergence criteria for the continuum equation, the momentum equation, and the energy equation, and the species equations reached 1×10^{-6} or smaller. The criterion used in Fluent is the scaled residual which is defined as the imbalance of the conservation equation summed over all the

computational cells P divided by the flow rate of general variable ϕ through a domain. After discretization, the conservation equation for a general variable ϕ at cells P can be written as:

$$a_P \phi_P = \sum a_{nb} \phi_{nb} + b \,. \tag{4.5}$$

Hence, the scaled residual, R^{ϕ} is defined as

$$R^{\phi} = \frac{\sum_{\text{cells } P} \left| \sum_{nb} a_{nb} \phi_{nb} + b - a_p \phi_P \right|}{\sum_{\text{cells } P} \left| a_P \phi_P \right|}, \tag{4.6}$$

where ϕ_P is a general variable at cell P, ϕ_{nb} is a general variable at the neighboring cells, a_P is the center coefficient, a_{nb} are the influence coefficients for the neighboring cells, and b is the constant part of the source term and boundary conditions. The temperature profiles in the axial and vertical directions are plotted to check the validity of the effective filament array reactor (the hot gas reactor), and are shown in Figures 4.12 and 4.13.

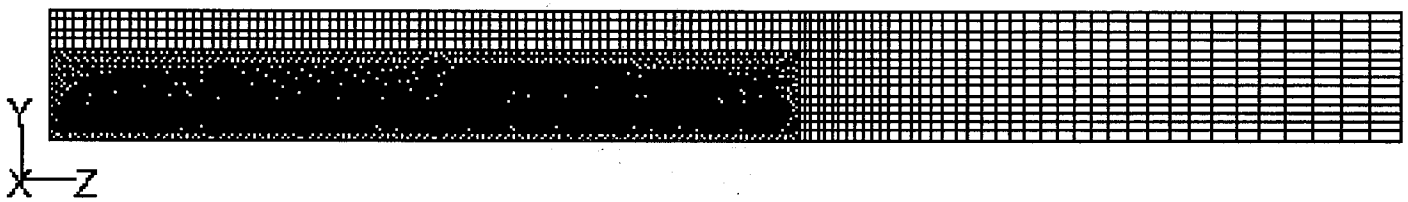

(a)

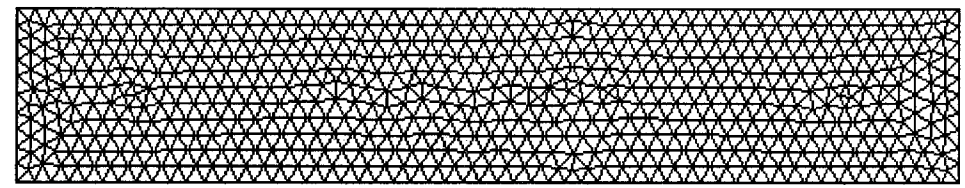

(b)

Figure 4.10 Grids generated for the reactor with the cylindrical filaments. The top figure, (a), shows the cross sectional view at the center plane of the reactor, and the bottom figure, (b), shows the cross sectional view of the reactor at the inlet plane.

(a)

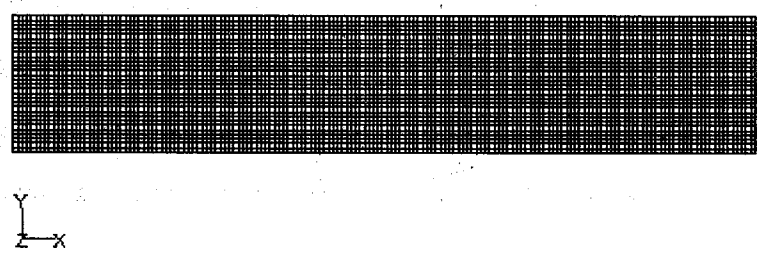

(b)

Figure 4.11 Grids generated for the reactor with surrogate filament array. The top figure, (a), shows the cross sectional view of the reactor at the center plane, and the bottom figure, (b), shows the cross sectional view of the reactor at the inlet plane.

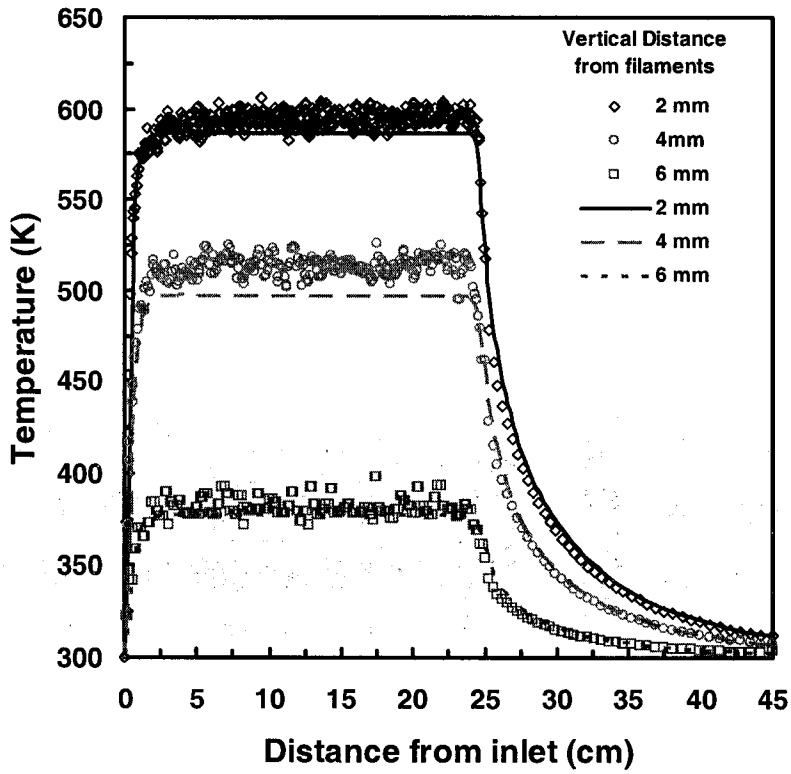

Figure 4.12 **Horizontal temperature profiles at different vertical distances from the filaments. The squares, circles, and diamonds represent the temperature profiles in the cylindrical filament reactors, and the lines represent the temperature profiles in the hot gas reactor.**

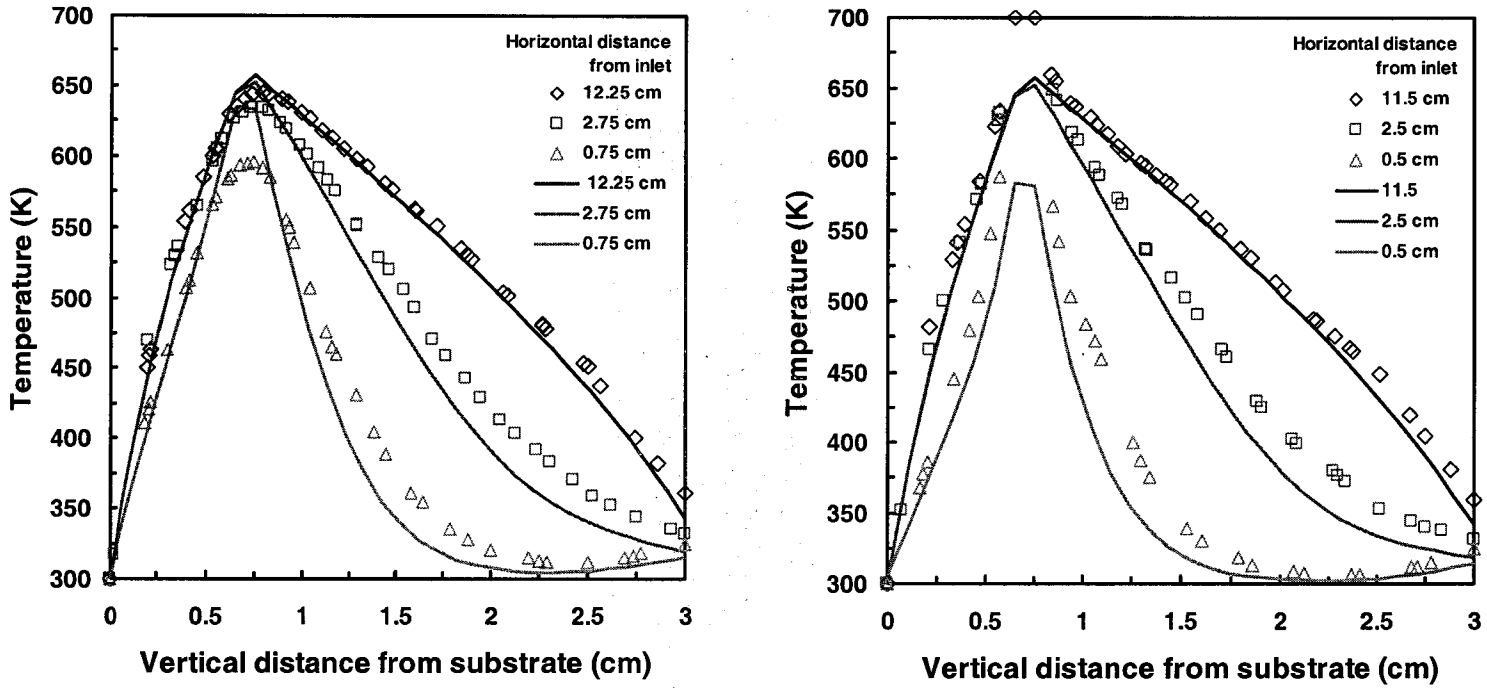

Figure 4.13 **Vertical temperature profiles at different axial positions. (a) The temperature profiles at the space between the filaments. (b) The temperature profiles at the filament position. Squares, diamonds, and triangles represent the temperature profiles in the reactor with the cylindrical filaments, while the lines represent the temperature profiles in the reactor with the effective filament array.**

Figure 4.12 and Figure 4.13 show the comparison of the temperature profiles in the axial and vertical directions, respectively, for the two filament array realizations. The axial profiles agree very well at 2 and 6 mm below the filament array. However, at 4 mm the profile from the hot gas reactor was a little bit lower than the profile from the cylindrical filament reactor. For the temperature profiles in the vertical direction, the temperature profiles below the filament array agreed very well with the effective array configuration. The temperature profiles of the hot gas array were lower than the temperature profiles of the cylindrical shaped filament reactor at the position of the filament array and above. The disagreement in temperature in this region might be the result of differing flow patterns, since for the cylindrical filament reactor the filaments are impermeable, and are immersed in gas flow. The gas must flow around these filaments while in the hot gas reactor the filaments are effective (virtual) and do not mechanically interfere with the flow. In the effective array configuration, the gas passes through this region and does not exhibit diversion of the flow. Plots of the velocity vectors at the filament array area, for the cylindrical filament reactor are shown in Figure 4.14. The gas moving toward the first filament creates a stagnation point near the surface of the filament and divides into two streams. The gas passing under the filaments rises upward downstream of the filament. Farther downstream this buoyant motion is not as pronounced, and the vectors are more horizontal in character. This result may explain why the gas temperatures around the filaments near the inlet for the cylindrical filament reactor were lower than the temperature at the same area in the hot gas reactor. Even though the temperature profiles do not quantitatively agree in the region above the filaments, the overall temperature profiles in both reactors show the same characteristics.

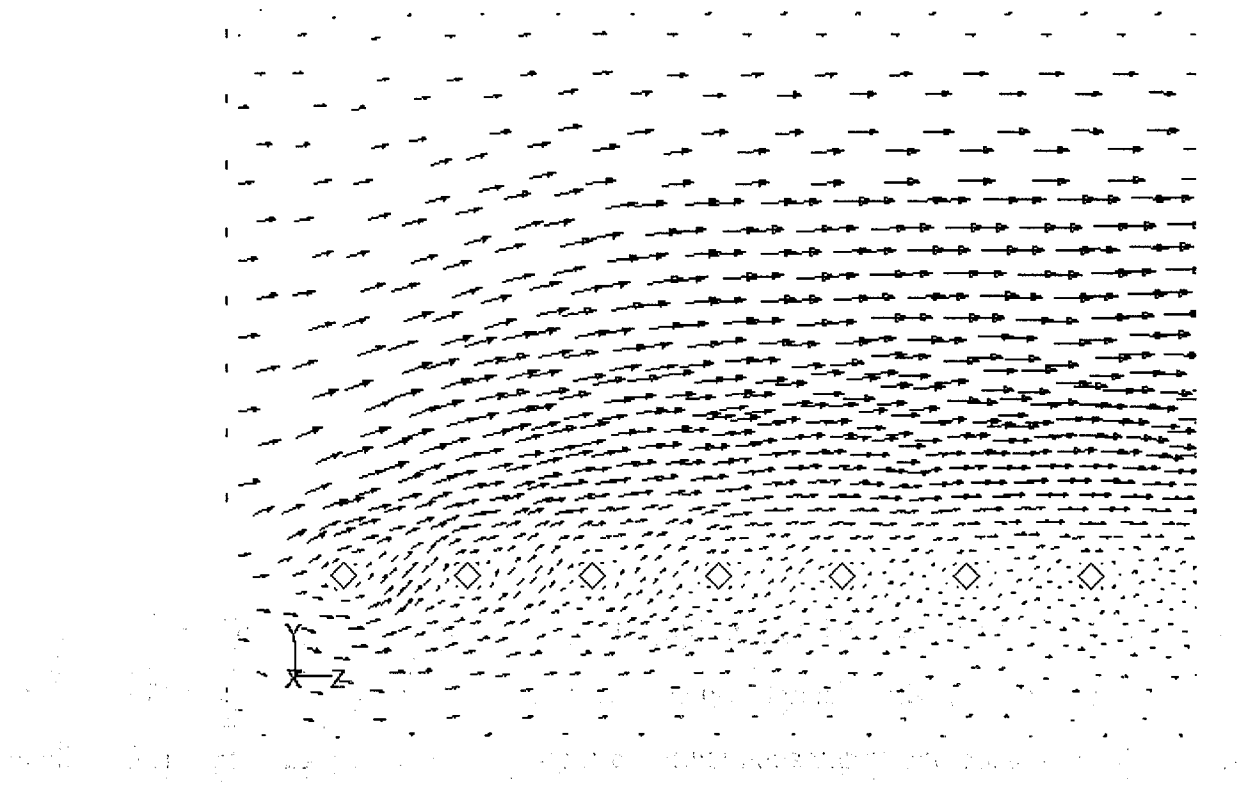

Figure 4.14 The velocity vectors plot at the center plane of the reactor witl cylindrical shaped hot filaments. The length of the arrow indicate the velocity magnitude at each location.

A plot of the CF_2 mass fractions is shown in Figure 4.15. As seen fron this figure, the predicted mass fraction distribution of CF_2 is in good agreement at 11.: cm and 24.5 cm from the inlet, which correspond to the center and end of the sub strate, respectively. However, the CF_2 mass fraction distribution near the beginning o the substrate (~4.5 cm from the inlet) was a little bit overestimated. Regardless, th CF_2 mass fraction distributions are considered to be in good qualitative agreement. I the future studies, the thickness of the hot gas volume would be increased and th

calculations would be done by using this reactor with effective array since it was simpler in creating the grids in this reactor than creating the grids in cylindrical filament reactor and the calculations were more accurate when the grids were close to the structured grids.

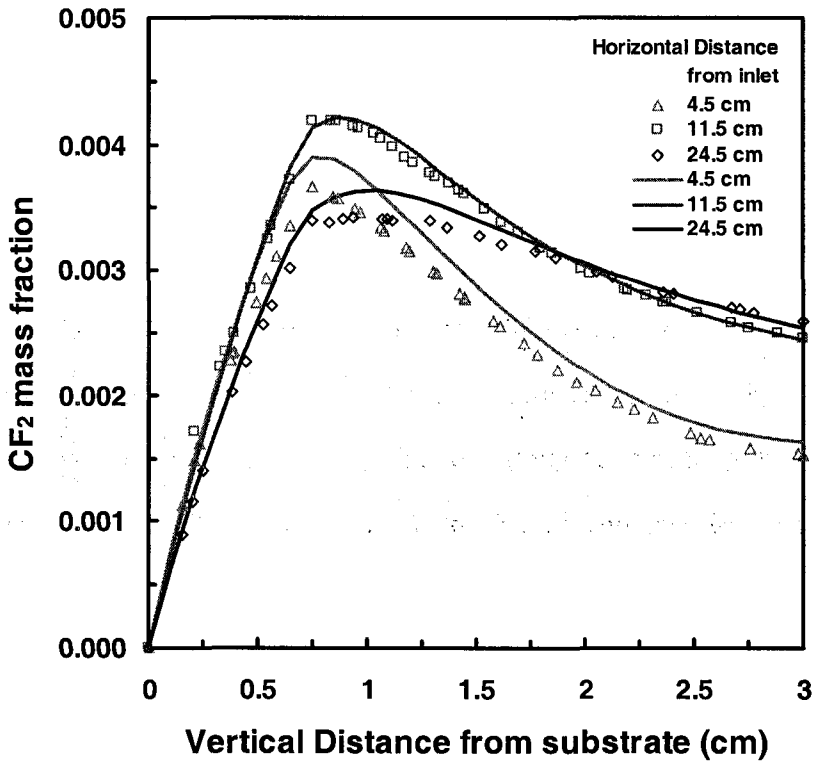

Figure 4.15 CF_2 mass fraction distribution in vertical direction at different axial position from substrate.

4.4 Summary

In this chapter two types of filament configurations have been examined to find the best arrangement to achieve uniform temperature profiles over the substrate by comparing the vertical arrangement with the horizontal arrangement. The results of the calculations show that the horizontal arrangement yields acceptable temperature profiles that were easily maintained. On the other hand, the vertical arrangement creates parabolic shaped profiles, which make it problematic to maintain temperature uniformity over the substrate. The filament diameter and the spacing between each filament are also crucial to the temperature profiles. Increasing the filament spacing and filament diameter increases temperature fluctuations. The optimum filament diameter is the smallest size that can readily be manufactured and arranged in an array. The optimum spacing is approximately $2d$ for filament diameters larger than 1 mm, or about 5 mm for a filament diameter less than 1 mm.

The technical issues associated with construction of structured grids in a reactor containing 20 to 100 small, cylindrical filaments make routine use of CFD a challenging task. Simply put, generating grids that capture filaments with diameters less than 1 mm is quite difficult because of the difference in scale between the filament and the reactor. To address this, real filament arrays were replaced by the volume of hot gas acting as a surrogate array, with temperature equal to the average temperature of the gas around the filaments. The results from this study show that the temperature profiles and CF_2 mass fraction from these two reactors were in good agreement. Thus, replacing the real filament array with the hot gas volume is an acceptable means of capturing the effects of the array without having to capturing its physical details.

Chapter 5

REACTOR CONFIGURATION

In Chapter 4, calculations for the idealized reactor, (i.e., the reactor with the hot gas volume), were compared with calculations for the reactor with cylindrical shaped filaments. The results confirmed that the temperature profiles in horizontal (z) and vertical directions (y) as well as the mass fraction profiles in both reactors were in good agreement. Therefore, the hot gas volume will be used instead of the actual filament array in the calculations associated with the following studies.

In this chapter, the effects of gas flow rate, the hot gas volume (surrogate filament) thickness, the space above the filaments, and the gap between the substrate and hot gas on the temperatures and mass fraction profiles will be examined. The calculations in chapter 4 were mostly done by solving the energy and momentum transfer equations under the assumption that the heat released from the reactions is negligible compared to the energy input from the hot gas volumes. In this chapter, the mass transfer equations are included in the calculations. The main objective is to find the optimal reactor configuration to achieve uniform deposition films over the substrate area.

5.1 Effects of Inlet Gas Flow Rate

In section 4.3, the simulation was performed by fixing the Reynolds number at approximately 20. The Reynolds number used in those calculations was

calculated from the average velocity of the inlet gas. The reactor chamber used in the calculations was 33 cm wide, 34 cm long and 3 cm high. The size of the hot gas volume was 1 mm thick, 32 cm wide and 24.1 cm long. The hot gas volume was placed at 6.5 mm above substrate and about 4 cm from the inlet. The dimension of the reactor and parameters used in the calculations are listed in Table 4.3. The configuration of the model reactor was shown in Figure 5.1. The operating pressure was set at 1 torr.

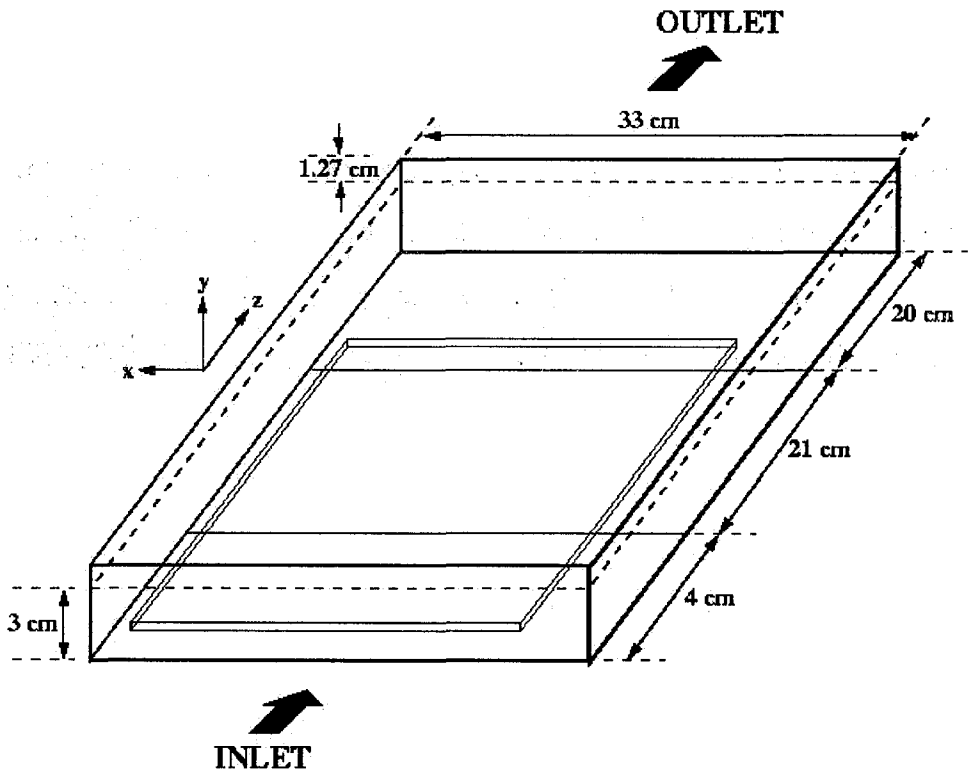

Figure 5.1 The configuration of reactors used in this study.

In this study, the inlet gas flow rate is varied from 0.001 to 0.1 m^3/s which is equivalent to a Reynolds number ranging from 2.75 to 275. The temperature of hot gas region was set to 663 K, which is the gas temperature near the filaments when the temperature of the filament surface is 700 K. Recall that this gas temperature was determined by a trial and error procedure to get the temperature profiles close to the temperature profiles from the cylindrical shaped filament reactor. The grids generated by Gambit program (Fluent Inc., USA) for the reactor used in the calculations were shown in Figure 4.10 and Figure 4.11. The calculation stopped when the criteria (scaled residual) of the continuum equation, the energy equation, and the species equations reached 1×10^{-6} or smaller.

Figures 5.2 (a), (b), and (c) show the temperature profiles in the axial direction (z) obtained from the calculations when the gas flow rates were 0.1, 0.01, and 0.001 m^3/s, respectively. At the highest gas flow rates (0.1 m^3/s, or Re ~275), the temperature becomes uniform about 7.5 cm from the inlet. When the gas flow rates decrease to 0.01 and 0.001 m^3/s, the temperature becomes uniform about 3 to 4 cm from the inlet. As the flow rate decreased, the entrance length (the length required for the temperature to develop into a uniform patterns) in the z-direction decreased as well.

Figures 5.3 (a), (b), and (c) display the temperature profiles in the vertical direction (y) for the gas flow rates of 0.1, 0.01, and 0.001 m^3/s, respectively. The temperature under the hot gas was uniform at about 5 cm from the inlet when the flow rate was 0.1 m^3/s. When the flow rates decrease to 0.01 and 0.001 m^3/s, the temperature was uniform at about 2 cm from the inlet. The decrease in gas flow rate decreased the entrance length of the reactor.

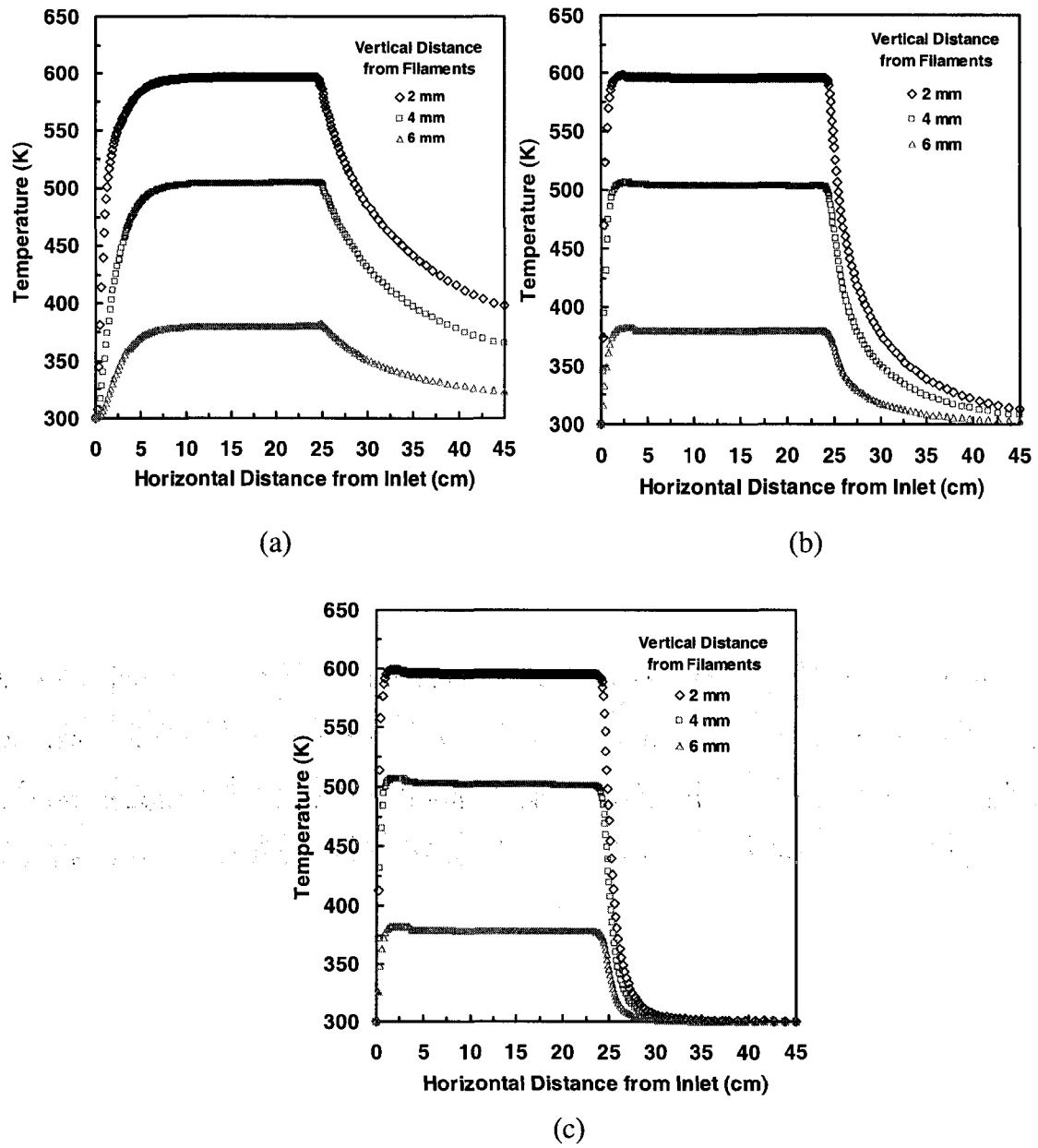

Figure 5.2 Horizontal temperature profiles at different vertical positions from the hot gas when varying the flow rate. (a) 0.1 m^3/s (b) 0.01 m^3/s (c) 0.001 m^3/s.

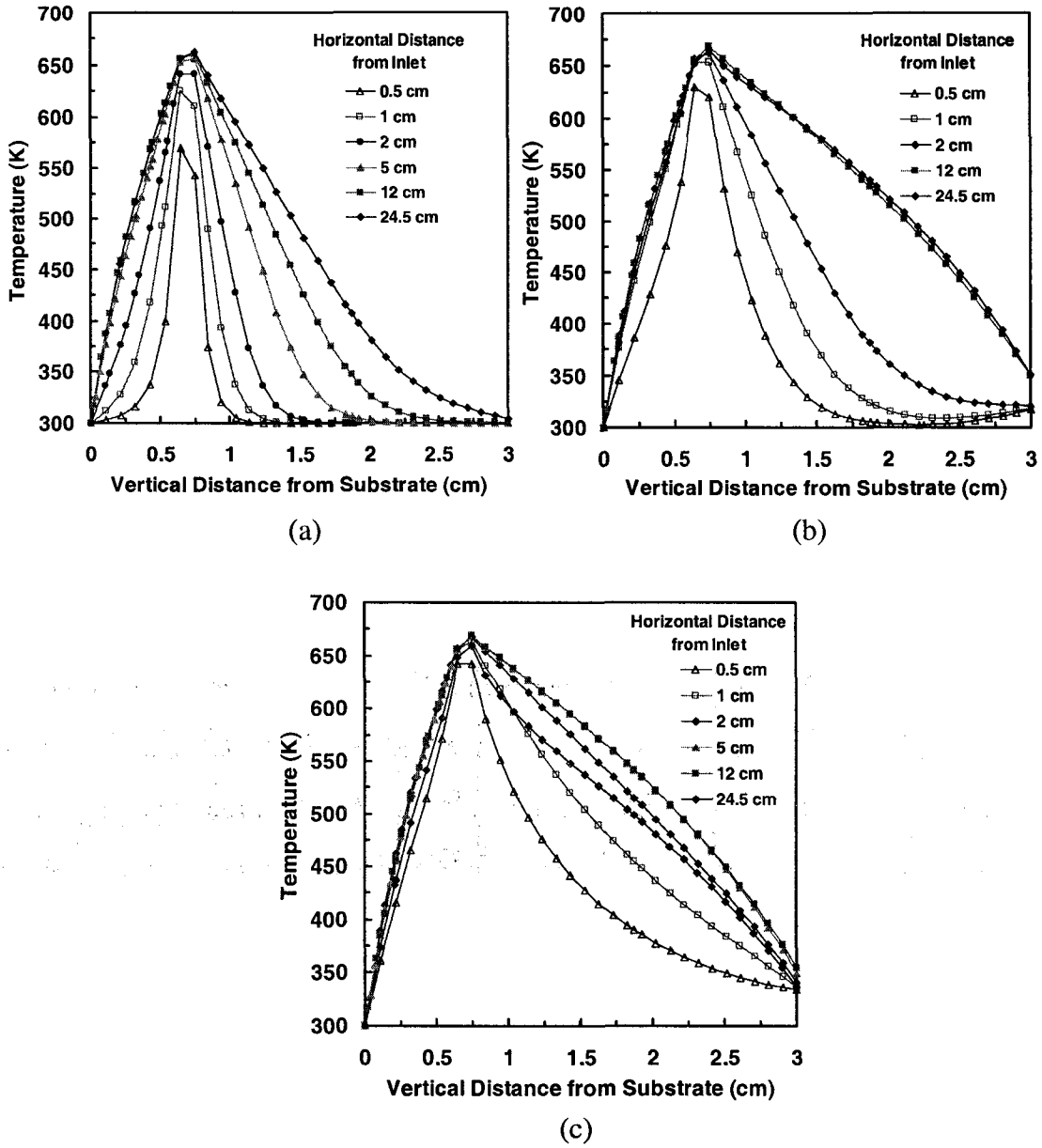

Figure 5.3 **Temperature profiles in a vertical direction at different positions from the inlet when varying the flow rate of gas. (a) 0.1 m^3/s (b) 0.01 m^3/s (c) 0.001 m^3/s.**

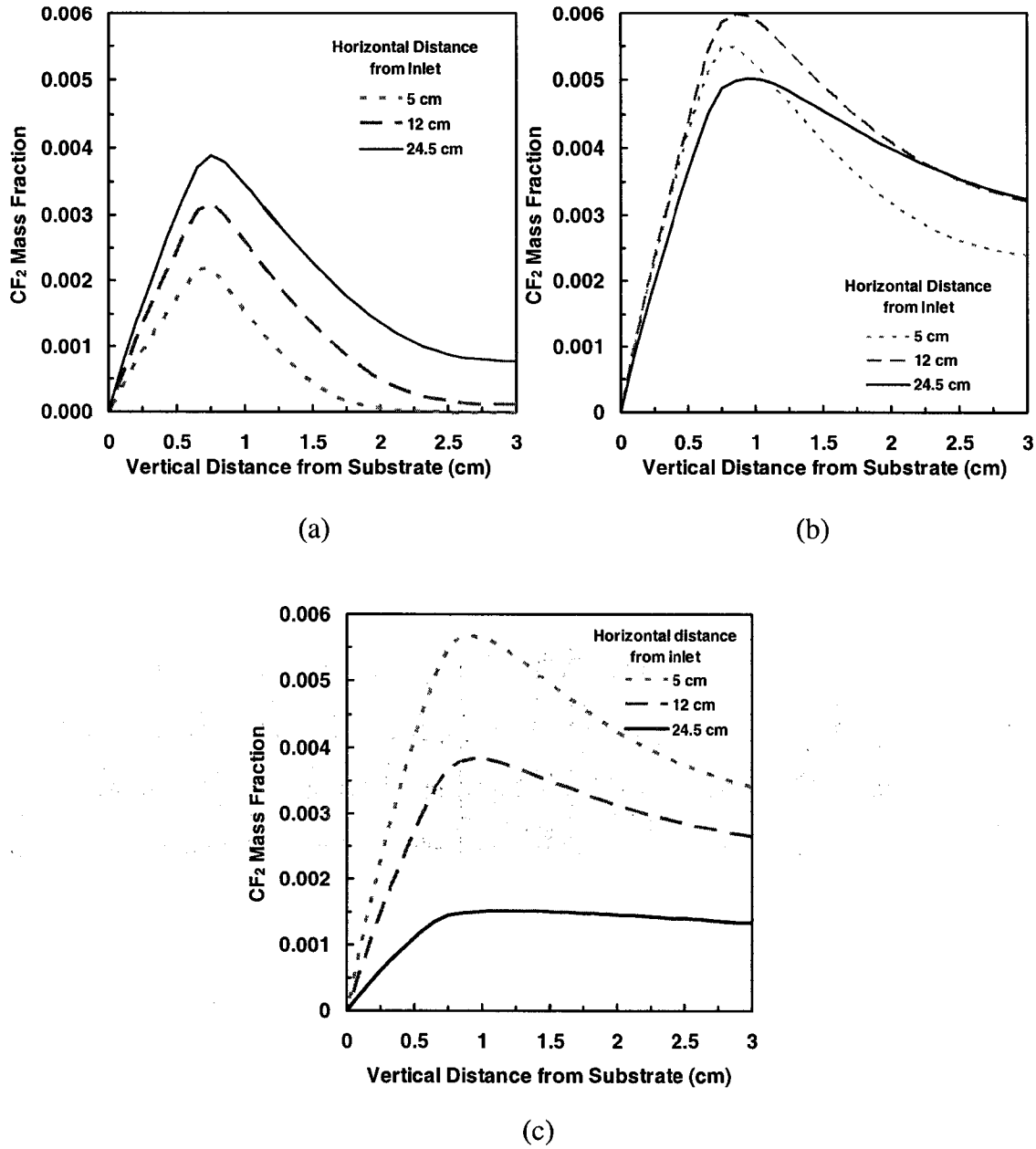

Figure 5.4 **CF_2 mass fraction profiles in a vertical direction (y-direction) at different positions from inlet when varying the gas flow rate. (a) 0.1 m^3/s (b) 0.01 m^3/s (c) 0.001 m^3/s.**

Although, the temperature profiles do not change significantly when gas flow rate are lower than 0.01 m^3/s, the deposited films will be uniform when the gradient of the precursor near the substrate is uniform over the substrate area. Figures 5.4(a), (b), and (c) show the CF_2 mass fraction profiles in the vertical direction at different axial positions when the gas flow rates are 0.1, 0.01, and 0.001 m^3/s, respectively. The results show that the mass fraction of CF_2 is higher at 0.01 m^3/s than with the other flow rates. At this flow rate, the mass fraction profiles do not vary appreciably at three different locations; the beginning of the substrate, the middle, and the end of the substrate. In contrast at the other flow rates, the mass fractions do vary along the axial direction. At the highest flow rate (0.1 m^3/s) the mass fraction was lowest at the beginning of the substrate, and then increased with axial position. This behavior is the result of convection moving CF_2 faster than it is consumed, and as a result it accumulates at the end of the substrate. On the other hand, at the lowest flow rate (0.001 m^3/s), the maximum concentration occurred at the start of the substrate region, and then increased along the axial direction. In this case convection was too low, and CF_2 was consumed as it passed over the substrate.

5.2 Effects of the Hot Gas Volume (Surrogate Filament) Thickness

The reactor configuration used in this study was the same as the reactor used in the previous study (see Table 4.3). The calculations were also done at 1torr pressure and a Reynolds number of 20. The boundary conditions used in the calculations were the same as those used in the previous study (shown in Table 4.1), except for the hot gas temperature. The gas temperature around the filaments, which was treated as a thin rectangular volume of hot gas inside the reactor, was set at 663 K

throughout the hot gas region. This temperature was equivalent to the temperature of the gas around the hot filament when the temperature of the filament surface was set at 700 K. The thickness of the hot gas region was varied in the study: 0.1, 0.3, 0.5, and 0.7 cm. Increasing the hot gas region thickness means there is more than one layer of filament in the array. The lower surface of the hot gas volume was fixed at 6.5 cm above the substrate area.

Figure 5.5 shows the plot of temperature profiles in the axial direction as a function of distance from the inlet. As the thickness of the hot gas is increased, the temperature increases a few degrees at the region near the inlet and then remains constant for all vertical positions, in all cases. The temperature profiles are also plotted against the vertical distance from the substrate for 1 mm, 3 mm, 5 mm, and 7 mm thicknesses in Figure 5.6. The temperature near the inlet (i.e., 0.5 cm from the inlet) increases as the thickness of the hot gas increases from 1 to 3 mm. For all cases, the temperature profiles below the hot gas zone became fully developed within 2.5 cm of the inlet. When the thickness of the hot gas increases from 3 to 5 to 7 mm, the profiles do not change. The profiles above the hot gas zone do change with thickness because more of this space is occupied by the hot gas as its thickness increases. Since the temperature profiles between hot gas zone and substrate do not vary for thicknesses greater than 3 mm, it may be inferred the optimum thickness is between 3 and 7 mm. The thicker hot gas would increase the rate of reaction of gas phase reactions which in turn would increase the amount of CF_2 in the CVD reactors.

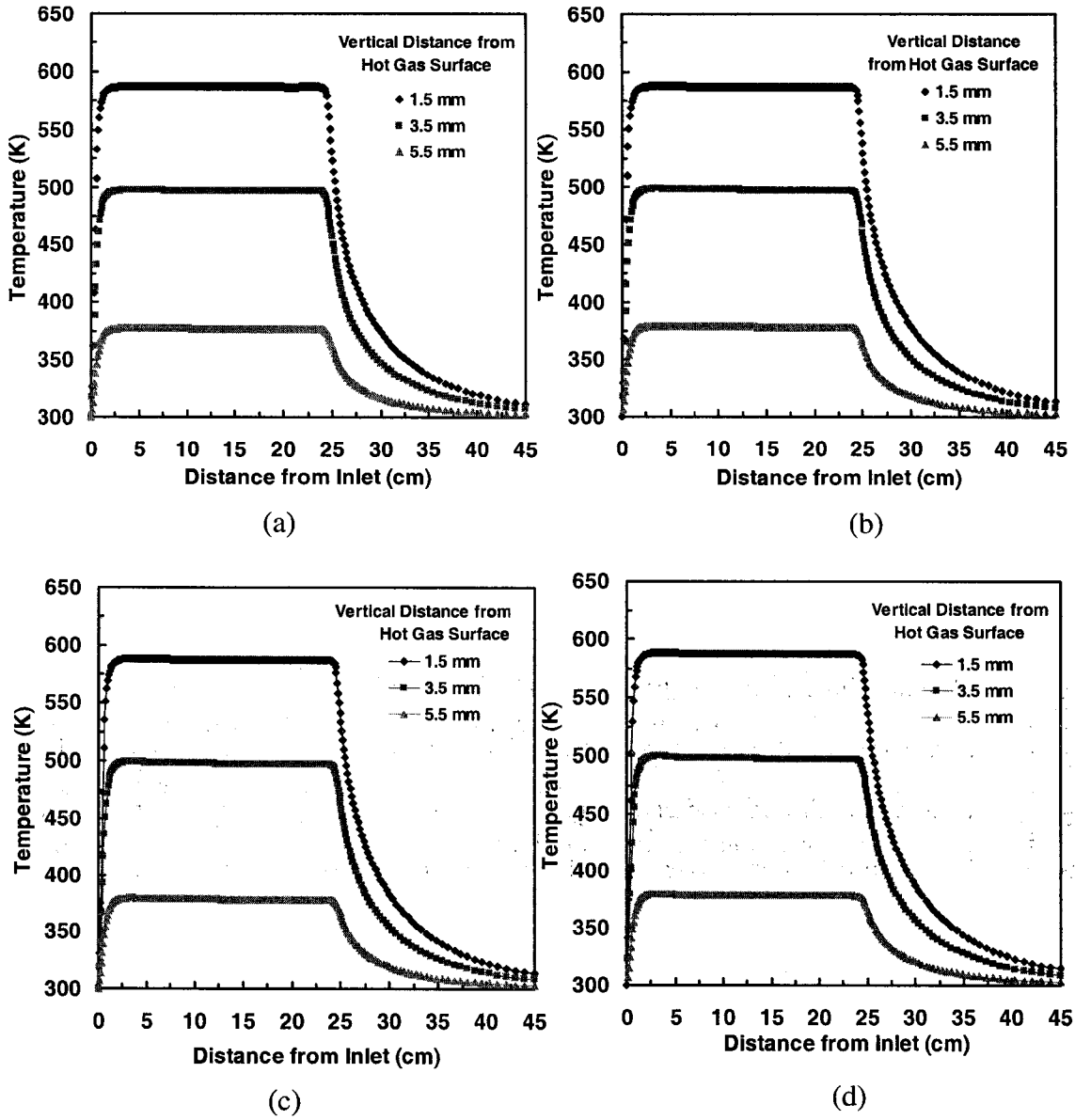

Figure 5.5 **Temperature profiles along the axial direction (z-direction) at different vertical positions when varying the thicknesses of the hot gas. (a) 0.1 cm. (b) 0.3 cm (c) 0.5 cm (d) 0.7 cm.**

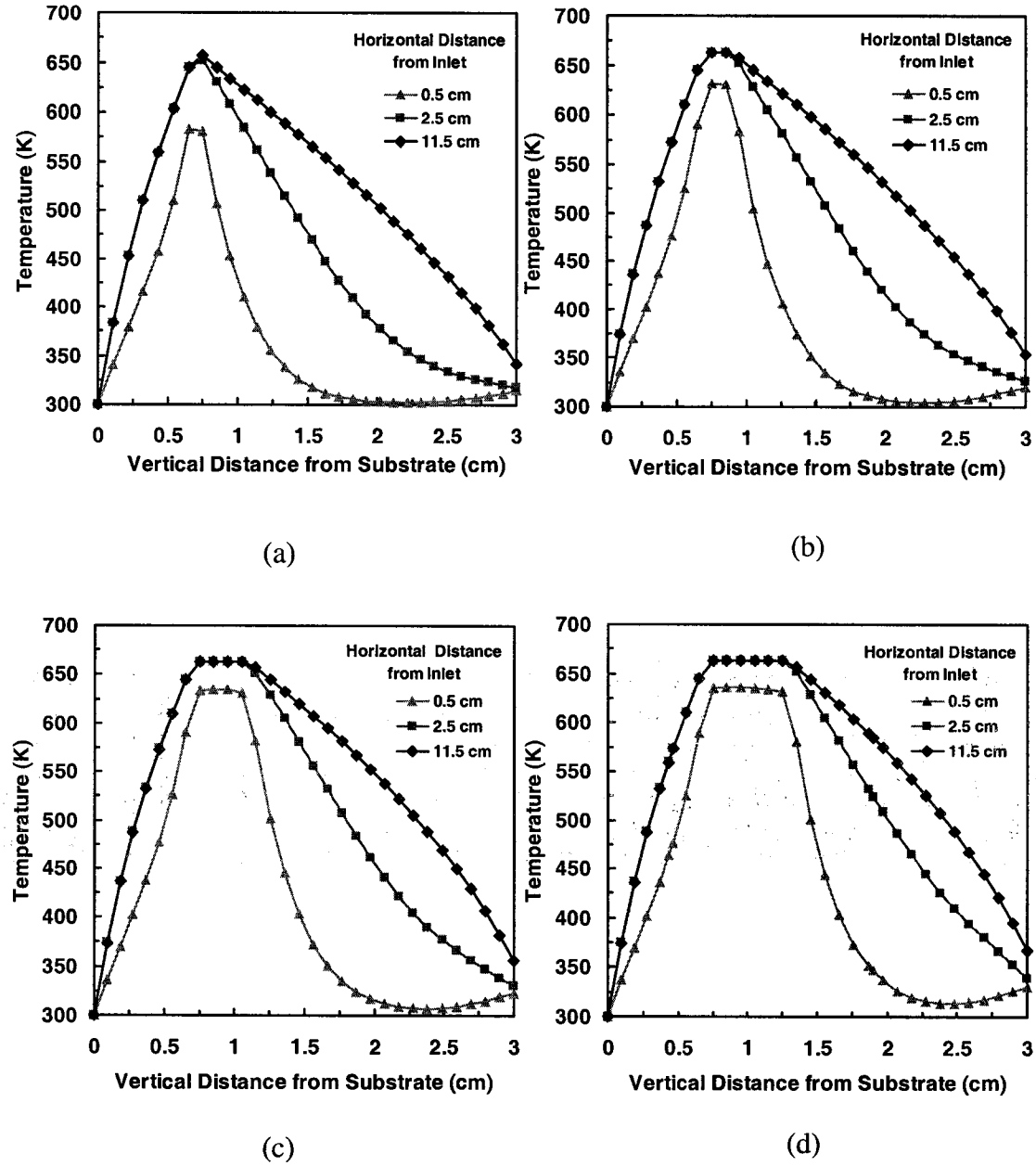

Figure 5.6 **Temperature profiles along the vertical direction (y-direction) at different axial positions with various thicknesses of the hot gas. (a) 1 mm. (b) 3 mm. (c) 5 mm. (d) 7 mm.**

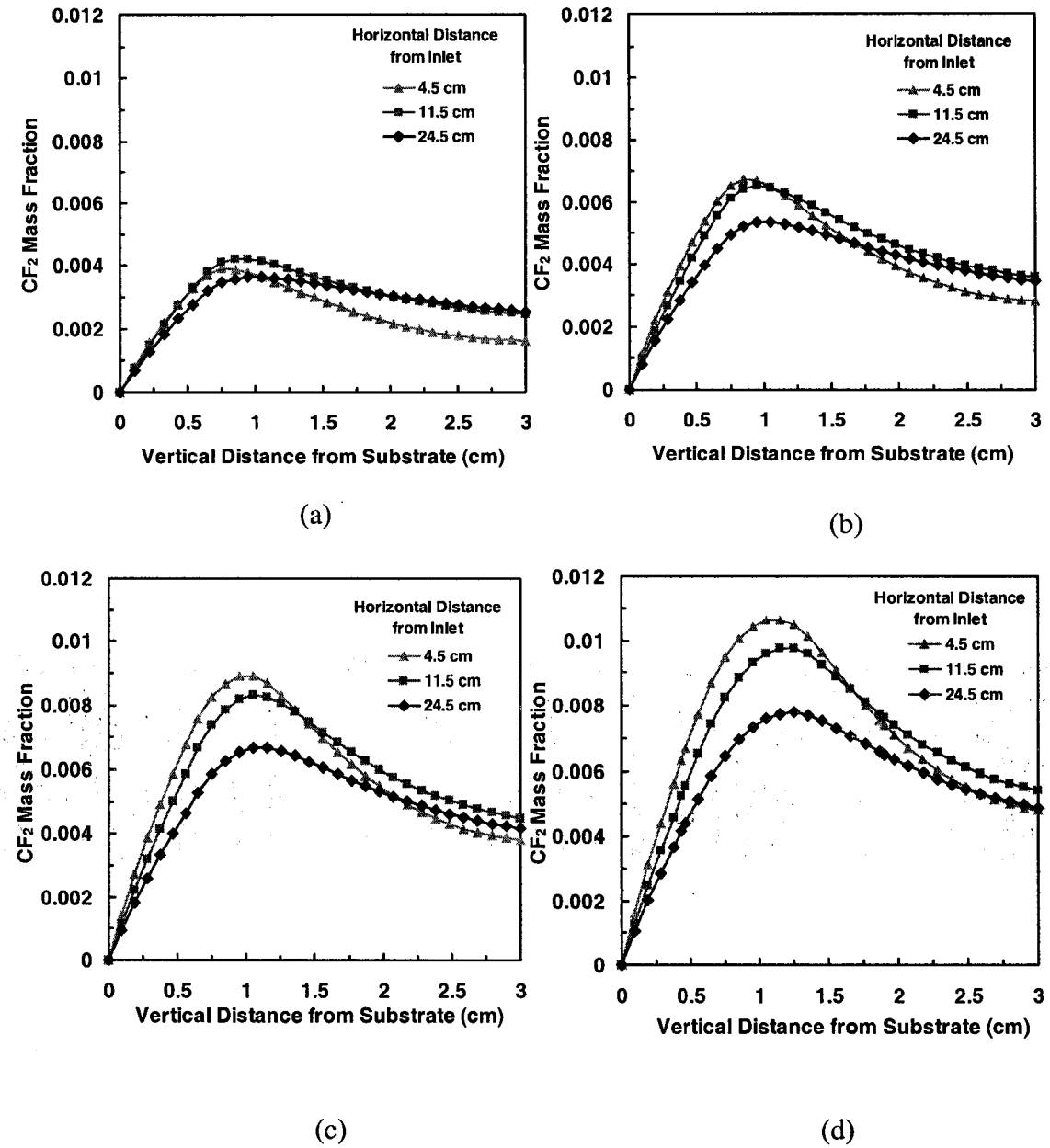

Figure 5.7 **CF_2 mass fraction profiles along the vertical direction (y-direction) at different axial positions with various thicknesses of the hot gas. (a) 0.1 cm (b) 0.3 cm (c) 0.5 cm (d) 0.7 cm.**

Figure 5.7 shows the vertical CF_2 mass fraction profiles at different axial positions. As the hot zone thickness increases, the CF_2 mass fraction increases from 0.004 to 0.01, or about 150%. The maximum CF_2 mass fraction occurs about 4.5 cm from the inlet, which is the leading edge of the substrate for all cases, except for the case when the hot gas thickness was 1 mm. Thus, increasing the hot gas volume increases the mass fraction of the CF_2 above substrate area. It is important to note that thickness of the hot gas will be limited by the heat loss from the top surface to the surroundings.

5.3 Effects of the Space above the Filament Arrays

In section 5.2, the thickness of the hot gas region was varied to examine its effect on the temperature and mass transfer profiles. The results showed that the temperature profiles in both directions (axial and vertical direction) were insensitive to changes in thickness of the hot gas region. The most significant impact was on the species distributions. Increasing the thickness of the hot gas increased the extent of gas phase reactions, resulting in an increase in CF_2 mass fraction.

Now, the focus will be on heat transfer characteristics. When the thickness of the hot gas increases, the overhead space above the hot gas reduces because the size of the reactor, and the space between the hot gas and substrate were both fixed. The region above the filament arrays is not utilized in the process since activated species (CF_2) in that region will diffuse away from the substrate, to the top wall direction. The larger the gap above the filaments, the more reactant gas required. In this study, the space above the filaments was reduced from 1.65 cm to 1 cm and 0.5 cm. The hot gas thickness was fixed at 7 mm, while the space between the hot gas

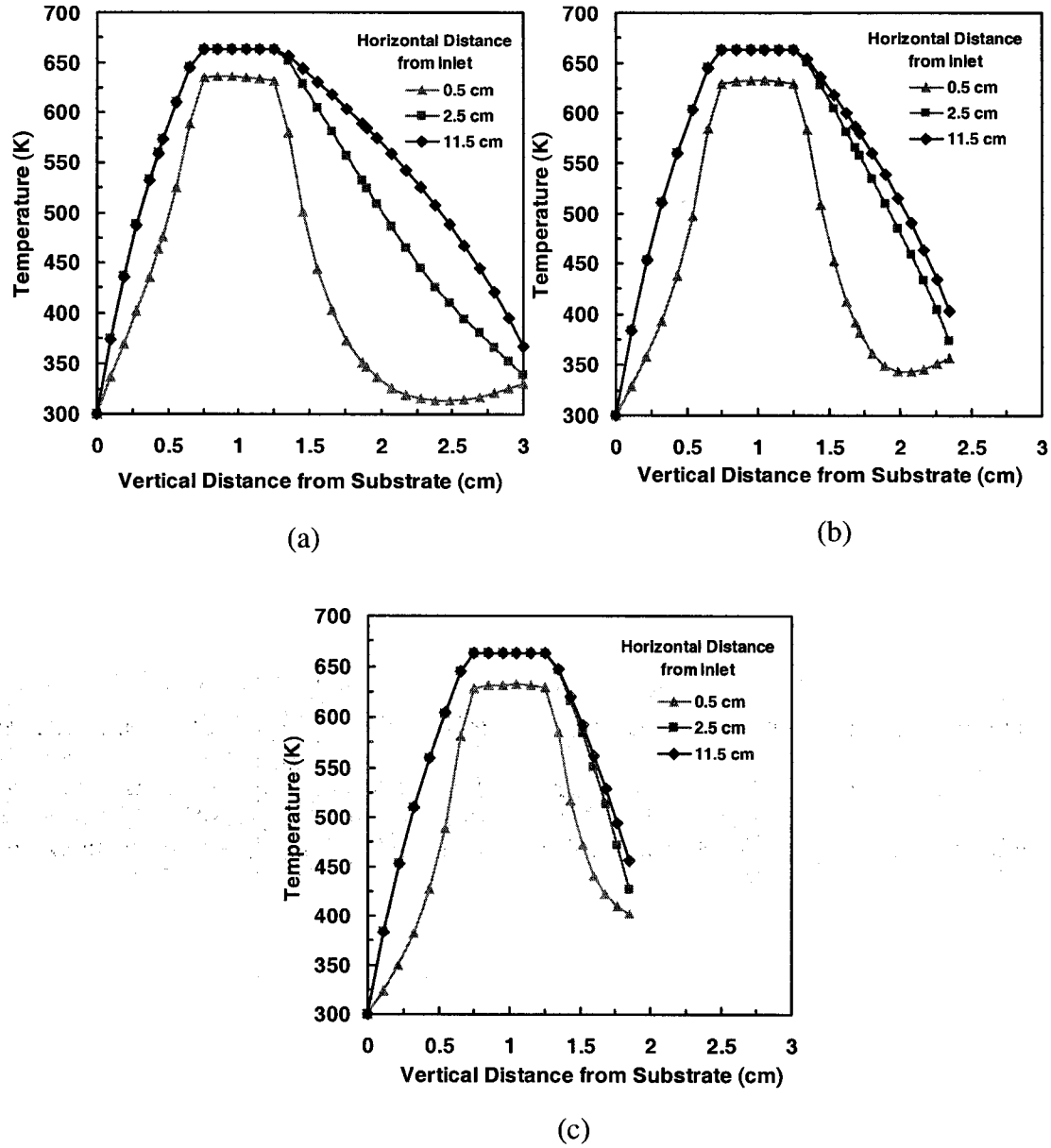

Figure 5.8 **Temperature profiles in a vertical direction at different positions from the inlet varying the space above the hot gas volume. (a) 1.65 cm (b) 1 cm (c) 0.5 cm.**

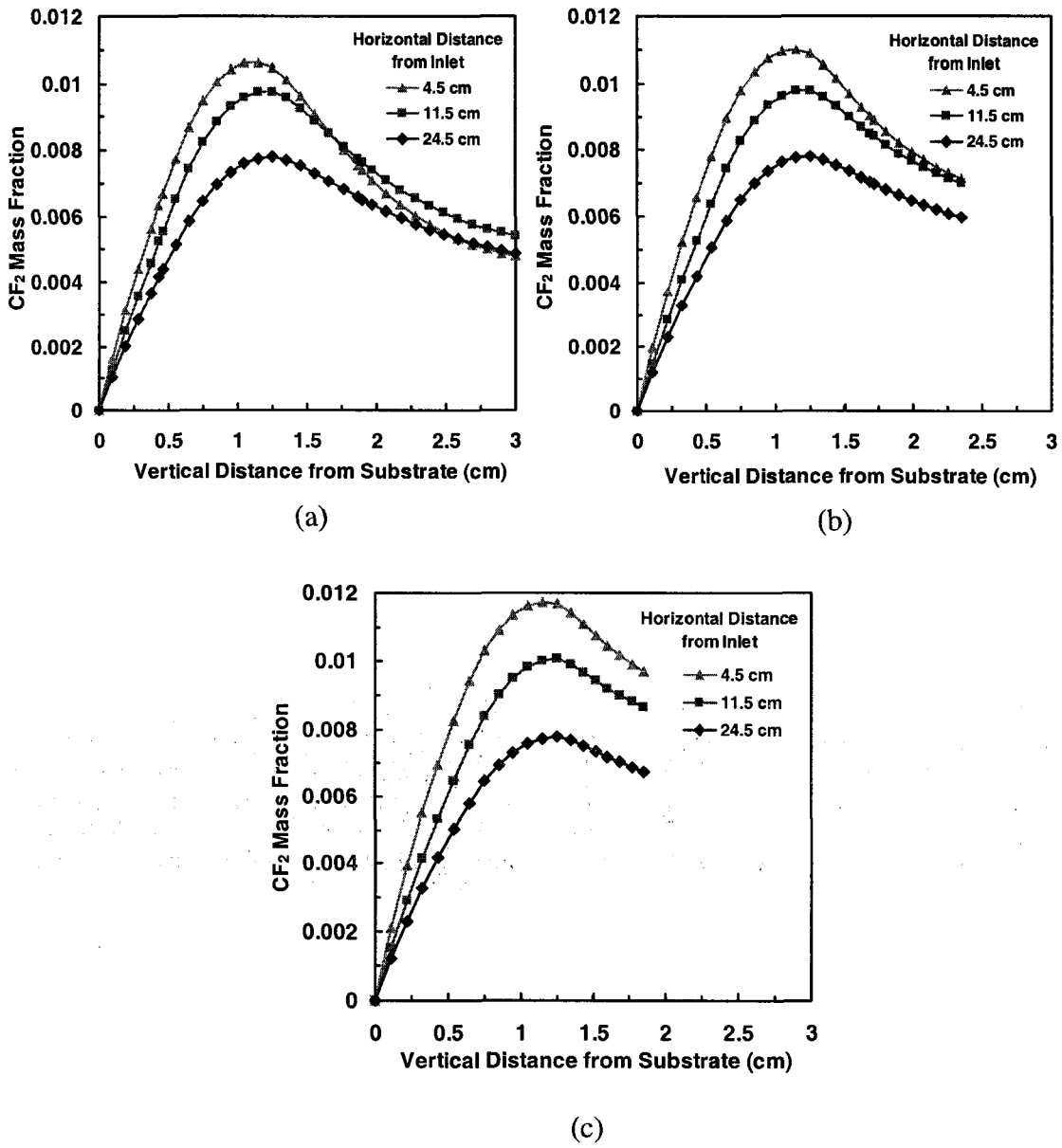

Figure 5.9 **CF_2 mass fraction profiles at different positions from the inlet by varying the space above the hot gas region. (a) 1.65 cm (b) 1 cm (c) 0.5 cm.**

and the substrate was fixed at 6.5 mm. All other reactor configuration is the same as in Figure 4.9, and all the reactor parameters are listed in Table 4.3.

The temperature profiles and the CF_2 mass fraction profiles are shown on Figures 5.8 and 5.9, respectively. Figure 5.8 displays the temperature profiles in the vertical direction at different axial locations. In all calculations, the temperature profiles below the hot gas region were found to be the same. Only the temperature profiles above the hot gas changed due to the decrease in gap height, and this did not affect the film deposition. In contrast, the CF_2 profiles at the leading edge of substrate increases approximately 10%, which in turn increases the CF_2 gradient near the substrate and the rate of deposition. So the optimal gap height above the filament arrays is approximately 5 mm.

5.4 Effects of the Space between the Substrate and the Hot Gas

In this study, the space between the substrate and the filament array was reduced from 6.5 mm to 5 mm, using the same reactor configuration as the previous study. Figures 5.10 and 5.11 show the temperature and CF_2 mass fraction profiles in the vertical direction at different axial locations. As seen from both figures, reducing the space between the substrate and the filaments array from 6.5 mm to 5 mm did not change the overall shape of profiles, but it did increase the gradient near the substrate. Decreasing space between substrate and filament arrays results in a smaller reactor size, which in turn lowers the required reactant flow rate. The optimal space between substrate and filaments is around 5-7 mm.

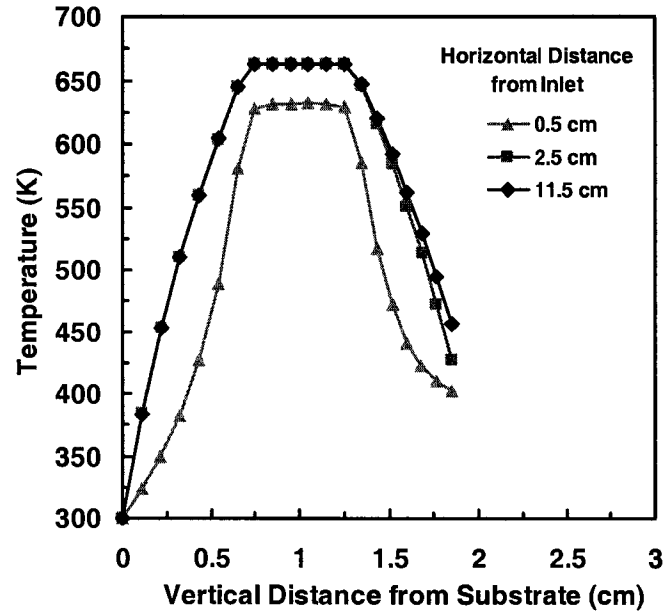

(a)

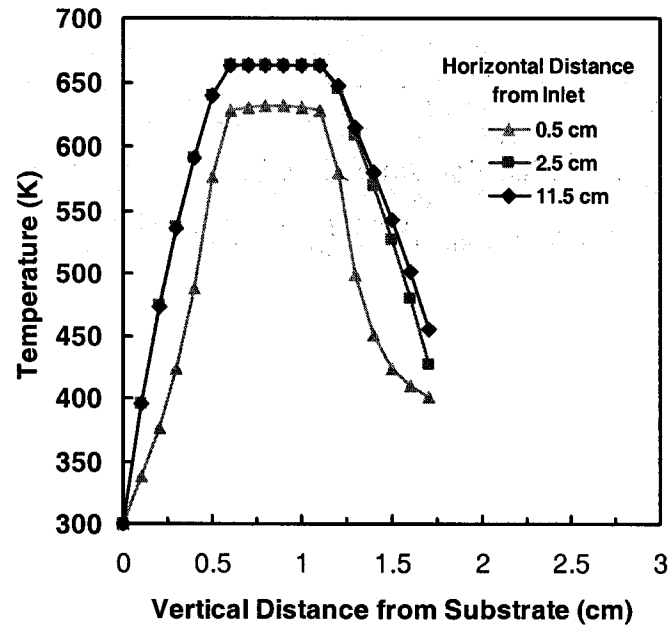

(b)

Figure 5.10 Temperature profiles in vertical direction at different positions from the inlet varying the space between the substrate and the hot gas. (a) 6.5 mm (b) 5.0 mm.

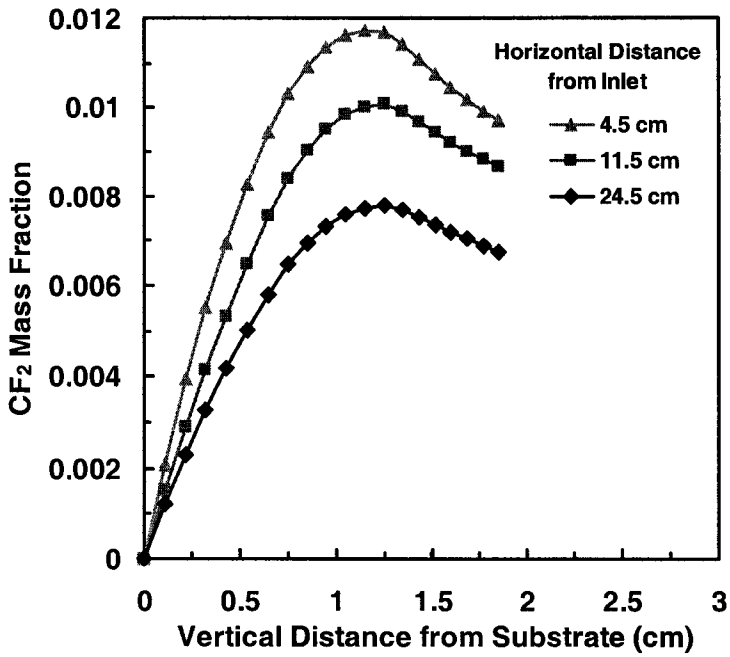

(a)

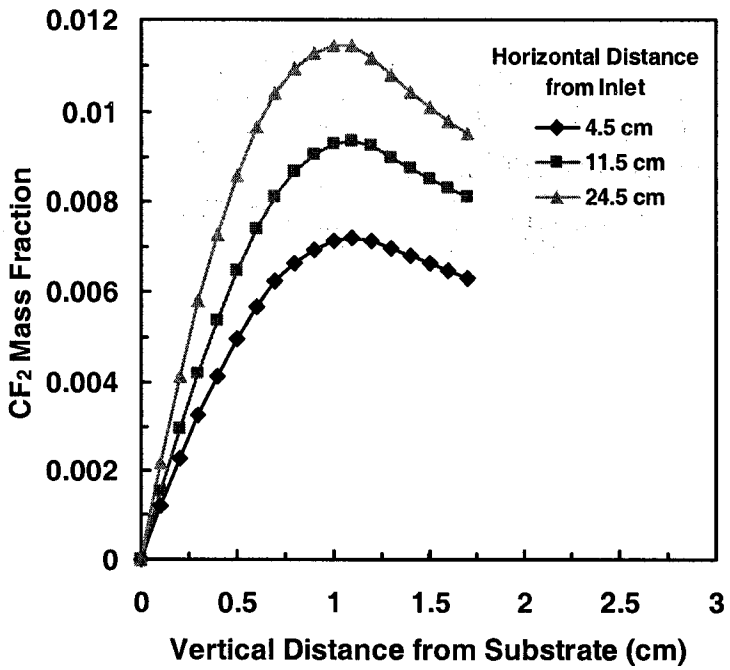

(b)

Figure 5.11 CF_2 **mass fraction profiles at different positions from inlet when vary the space between substrate and hot gas. (a) 0.65 cm (b) 0.5 cm.**

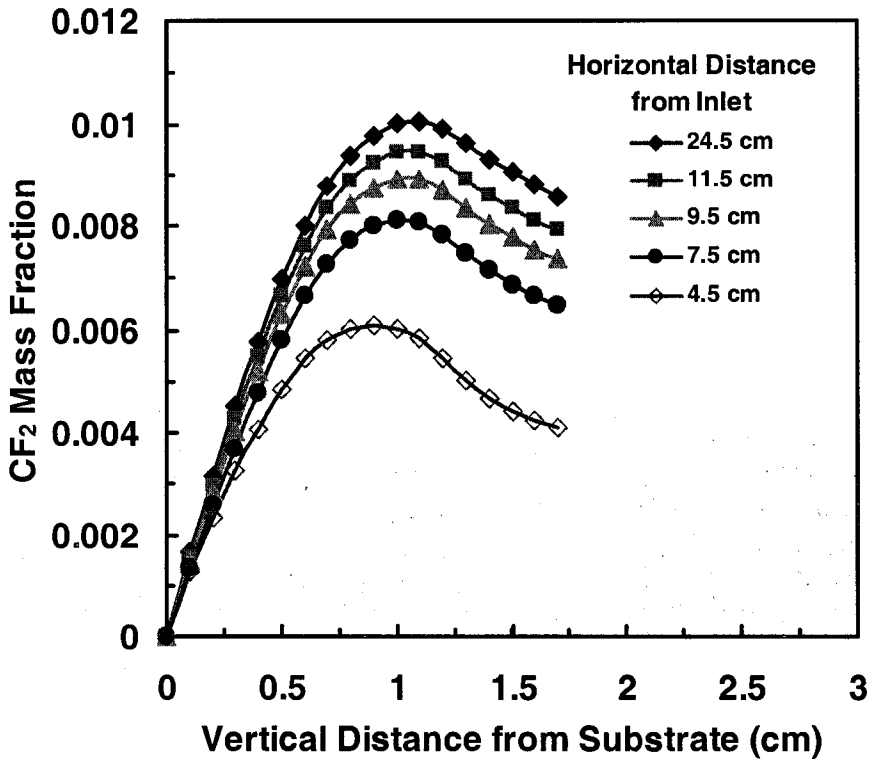

Figure 5.12 CF_2 **mass fraction profiles at different positions from inlet when the gas flow rate is 0.05** m^3/s.

Since the reactor configuration has been changed a little, one simulation has been performed to check that the more uniform CF_2 gradient can achieve by controlling the flow rate. The calculations showed that increasing the flow rate from 0.01 m^3/s to 0.05 m^3/s, changed CF_2 mass fraction profiles as shown in Figure 5.12. Uniform CF_2 gradient starts at 7.5 cm from the inlet. This recommends that the substrate region should start here to get the uniform mass gradient over the substrate area.

5.5 Summary

The effects of the gas flow rate, the thickness of the hot filament array, spacing between substrate and the reactor top wall, and spacing between substrate and hot filament array have been investigated in this chapter. The main objective of this investigation is to see the sensitivity of film deposition on these parameters. The following conclusions can be drawn.

By changing the reactor flow rate from 0.001 to 0.1 m^3/s significant changes were observed for both the temperature and mass fraction profiles. Uniform temperature is achieved when the flow rate was intermediate, at 0.01 m^3/s. The CF_2 mass fraction gradient near the substrate surface is highest and more uniform when the flow rate is approximately 0.01 m^3/s. However this optimal flow rate will be changed if the reactor configuration was changed.

The second parameter that has been investigated is the thickness of the hot gas volume. Increasing the thickness of the hot gas volume means there is more than one layer of the filament in the array. Increasing the hot gas region thickness above 3 mm did not change the temperature profiles below the filaments, but did increase the

extent of the reaction in the reactor, resulting in higher CF_2 gradients near the substrate.

When the space above the filament array was reduced from 1.65 cm to 0.5 cm, the temperature profiles below the filament arrays did not change, In contrast, the CF_2 mass fraction gradient near the substrate is increased. The optimal space above filament is as small as possible as long as the reactor can be manufactured.

The last parameter that has been investigated is the space below the filaments array. Again, decreasing the space below the filament from 6.5 to 5 mm does not significantly change both the temperature and CF_2 mass fraction profiles near the substrate. The optimal is somewhere between 5-7 mm.

Chapter 6

CONCLUSIONS AND RECOMENDATIONS

6.1 Conclusions

The objective of this research is the design of a new, one-dimensional, continuous flow HFCVD reactor using a rigorous computational fluid dynamics (CFD) approach. The reactor geometry strongly affects the flow characteristics, which in turn affects the properties of films. The uniform concentration-boundary layer thickness over the substrate is required to achieve good quality films. The studies in this research have been directed toward the design of this one-dimensional flow HFCVD reactor.

To validate the CFD approach with experiment, a set of preliminary simulations were performed for two different cylindrical reactor configurations, with and without an inlet showerhead. The reactor with shower-head inlet feed has the shorter overhead space above the substrate The conditions used in calculations for both configurations were 48 m/s inlet velocity (corresponding to 30 sccm flow rate), 1 torr pressure at the inlet, and 0.3 W/cm^3 heat generation rate in the hot filament zone. The simulation predicted a recirculating flow pattern occurred around the centerline in the cylindrical reactor without showerhead inlet. The associated non-uniform flow and temperature profiles correlated directly to non-uniform thickness of films deposited in this reactor. Films near the wafer edge are thinner than at the wafer center. These results demonstrate the effects of the reactor geometry on the film uniformity.

Increasing the flow rate increased the non-uniformity of the temperature contours, with recirculation still occurring over the substrate in even more complicated patterns. When the geometry of the reactor was changed by decreasing the overhead space above the substrate through the use of a showerhead inlet, both the velocity vector plots and temperature contours from this new geometry showed significant improvements in uniformity; recirculation zones disappeared and the temperature was significantly uniform above the substrate area.

The ability to capture non-uniform flow pattern in the cylindrical reactor confirmed the validity of the model. The developed model is used to determine appropriate configuration for the inlet showerhead that will result in a uniform inlet flow across the area where the substrate would be located and to investigate the sensitivity of the inlet flow characteristics on the showerhead configuration, the effects of the spacing between holes in the inlet showerhead, space near the walls, and the diameter of the showerhead holes have been investigated. The ideal configuration is an array of very small, closely spaced holes. However, the smaller the diameter, the higher the cost of the showerhead due to manufacturing challenges, and the larger pressure drop required to obtain a desired flow rate. The results from these studies indicate that there is little effect on the entrance length and the shape of the velocity profiles due to the showerhead hole spacing, showerhead hole-diameter, and spacing near the chamber walls. The entrance lengths obtained from the simulations were fitted by the least square method with R^2 value of 0.89. The slope of the correlation obtained from this study are reasonably close to Atkinson's equation, but the intercept is about half of Atkinson's value. The velocity profiles derived from Navier-Stokes

equation for a rectangular chamber showed very good agreement with the simulation profiles.

Next, two possible filament arrangements were examined to determine the appropriate filament configuration. In the first configuration, the filaments were arranged perpendicular to the flow, at a uniform height above the substrate, and were called the horizontal filament arrangement. In the second configuration, the filaments were stacked vertically near the reactor inlet, again oriented perpendicular to the flow, referred to as the vertical filament arrangement. The effects of the filament diameter and the spacing between filaments on the temperature distribution in the gas above the substrate region were investigated. Only the momentum and energy conservation equations were used in the calculations. All the calculations were done at 1 torr pressure, with a HFPO inlet flow rate of 790 sccm. These parameters are equivalent to a Reynolds number of 20. The analytical expression derived from the Navier-Stokes equation for a rectangular channel was applied as the inlet velocity boundary condition gas flow. The assumption of fully developed flows was applied in this study. The results of the calculations show that the horizontal arrangement yields acceptable temperature profiles that were easily maintained. On the other hand, the vertical arrangement creates parabolic shaped profiles, which make it problematic to maintain temperature (and therefore concentration) uniformity over the substrate. The filament diameter and the spacing between each filament are also crucial to the temperature profiles. Increasing the filament spacing and filament diameter increases temperature fluctuations. The optimum filament diameter is the smallest size that can readily be manufactured and arranged in an array. The optimum spacing is approximately two times of the diameter for filament diameters larger than 1 mm, or about 5 mm for

filament diameters less than 1 mm. Since the optimal filament size is less than or equal to 1 mm, the process of generating grids with the actual shape filament geometry for diameters below 1 mm is very challenging because of the extreme differences in size between the filaments and the reactor. To address this technical complication an alternate effective filament array representation was examined. Instead of reproducing the actual shape of small filaments inside the reactor, the region where the filament arrays located was replaced by a thin volume of hot gas with a temperature equal to the average temperature of the gas around the actual filaments. The results from this study show that the temperature profiles and CF_2 mass fractions from the surrogate filament array were in good agreement with the cylindrical filament array. Thus, replacing the real filament array with the hot gas volume is an acceptable means of capturing the effects of the array without having to capture its physical details

The effects of gas flow rate, hot gas volume thickness, the space above the filaments, and the space between the substrate and hot gas on the temperature and mass fraction profiles were investigated using the reactor with the surrogate filament array. The objective is to find the right reactor configuration to be able to deposit uniform films over the entire substrate area. By changing the reactor flow rate in the range of 0.001 to 0.1 m^3/s (which is equivalent to the Reynolds number of 2.75 to 275) significantly changed both the temperature and mass fraction profiles. Uniform temperature achieved when the flow rate was at 0.01 m^3/s. The CF_2 mass fraction gradient near the substrate surface is highest and more uniform in the flow direction when the flow rate is approximately 0.01 m^3/s. However, this optimum flow rates will be changed if the reactor configuration is changed. Increasing the thickness of the hot gas volume means there are more than one layer of the filament in the array.

Increasing the hot gas region thickness does not change the temperature profile below the filaments, but increases the extent of the reaction in the reactor, resulting in a higher CF_2 gradient near the substrate. When the space above the filament array was reduced from 1.65 cm to 0.5 cm, the temperature profiles below the filament arrays was not changed, however the CF_2 mass fraction gradient near the substrate was increased. The optimal space above filament array is as small as possible, depending on the manufacturing tolerances and heat transfer issues. Decreasing the space below the filament from 6.5 to 5 mm does not significantly change either the temperature or CF_2 mass fraction profiles near the substrate. The optimal range is somewhere between 5 to 7 mm, and really depends on the manufacturing process.

6.2 Recommendations

In designing the reactor by solving the continuum transport equations, the physical and thermodynamic properties are the critical information to solve these equations. In this study, the physical properties of the species were calculated using the kinetic gas theory, therefore the Lennard-Jones parameters of each gas species have to be known. Unfortunately, the Lennard-Jones parameters for hexafluoropropylene oxide, tetrafluoroethene, and trifluoroacetylfluoride are not available in the literatures. The calculations were done by estimating these parameters from their critical points, for hexafluoropropylene oxide and tetrafluoroethene, or the normal boiling point, for the trifluoroacetyl fluoride. There are no experimental data available to estimate the error in these calculated properties. The experimental measurement for these species should be done in the future for higher accuracy.

The specific heat and the heat of formation for hexafluoropropylene oxide and trifluoroacetyl fluoride appearing in the energy equation are estimated using a

molecular mechanics approach. Although this method has been known to predict such properties with very high accuracy, experimental measurements of these properties are still needed for future studies. The comparison between the measurement and the calculation should be made.

This project has aimed to design a one-dimensional horizontal reactor mostly through the calculations. Most of the limitation of the reactor geometry came from the capability of the manufacturing technology. There is no real reactor and the experimental results to validate the calculation results. The future study should carry on both the simulation and experiments. The study of the kinetics and mechanism of the polymerization process using the mathematical model is recommended for the future study.

REFERENCES

[1] Kenneth K.S. Lau and Karen K. Gleason. Low dielectric constant fluorocarbon films. In Wei William Lee et al., editors, *Plasma deposition and treatment of polymers*, volume 544 of *Mater. Res. Soc. Symp. Proc.*, pages 209–219, Warrendale, Pennsylvania, Nov. 30 – Dec. 2, 1998. Materials Research Society.

[2] Kazuhiko Endo and Toru Tatsumi. Fluorinated amorphous carbon thin films grown by helicon plasma enhanced chemical vapor deposition for low dielectric constant interlayer dielectrics. *Applied Physics Letters*, 68(20):2864–2866, May 1996.

[3] R. H. Havemann, M. K. Jain, R. S. List, A. R. Ralston, W-Y. Shih, C. Jin, E. M. Zielinski, G. A. Dixit, A. Singh, S. W. Russell, J. F. Gaynor, A. J. Mckerrow, and M. W. Lee. Overview of process integration issues for low k dielectrics. In Chien Chiang et al., editors, *Low-dielectric constant materials IV*, volume 511 of *Mater. Res. Soc. Symp. Proc.*, pages 3–14, Pennsylvania, April 14–16 , 1998. Materials Research Society.

[4] J. N. Bremmer, Y. Liu, K. G. Cruszynski, and F. C. Dall. Cure of hydrogen silsesquioxane for intermetal dielectric applications. In C. Case et al., editors, *Low-dielectric constant materials III.* volume 476 of *Mater. Res. Soc. Symp. Proc.*, pages 37–44, New York, 1997. Materials Research Society.

[5] J. Pellerin, R. Fox, and H. Ho. Low dielectric constant fluorinated polyimides for interlayer dielectric applications. In C. Case et al., *Low-dielectric constant materials III*, volume 476 of *Mater. Res. Soc. Symp. Proc.*, pages 113–119, Pittsburgh, PA., 1997. Materials Research Society.

[6] N. P. Hacker, L. K. Figge, V. Fores, and S. P. lefferts. A new low dielectric constant siloxane polymer: Accuspin © T-24. In *Proceedings of the International Interconnect Technology Conference*, pages 286-288, Piscataway, NJ, 1998.

[7] R. N. Vrtis, K. A. Heap, W. F. Burgoyne, and L. M. Robeson. Poly(arylene ethers) as low dielectric constant materials for ULSI Interconnect applications. In *Low-dielectric constant materials II*, volume 443 of *Mater. Res. Soc. Symp. Proc.*, pages 171–176, Pittsburgh, P.A., 1997. Materials Research Society.

[8] Semiconductor Industry Association. *The International techonology roadmap for semiconductors.* http://public.itrs.net/files/2001ITRS/interconnect.pdf., 2001 edition., access date:10/5/2005.

[9] K. Endo. Fluorinated amorphous carbon as a low-dielectric-constant interlayer dielectric. *MRS Bulletin*, 22(10):55, 1997.

[10] W. Coburn and H. F. Winters. Plasma etching — a discussion of mechanisms. *J. Vac. Sci. Technol.*, 16(2):391–403, 1979.

[11] T. Shirafuji, A. Kamisawa, T. Shimasaki, Y. Hayashi, and S. Nishino. Plasma enhanced chemical vapor deposition of thermally stable and low-dielecrtric constant fluorinated amorphous carbon films using low-global-warming-potential gas C_5F_8, *Thin Solid Films*, 374:256-261, 2000.

[12] Jeoung W. Yi, Young H. Lee, and B. Farouk. Low dielectric fluorinated amorphous carbon thin films grown from C_6F_6 and Ar Plasma. *Thin Solid Films*, 374:103–108, 2000.

[13] R. d'Agostino, F. Cramarossa, F. Fracassi, E. Desimoni, L. Sabbatini, P.G. Zambonin, and G. Caporiccio. Polymer film formation in $C_2F_6H_2$ discharges. *Thin Solid Films*, 143(2):163–175, 1986.

[14] S.F. Durrant, E.C. Rangel, and N.C. daCruz, S.G.C. Castro, and M.A.B deMoraes. Amorphous hydrogenated fluorinated carbon films produced by PECVD. *Surf. Coat. Technol.*, 87-8(1-3):443–448, Dec. 1996.

[15] K. Endo and T. Tatsumi, Fluorinated amorphous carbon thin films grown by plasma enhanced chemical vapor deposition for low dielectric constant interlayer dielectrics. *J. Applied Physics*, 78(2):1370–1372, Jul. 1995.

[16] P. B. Leezenberg, T. C. Reiley, and G. W. Tyndall. Plasma induced copoly-merization of hexafluoropropylene and octafluoropropane, *J. Vac. Sci. Technol A*, 17(1):275–281, Jan./Feb. 1999.

[17] H. Yasuda and T. Hsu. Some aspects of plasma polymerization investigated by pulsed RF discharge. *J. Polym. Sci., Polym. Chem. Ed.*, 15(1):81–97, Jan. 1977.

[18] C. B. Labelle, S. J. Limb, and K. K. Gleason. Electron spin resonance of pulsed plasma-enhanced chemical, vapor deposited fluorocarbon films. *Journal of Applied Physics*, 82(4):1784–1787, August 1997.

[19] C. B. Labelle and K. K. Gleason. Pulsed plasma-enhanced chemical vapor deposition from CH_2F_2, $C_2H_2F_4$, and $CHClF_2$. *J. Vac. Sci. Technol. A*, 17(2):445-452, Mar./Apr. 1999.

[20] S. J. Limb, K. K. Gleason, D. J. Edell, and E. F. Gleason. Flexible fluorocarbon wire coatings by pulsed plasma enhanced chemical vapor deposition. *J. Vac. Sci. Technol. A*, 15(4):1814–1818, Jul./Aug. 1997.

[21] S.J. Limb, D. J. Edell, E. F. Gleason, and K. K. Gleason. Pulsed plasma-enhanced chemical vapor deposition from Hexafluoropropylene Oxide: film composition study, *J. Appl. Polym. Sci.*, 67:1489-1502, 1998.

[22] Kenneth K. S. Lau and Karen K. Gleason. SoLid-State Nucear Magnetic Resonance spectroscopy of low dielectric constant films from pulsed Hydrofluoro-carbon plasmas. *J. Electrochem. Soc*, 146(7):2652-2658, 1999.

[23] Scott J. Limb, C. B. Labelle, K. K. Gleason, D. J. Edell, and E. F. Gleason. Growth of fluorocarbon polymer thin films with high CF_2 fractions and low dangling bond concentrations by thermal chemical vapor deposition. *Applied Physics Letters*, 68(20):2810–2812, May 1996.

[24] K. K. S. Lau and K. K. Gleason. Pulsed plasma enhanced and hot filament chemical vapor deposition of fluorocarbon films. *J. Fluorine Chem.*, 104:119–126, 2000.

[25] K. K. S. Lau, Jeffrey A. Caufield, and Karen K. Gleason. Structure and morphology of fluorocarbon films grown by hot filament chemical vapor deposition. *Chem. Mater.*, 12:3032–3037, 2000.

[26] Nason, T.C. and Lu, T.M. Thermoplastic spectroscopic properties of amorphous fluoropolymer thin-films. *Thin Solid Films*, 239(1):27–30, Feb. 1990.

[27] Hynek Biederman. Organic films prepared by polymer sputtering. *J. Vac. Sci. Technol. A*, 18(4):1642-1648, Jul./Aug. 2000.

[28] M. A. Golub, T. Wydeven, and A. L. Johnson. Similarity of plasma-polymerized tetrafluoroethylene and fluoropolymer films deposited by rf sputtering of poly(tetrafluoroethylene). *Langmuir*, 14:2217–2220, 1998.

[29] Goodmann, J. The formation of thin polymer films in the gas discharge. *J. Polym. Sci.*, 44(144):551-552, 1960.

[30] R. A. Connell and L.V. gregor. Magnetically shaped rf discharge for polymer film formation. *J. Electrochem. Soc.*, 112(12):1198, 1965.

[31] J. A. Theil. Fluorinated amorphous carbon films for low permittivity interlevel dielectrics, *J. Vac. Sci. Technol. B*, 17(6):2397–2410, Nov./Dec. 1999.

[32] Yasuda H. *Plasma polymerization.* Academic, New York, 1985.

[33] H. Yang and D. J. Tweet and Y. Ma and T. Nguyen. Deposition of highly crosslinked fluorinated amorphous carbon film and structural evolution during thermal annealing. *Applied Physics Letters*, 73(11):1514–1516, Sep. 1998.

[34] C. I. Butoi, N. M. Mackie, J. L. Barnd, and E. R. Fisher. Deposition of highly ordered CF_2-rich films using continuous wave and pulsed hexafluoropropylene oxide plasmas. *Chem. Mater.*, 12(7):2014–2024, 2000.

[35] H. Yasuda and T. Hsu. Glow discharge polymerization. *J. Polym. Sci. Macromol. Rev.*, 16:199–293, 1981.

[36] C. I. Butoi, N. M. Mackie, L. J. Gamble, D. G. Castner, J. Barnd, A. M. Miller, and E. R. Fisher. Control of surface film composition and orientation with downstream PECVD of hexafluoropropylene oxide. *Chem. Mater.*, 11(4):862–864, 1999.

[37] C. R. Savage and R. B. Timmons and J. W. Lin. Molecular control of surface-film compositions vis pulsed radio frequency plasma deposition of perfluoropropylene oxide. *Chem. Mater.* 3(4):575–577, Jul.–Aug. 1991.

[38] C. R. Savage, R. B. Timmons, and J. W. Lin. Spectroscopic characterization of films obtained in pulsed radio-frequency plasma discharges of fluorocarbon monomers. In M. W. Urban and C. D. Craver, editors, *Structure-property relations in polymers:spectroscopy and performance.* volume 236 of *Advances in Chemistry Series*, pages 745–768, Washington, D.C., 1993. American Chemical Society.

[39] Scott J. Limb, K. K. S. Lau, D. J. Edell, E. F. Gleason, and K. K. Gleason. Molecular design of fluorocarbon film architecture by pulsed plasma enhanced and pyrolytic chemical vapor deposition. *Plasmas and Polymers*, 4(1):21–32, 1999.

[40] NIST. *Chemistry webbook.* http://webbook.nist.gov/chemistry, 2000.

[41] David R. Lide, *CRC Handbook of chemistry and physics.* CRC press, Boca Raton, Florida, 81st edition, 2000.

[42] E. H. Zytkus. DUPONT, circa 1962–3.

[43] Robert C. Reid, John M. Prausnitz, and Bruce E. Poling. *The properties of gases & liquids.* McGraw-Hill, New York, 4th edition, 1987.

[44] E.L. Pace and P.E. Hodge. Thermodynamics properties of trifluoroacetyl fluoride from 14 K to its boiling temperature. *J. Chem. Thermodynam.*, 4:441–447, 1972.

[45] P.D. Neufeld, A.R. Janzen, and R.A. Aziz. Empirical equation to calculate 16 of the transport collision integrals $\omega^{(l,s)*}$ for the Lennard-Jones (12-6) potential. *J. Chem. Phys.*, 57:1100–1102, 1972.

[46] M. W. Chase, Jr. NIST-JANAF Thermochemical tables, 4th edition. *J. Phys. Chem. ref. Data.*, Monograph 9:1–1951, 1998.

[47] R. Craig Kennedy and Joseph B. Levy. The pyrolysis of hexafluoropropylene oxide. *J. Fluorine Chem.*, 7:101–114, 1976.

[48] Walter Mahler and Paul R. Resnick. The reversible difluorocarbene elimination from hexafluoropropylene epoxide. *J. Fluorine Chem.*, 3:451–452, 1973.

[49] Mark B. Knickelbein, Douglas A. Webb, and Edward R. Grant. New devices for the production of intense pulsed jets of CF_2: laser spectroscopic characterization. volume 38 of *Mater. Res. Soc. Symp. Proc.*, pages 23–33. Materials Research Society, 1985.

[50] M. Lenzi, and A. Mele. Kinetics of thermal decomposition of tetrafluoroethylene oxide. *J. Chem. Phys.*, 43(6):1974, 1965.

[51] Mel'nikovich, S.I. *Canadian Sci. (Chem.) Dissertation*, L'vov:L'vov. Politekhnicheskii Inst., 1990.

[52] N. N. Buravtsev, Yu. A. Kolbanovskii, T. S. Kuptsova, and O. M. Nefedov. *Abstracts of papers of VI All-Union Conf. on Chemistry of Organofluorine compounds.* page 124. Novosibirsk, 1990.

[53] V. A. Dunyakhin, V. V. Timofeev, E. A. Tveritinova, N. Yu. Ignat'eva, and Yu. N. Zhitnev. Laser Induced Degradation of Hexafluoropropylene Oxide. *High Energy Chemistry.*, 28(6):538-542, 1994.

[54] P. J. Krusic, D. C. Roe, and B. E. Smart. Kinetics of hexafluoropropylene oxide pyrolysis studied by gas-phase NMR. *Israel Journal of Chemistry.*, 39:117-123, 1999.

[55] S. V. Mel'nikovich, and F. B. Moin. Kinetics and mechanism of reaction of difluorocarbene. *Kinetica I Kataliz*, 29(2):298-302, 1988.

[56] F. W. Dalby. Flash photolysis measurement of the kinetics of CF_2 reactions. J. Chem. Phys., 41(8):2297-2303, 1964.

[57] W. J. R. Tyerman. Rate parameters for reactions of ground state difluorocarbene and determination of the absolute intensity of the $\tilde{A}^1B_1$–X^1A_1 absorption band. *Trans. Faraday Soc.*, 69(7):1188-1198, 1969.

[58] B. Atkinson, and D. McKeagan. The thermal decomposition of perfluoro-cyclopropane. Chem. Comm., 7:189-190, 1966.

[59] N. Cohen, and J. Heicklen. Mercury-sensitized photolysis of C_2F_4. *J. Chem. Phys.*, 43(3):871-873, 1965.

[60] J. P. Vandoormaal, G. D. Raithby. Enhancements of the SIMPLE method for predicting incompressible fluid flows. *Numerical Heat Transfer*, 7:147–163, 1984.

[61] K. F. Jensen. Flow phenomena in chemical vapor deposition of thin films. *Annu. Rev. Fluid Mech.*, 23:197–232, 1991.

[62] K. Tankala and T. Debroy. Transport phenomena in the scale-up of hot filament-assisted chemical vapor deposition of diamond. *Surface and Coatings Technology*, 62:349–355, 1993.

[63] K. K. S. Lau, Jeffrey A. Caufield, and Karen K. Gleason. Unpublished data.

[64] Chris R. Kleijn and Christoph Werner. *Modeling of chemical vapor deposition of Tungsten films.* Birkhäuser Verlag, Basel, Germany, 1993.

[65] B. Atkinson, M. P. Brocklebank, C. C. H. Card, and J. M. Smith. Low Reynolds number developing flows. *AIChE Journal*, 15(4)`:548-553, July 1969.

[66] R. B. Bird, W. E. Stewart, and E. N. Lightfoot. *Transport Phenomena.* 2nd edition, page 848, John Wiley & Sons, Inc., New York, 2002.

[67] William H. McAdams. *Heat Transmission.* 3rd edition, Mc-Graw-Hill, New York, 1954.

[68] K. K. S. Lau, K. K. Gleason, and B. L. Trout. Thermochemistry of gas phase CF_2 reaction: A density functional theory study. *J. Chem. Phys.*, 113(10):4103-4108, 2000.

Appendix A

SPECIFIC HEAT

A.1 Specific Heat of HFPO

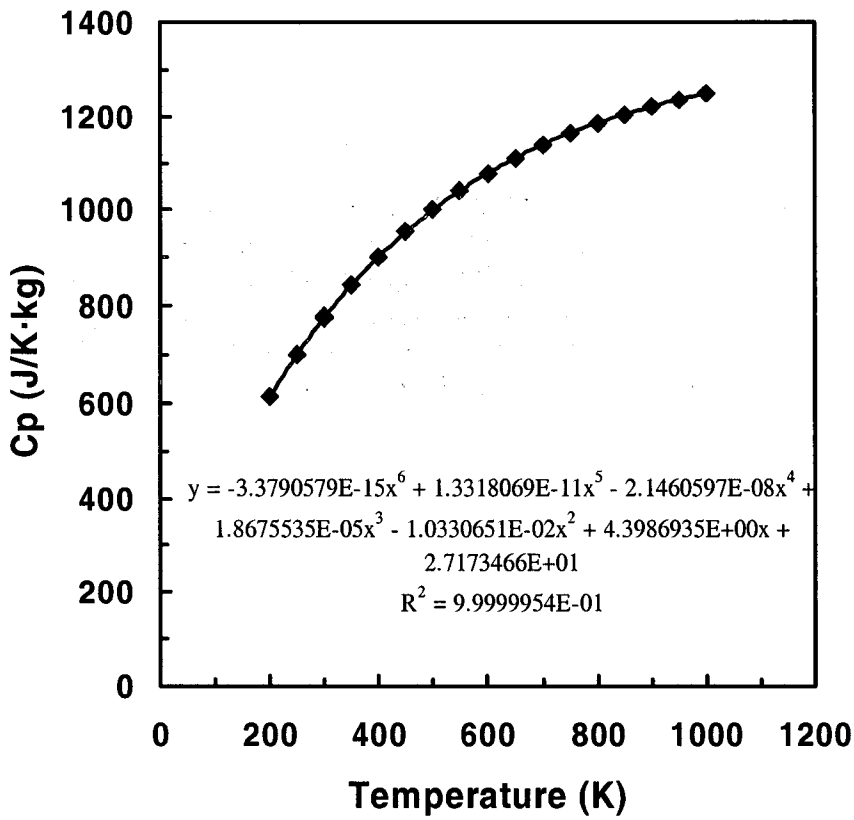

Figure A.1 Curve fitting of HFPO specific heat calculated from CACHE program. The value shown on the curve is the average value calculated by AM1, MNDod, PM3, PM3Cl, and PM5 methods.

A.2 Specific Heat of Trifluoroacetyl Fluoride

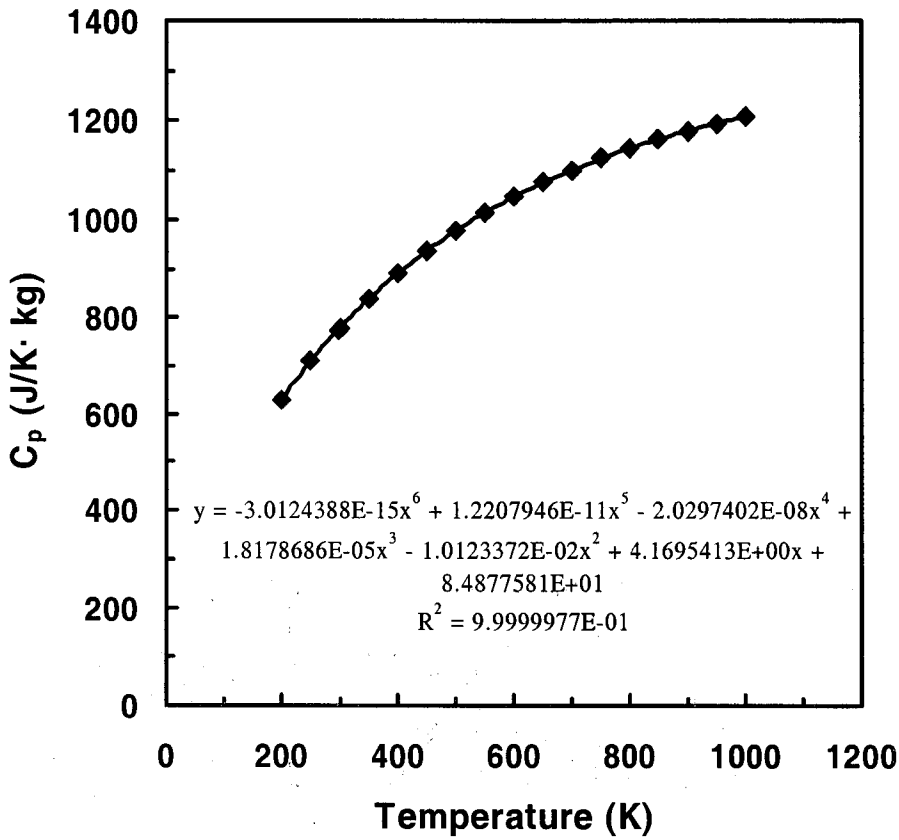

Figure A.2 **Curve fitting of trifluoroacetyl fluoride specific heat calculated from CACHE program. The value shown on the curve is the average value calculated by AM1, MNDod, PM3, PM3Cl, and PM5 methods.**

A.3 Specific Heat of Difluoromethylene

Table A.1 Thermochemical data of difluoromethylene [46]

Enthalpy Reference Temperature = T_r = 298.15 K Standard State Pressure = p° = 0.1 MPa

	J·K⁻¹·mol⁻¹			kJ·mol⁻¹			
T/K	C_p°	S°	$-[G^\circ-H^\circ(T_r)]/T$	$H^\circ-H^\circ(T_r)$	$\Delta_f H^\circ$	$\Delta_f G^\circ$	log K_f
0	0.	0.	INFINITE	−10.354	−182.482	−182.482	INFINITE
100	33.311	202.633	272.908	−7.028	−182.122	−185.253	96.766
200	35.154	226.123	244.265	−3.628	−181.979	−188.456	49.220
250	36.964	234.154	241.463	−1.827	−181.975	−190.077	39.714
298.15	38.948	240.833	240.833	0.	−182.004	−191.635	33.574
300	39.026	241.074	240.834	0.072	−182.006	−191.695	33.377
350	41.119	247.248	241.316	2.076	−182.061	−193.306	28.849
400	43.097	252.869	242.414	4.182	−182.138	−194.907	25.452
450	44.887	258.051	243.867	6.383	−182.232	−196.498	22.809
500	46.465	262.864	245.529	8.667	−182.345	−198.077	20.693
600	49.020	271.573	249.160	13.448	−182.616	−201.199	17.516
700	50.913	279.279	252.923	18.449	−182.939	−204.271	15.243
800	52.319	286.173	256.656	23.614	−183.305	−207.294	13.535
900	53.376	292.400	260.287	28.901	−183.706	−210.269	12.204
1000	54.184	298.067	263.786	34.281	−184.139	−213.197	11.136
1100	54.812	303.262	267.142	39.732	−184.602	−216.081	10.261
1200	55.308	308.053	270.354	45.239	−185.092	−218.921	9.529
1300	55.705	312.497	273.427	50.791	−185.609	−221.719	8.909
1400	56.028	316.637	276.367	56.378	−186.152	−224.477	8.375
1500	56.293	320.512	279.182	61.994	−186.721	−227.195	7.912
1600	56.515	324.152	281.880	67.635	−187.314	−229.874	7.505
1700	56.702	327.584	284.469	73.296	−187.930	−232.515	7.144
1800	56.864	330.830	286.955	78.975	−188.568	−235.119	6.823
1900	57.006	333.908	289.346	84.668	−189.225	−237.688	6.534
2000	57.134	336.836	291.648	90.375	−189.899	−240.221	6.274
2100	57.252	339.626	293.867	96.095	−190.585	−242.721	6.037
2200	57.365	342.292	296.008	101.825	−191.280	−245.187	5.821
2300	57.475	344.844	298.076	107.567	−191.980	−247.621	5.624
2400	57.586	347.293	300.076	113.321	−192.680	−250.026	5.442
2500	57.700	349.646	302.012	119.085	−193.376	−252.401	5.274
2600	57.820	351.911	303.888	124.861	−194.062	−254.748	5.118
2700	57.947	354.096	305.707	130.649	−194.734	−257.069	4.973
2800	58.083	356.206	307.473	136.451	−195.388	−259.366	4.839
2900	58.229	358.246	309.189	142.266	−196.020	−261.640	4.713
3000	58.384	360.223	310.858	148.097	−196.625	−263.892	4.595
3100	58.551	362.140	312.481	153.943	−197.201	−266.125	4.484
3200	58.728	364.002	314.062	159.807	−197.743	−268.339	4.380
3300	58.916	365.812	315.603	165.689	−198.249	−270.538	4.282
3400	59.115	367.574	317.106	171.591	−198.716	−272.721	4.190
3500	59.323	369.290	318.572	177.513	−199.143	−274.891	4.103
3600	59.541	370.964	320.004	183.456	−199.527	−277.050	4.020
3700	59.768	372.599	321.404	189.421	−199.866	−279.199	3.942
3800	60.002	374.196	322.772	195.410	−200.160	−281.339	3.867
3900	60.242	375.758	324.111	201.422	−200.407	−283.472	3.797
4000	60.488	377.286	325.421	207.458	−200.607	−285.599	3.730
4100	60.739	378.783	326.705	213.520	−200.760	−287.722	3.666
4200	60.993	380.249	327.962	219.606	−200.865	−289.841	3.605
4300	61.250	381.687	329.195	225.718	−200.922	−291.959	3.547
4400	61.508	383.098	330.404	231.856	−200.932	−294.076	3.491
4500	61.766	384.484	331.590	238.020	−200.895	−296.193	3.438
4600	62.024	385.844	332.755	244.209	−200.811	−298.312	3.387
4700	62.280	387.181	333.899	250.425	−200.682	−300.433	3.339
4800	62.533	388.495	335.023	256.665	−200.508	−302.557	3.292
4900	62.783	389.786	336.127	262.931	−200.290	−304.685	3.248
5000	63.029	391.057	337.213	269.222	−200.029	−306.818	3.205
5100	63.270	392.308	338.281	275.537	−199.727	−308.957	3.164
5200	63.506	393.539	339.332	281.875	−199.385	−311.102	3.125
5300	63.735	394.751	340.366	288.238	−199.003	−313.254	3.087
5400	63.958	395.944	341.384	294.622	−198.584	−315.413	3.051
5500	64.174	397.120	342.387	301.029	−198.129	−317.581	3.016
5600	64.383	398.278	343.375	307.457	−197.639	−319.757	2.983
5700	64.584	399.419	344.348	313.905	−197.116	−321.943	2.950
5800	64.776	400.544	345.307	320.373	−196.561	−324.138	2.919
5900	64.961	401.653	346.253	326.860	−195.976	−326.342	2.889
6000	65.137	402.746	347.185	333.365	−195.361	−328.557	2.860

PREVIOUS: June 1970 (1 atm) CURRENT: June 1970 (1 bar)

A.4 Specific Heat of Tetrafluoroethene

Table A.2 Thermochemical data of tetrafluoroethylene [46]

Enthalpy Reference Temperature = T_r = 298.15 K Standard State Pressure = p° = 0.1 MPa

	J·K⁻¹·mol⁻¹			kJ·mol⁻¹			
T/K	C_p°	S°	$-[G^\circ-H^\circ(T_r)]/T$	$H^\circ-H^\circ(T_r)$	$\Delta_f H^\circ$	$\Delta_f G^\circ$	log K_f
0	0.	0.	INFINITE	−16.330	−655.140	−655.140	INFINITE
100	44.191	233.706	360.595	−12.689	−657.432	−646.538	337.717
200	65.202	270.959	306.921	−7.192	−658.446	−635.144	165.883
250	73.646	286.445	301.303	−3.715	−658.565	−629.302	131.485
298.15	80.458	300.015	300.015	0.	−658.562	−623.665	109.263
300	80.698	300.514	300.017	0.149	−658.560	−623.448	108.552
350	86.707	313.416	301.022	4.338	−658.491	−617.601	92.172
400	91.903	325.342	303.326	8.806	−658.387	−611.767	79.889
450	96.426	336.433	306.396	13.517	−658.267	−605.946	70.336
500	100.373	346.802	309.923	18.439	−658.138	−600.140	62.696
600	106.824	365.699	317.676	28.814	−657.867	−588.565	51.239
700	111.747	382.553	325.762	39.753	−657.577	−577.037	43.059
800	115.524	397.732	333.826	51.125	−657.266	−565.553	36.927
900	118.450	411.515	341.704	62.830	−656.939	−554.108	32.160
1000	120.743	424.118	349.324	74.794	−656.601	−542.700	28.348
1100	122.561	435.715	356.658	86.963	−656.259	−531.327	25.231
1200	124.020	446.444	363.699	99.294	−655.922	−519.984	22.634
1300	125.206	456.419	370.452	111.758	−655.595	−508.669	20.439
1400	126.179	465.735	376.929	124.328	−655.285	−497.380	18.557
1500	126.986	474.468	383.143	136.988	−654.995	−486.111	16.928
1600	127.662	482.686	389.110	149.721	−654.729	−474.860	15.503
1700	128.233	490.443	394.845	162.517	−654.489	−463.626	14.245
1800	128.720	497.787	400.362	175.365	−654.274	−452.405	13.128
1900	129.137	504.758	405.675	188.258	−654.082	−441.196	12.129
2000	129.498	511.391	410.796	201.191	−653.911	−429.995	11.230
2100	129.811	517.717	415.738	214.156	−653.757	−418.804	10.417
2200	130.085	523.762	420.512	227.152	−653.614	−407.619	9.678
2300	130.326	529.550	425.128	240.172	−653.477	−396.440	9.003
2400	130.539	535.102	429.595	253.216	−653.339	−385.268	8.385
2500	130.728	540.434	433.923	266.279	−653.195	−374.101	7.816
2600	130.896	545.565	438.119	279.361	−653.038	−362.940	7.292
2700	131.047	550.508	442.190	292.458	−652.862	−351.786	6.806
2800	131.182	555.276	446.144	305.570	−652.662	−340.639	6.355
2900	131.305	559.882	449.987	318.694	−652.432	−329.499	5.935
3000	131.415	564.335	453.725	331.830	−652.167	−318.368	5.543
3100	131.515	568.646	457.363	344.977	−651.865	−307.246	5.177
3200	131.607	572.823	460.906	358.133	−651.521	−296.135	4.834
3300	131.690	576.874	464.359	371.298	−651.132	−285.035	4.512
3400	131.766	580.806	467.727	384.471	−650.697	−273.947	4.209
3500	131.836	584.627	471.012	397.651	−650.214	−262.873	3.923
3600	131.901	588.342	474.220	410.838	−649.681	−251.813	3.654
3700	131.960	591.957	477.354	424.031	−649.097	−240.770	3.399
3800	132.015	595.476	480.416	437.230	−648.463	−229.743	3.158
3900	132.066	598.906	483.410	450.434	−647.778	−218.732	2.930
4000	132.113	602.250	486.340	463.643	−647.042	−207.740	2.713
4100	132.156	605.513	489.207	476.856	−646.257	−196.768	2.507
4200	132.197	608.698	492.014	490.074	−645.422	−185.814	2.311
4300	132.235	611.809	494.764	503.295	−644.539	−174.882	2.124
4400	132.270	614.850	497.459	516.521	−643.609	−163.970	1.947
4500	132.303	617.823	500.101	529.749	−642.633	−153.080	1.777
4600	132.334	620.731	502.692	542.981	−641.613	−142.212	1.615
4700	132.363	623.577	505.233	556.216	−640.550	−131.367	1.460
4800	132.391	626.364	507.728	569.454	−639.446	−120.545	1.312
4900	132.416	629.094	510.177	582.694	−638.301	−109.746	1.170
5000	132.440	631.770	512.582	595.937	−637.118	−98.971	1.034
5100	132.463	634.393	514.945	609.182	−635.899	−88.220	0.904
5200	132.484	636.965	517.267	622.430	−634.644	−77.493	0.778
5300	132.505	639.489	519.549	635.679	−633.356	−66.791	0.658
5400	132.524	641.966	521.793	648.930	−632.036	−56.114	0.543
5500	132.542	644.398	524.001	662.184	−630.686	−45.461	0.432
5600	132.559	646.786	526.172	675.439	−629.307	−34.833	0.325
5700	132.575	649.132	528.309	688.696	−627.900	−24.231	0.222
5800	132.591	651.438	530.412	701.954	−626.468	−13.652	0.123
5900	132.606	653.705	532.482	715.214	−625.011	−3.098	0.027
6000	132.620	655.934	534.521	728.475	−623.532	7.430	−0.065

PREVIOUS: June 1969 (1 atm) CURRENT: June 1969 (1 bar)

Appendix B

STANDARD STATE HEAT OF FORMATION

Table B.1: Species Heat of formation.

Species	$\Delta_f H°(298.15K)$	*Reference*
C_2F_4	-658.56±2.9 kJ/mol	[46]
CF_2	-182.00±6.3 kJ/mol	[46]
HFPO	-309.2 kcal/mol	[68]
CF_3CFO	-239.9 kcal/mol	[68]

Appendix C

USER DEFINED FUNCTIONS FOR INLET VELOCITY PROFILES AND HEAT TRANSFER COEFFICIENT

C.1 Inlet Velocity Profile

Function

```
/************************************************************************
• uprofile.C                                                            *
• UDF for specifying the velocity profile boundary condition            *
************************************************************************/

#include "udf.h"

real U(double x, double y, double a, double b, double Q, double mu);

const real vis = 1.834124e-5; /*viscosity (Pa.s)*/
const real A = 0.165; /* half width of the channel (m) */
const real B = 0.015; /* half height of the channel (m) */
const real FLOW = 0.01; /* volumetric flowrate (m^3/s) */

DEFINE_PROFILE(inlet_velocity, thread, position)
{

    real xx, y;
    face_t f;
    real x[ND_ND];

  begin_f_loop (f, thread)
   {
   F_CENTROID(x,f,thread);
   xx = x[0];
   y = x[1];
   F_PROFILE(f, thread, position)=U(xx, y, A, B, FLOW, vis);
```

```
    }
  end_f_loop(f, thread)
}

real U(double x, double y, double a, double b, double Q, double mu)

{
    real lambda, termg, g, lambdaA, lambdaB;
    real u1, u2, u, an;
    real sumu = 0.0;
    real sumg = 0.0;
    int i;
    for( i = 0; i<=1000; i++)
  {
    lambda = (2.0*i+1.0)*M_PI/(2.0*a);
    lambdaA= lambda*a;
    lambdaB = lambda*b;
    termg = sin(lambdaA)*sin(lambdaA)*tanh(lambdaB)/pow(lambda,5); sumg =
    sumg + termg;
  }
    g = mu*Q/4.0/(pow(a,3.0)/3.0*b-2.0/a*sumg);
    u1 = g*(a*a - x*x)/(2.0*mu);
    for (i = 0; i<=1000; i++)
  {
    lambda = (2.0*i+1.0)*M_PI/(2.0*a);
    lambdaA = lambda*a;
    lambdaB = lambda*b;
    an = -2.0*g*sin(lambdaA)/(mu*a*pow(lambda,3.0)*cosh(lambdaB)); u2 =
    an*cos(lambda*x)*cosh(lambda*y); sumu = sumu + u2;
  }
    u = u1 + sumu;
    return u;
}
```

C.2 Heat Transfer Coefficient Function

```
/************************************************************************/
/* hExt.c                                                               */
/* UDF for specifying a external heat transfer coefficients             */
/************************************************************************/

#include "udf.h"

DEFINE_PROFILE(h_ext_horiz, thread, position)

{
face_t f;
real temp, tempF;
const real L = 0.9514435695538; /* Length of the horizontal surface in ft */

begin_f_loop(f, thread)

 {
   temp = F_T(f, thread);
   tempF = (temp - 273.15) * 1.8 + 32.0-80.0;
   F_PROFILE(f, thread, position) = 5.6782*0.27*pow(tempF/L,0.25);
 }
end_f_loop(f, thread)

}

DEFINE_PROFILE(h_ext_vert1, thread, position)

{
face_t f;
real temp, tempF;
const real L1 = 0.041666666; /* Height of the vertical surface in ft */

begin_f_loop(f,thread)

 {
   temp = F_T(f, thread);
   tempF = (temp -273.15) * 1.8 + 32.0 - 80.0;
   F_PROFILE(f, thread, position) = 5.6782*0.29*pow(tempF/L1,0.25);
 }
end_f_loop(f, thread)

}
```

```
DEFINE_PROFILE(h_ext_vert2, thread, position)
{
face_t f;
real temp, tempF;
const real L2 = 0.098425196; /* Height of the vertical surface in ft */

begin_f_loop(f,thread)
 {
   temp = F_T(f, thread);
   tempF = (temp -273.15) * 1.8 + 32.0 - 80.0;
   F_PROFILE(f, thread, position) = 5.6782*0.29*pow(tempF/L2,0.25);
 }
end_f_loop(f, thread)
}
```